Fermi National Accelerator Laboratory

FERMILAB-Pub-95/033-E

CDF

Measurement of the W Boson Mass

F. Abe et al.
The CDF Collaboration

Fermi National Accelerator Laboratory
P.O. Box 500, Batavia, Illinois 60510

March 1995

Submitted to *Physical Review D*

Operated by Universities Research Association Inc. under Contract No. DE-AC02-76CHO3000 with the United States Department of Energy

Disclaimer

CDF/PUB/ELECTROWEAK/PUBLIC/2864
FERMILAB-PUB-95/033-E

Measurement of the W Boson Mass

F. Abe,[13] M. G. Albrow,[7] D. Amidei,[16] J. Antos,[28] C. Anway-Wiese,[4] G. Apollinari,[26] H. Areti,[7] M. Atac,[7] P. Auchincloss,[25] F. Azfar,[21] P. Azzi,[20] N. Bacchetta,[18] W. Badgett,[16] M. W. Bailey,[18] J. Bao,[34] P. de Barbaro,[25] A. Barbaro-Galtieri,[14] V. E. Barnes,[24] B. A. Barnett,[12] P. Bartalini,[23] G. Bauer,[15] T. Baumann,[9] F. Bedeschi,[23] S. Behrends,[3] S. Belforte,[23] G. Bellettini,[23] J. Bellinger,[33] D. Benjamin,[32] J. Benlloch,[15] J. Bensinger,[3] D. Benton,[21] A. Beretvas,[7] J. P. Berge,[7] S. Bertolucci,[8] A. Bhatti,[26] K. Biery,[11] M. Binkley,[7] F. Bird,[29] D. Bisello,[20] R. E. Blair,[1] C. Blocker,[29] A. Bodek,[25] W. Bokhari,[15] V. Bolognesi,[23] D. Bortoletto,[24] C. Boswell,[12] T. Boulos,[14] G. Brandenburg,[9] C. Bromberg,[17] E. Buckley-Geer,[7] H. S. Budd,[25] K. Burkett,[16] G. Busetto,[20] A. Byon-Wagner,[7] K. L. Byrum,[1] J. Cammerata,[12] C. Campagnari,[7] M. Campbell,[16] A. Caner,[7] W. Carithers,[14] D. Carlsmith,[33] A. Castro,[20] Y. Cen,[21] F. Cervelli,[23] H. Y. Chao,[28] J. Chapman,[16] M.-T. Cheng,[28] G. Chiarelli,[8] T. Chikamatsu,[31] C. N. Chiou,[28] S. Cihangir,[7] A. G. Clark,[23] M. Cobal,[23] M. Contreras,[5] J. Conway,[27] J. Cooper,[7] M. Cordelli,[8] D. Crane,[1] J. D. Cunningham,[3] T. Daniels,[15] F. DeJongh,[7] S. Delchamps,[7] S. Dell'Agnello,[23] M. Dell'Orso,[23] L. Demortier,[26] B. Denby,[23] M. Deninno,[2] P. F. Derwent,[16] T. Devlin,[27] M. Dickson,[25] S. Donati,[23] R. B. Drucker,[14] A. Dunn,[16] K. Einsweiler,[14] J. E. Elias,[7] R. Ely,[14] E. Engels, Jr.,[22] S. Eno,[5] D. Errede,[10] S. Errede,[10] Q. Fan,[25] B. Farhat,[15] I. Fiori,[2] B. Flaugher,[7] G. W. Foster,[7] M. Franklin,[9] M. Frautschi,[18] J. Freeman,[7] J. Friedman,[15] H. Frisch,[5] A. Fry,[29] T. A. Fuess,[1] Y. Fukui,[13] S. Funaki,[31] G. Gagliardi,[23] S. Galeotti,[23] M. Gallinaro,[20] A. F. Garfinkel,[24] S. Geer,[7] D. W. Gerdes,[16] P. Giannetti,[23] N. Giokaris,[26] P. Giromini,[8] L. Gladney,[21] D. Glenzinski,[12] M. Gold,[18] J. Gonzalez,[21] A. Gordon,[9] A. T. Goshaw,[6] K. Goulianos,[26] H. Grassmann,[6] A. Grewal,[21] G. Grieco,[23] L. Groer,[27] C. Grosso-Pilcher,[5] C. Haber,[14] S. R. Hahn,[7] R. Hamilton,[9] R. Handler,[33] R. M. Hans,[34] K. Hara,[31] B. Harral,[21] R. M. Harris,[7] S. A. Hauger,[6] J. Hauser,[4] C. Hawk,[27] J. Heinrich,[21] D. Cronin-Hennessy,[6] R. Hollebeek,[21] L. Holloway,[10] A. Hölscher,[11] S. Hong,[16] G. Houk,[21] P. Hu,[22] B. T. Huffman,[22] R. Hughes,[25] P. Hurst,[9] J. Huston,[17] J. Huth,[9] J. Hylen,[7] M. Incagli,[23] J. Incandela,[7] H. Iso,[31] H. Jensen,[7] C. P. Jessop,[9] U. Joshi,[7] R. W. Kadel,[14] E. Kajfasz,[7a] T. Kamon,[30] T. Kaneko,[31] D. A. Kardelis,[10] H. Kasha,[34] Y. Kato,[19] L. Keeble,[30] R. D. Kennedy,[27] R. Kephart,[7] P. Kesten,[14] D. Kestenbaum,[9] R. M. Keup,[10] H. Keutelian,[7] F. Keyvan,[4] D. H. Kim,[7] H. S. Kim,[11] S. B. Kim,[16]

Submitted to Physical Review D March 6, 1995

S. H. Kim,[31] Y. K. Kim,[14] L. Kirsch,[3] P. Koehn,[25] K. Kondo,[31] J. Konigsberg,[9] S. Kopp,[5] K. Kordas,[11] W. Koska,[7] E. Kovacs,[7a] W. Kowald,[6] M. Krasberg,[16] J. Kroll,[7] M. Kruse,[24] S. E. Kuhlmann,[1] E. Kuns,[27] A. T. Laasanen,[24] N. Labanca,[23] S. Lammel,[4] J. I. Lamoureux,[3] T. LeCompte,[10] S. Leone,[23] J. D. Lewis,[7] P. Limon,[7] M. Lindgren,[4] T. M. Liss,[10] N. Lockyer,[21] C. Loomis,[27] O. Long,[21] M. Loreti,[20] E. H. Low,[21] J. Lu,[30] D. Lucchesi,[23] C. B. Luchini,[10] P. Lukens,[7] P. Maas,[33] K. Maeshima,[7] A. Maghakian,[26] P. Maksimovic,[15] M. Mangano,[23] J. Mansour,[17] M. Mariotti,[23] J. P. Marriner,[7] A. Martin,[10] J. A. J. Matthews,[18] R. Mattingly,[15] P. McIntyre,[30] P. Melese,[26] A. Menzione,[23] E. Meschi,[23] G. Michail,[9] S. Mikamo,[13] M. Miller,[5] R. Miller,[17] T. Mimashi,[31] S. Miscetti,[8] M. Mishina,[13] H. Mitsushio,[31] S. Miyashita,[31] Y. Morita,[13] S. Moulding,[26] J. Mueller,[27] A. Mukherjee,[7] T. Muller,[4] P. Musgrave,[11] L. F. Nakae,[29] I. Nakano,[31] C. Nelson,[7] D. Neuberger,[4] C. Newman-Holmes,[7] L. Nodulman,[1] S. Ogawa,[31] S. H. Oh,[6] K. E. Ohl,[34] R. Oishi,[31] T. Okusawa,[19] C. Pagliarone,[23] R. Paoletti,[23] V. Papadimitriou,[7] S. Park,[7] J. Patrick,[7] G. Pauletta,[23] M. Paulini,[14] L. Pescara,[20] M. D. Peters,[14] T. J. Phillips,[6] G. Piacentino,[2] M. Pillai,[25] R. Plunkett,[7] L. Pondrom,[33] N. Produit,[14] J. Proudfoot,[1] F. Ptohos,[9] G. Punzi,[23] K. Ragan,[11] F. Rimondi,[2] L. Ristori,[23] M. Roach-Bellino,[32] W. J. Robertson,[6] T. Rodrigo,[7] J. Romano,[5] L. Rosenson,[15] W. K. Sakumoto,[25] D. Saltzberg,[5] A. Sansoni,[8] V. Scarpine,[30] A. Schindler,[14] P. Schlabach,[9] E. E. Schmidt,[7] M. P. Schmidt,[34] O. Schneider,[14] G. F. Sciacca,[23] A. Scribano,[23] S. Segler,[7] S. Seidel,[18] Y. Seiya,[31] G. Sganos,[11] A. Sgolacchia,[2] M. Shapiro,[14] N. M. Shaw,[24] Q. Shen,[24] P. F. Shepard,[22] M. Shimojima,[31] M. Shochet,[5] J. Siegrist,[29] A. Sill,[7a] P. Sinervo,[11] P. Singh,[22] J. Skarha,[12] K. Sliwa,[32] D. A. Smith,[23] F. D. Snider,[12] L. Song,[7] T. Song,[16] J. Spalding,[7] L. Spiegel,[7] P. Sphicas,[15] A. Spies,[12] L. Stanco,[20] J. Steele,[33] A. Stefanini,[23] K. Strahl,[11] J. Strait,[7] D. Stuart,[7] G. Sullivan,[5] K. Sumorok,[15] R. L. Swartz, Jr.,[10] T. Takahashi,[19] K. Takikawa,[31] F. Tartarelli,[23] W. Taylor,[11] P. K. Teng,[28] Y. Teramoto,[19] S. Tether,[15] D. Theriot,[7] J. Thomas,[29] T. L. Thomas,[18] R. Thun,[16] M. Timko,[32] P. Tipton,[25] A. Titov,[26] S. Tkaczyk,[7] K. Tollefson,[25] A. Tollestrup,[7] J. Tonnison,[24] J. F. de Troconiz,[9] J. Tseng,[12] M. Turcotte,[29] N. Turini,[2] N. Uemura,[31] F. Ukegawa,[21] G. Unal,[21] S. van den Brink,[22] S. Vejcik, III,[16] R. Vidal,[7] M. Vondracek,[10] R. G. Wagner,[1] R. L. Wagner,[7] N. Wainer,[7] R. C. Walker,[25] C. H. Wang,[28] G. Wang,[23] J. Wang,[5] M. J. Wang,[28] Q. F. Wang,[26] A. Warburton,[11] G. Watts,[25] T. Watts,[27] R. Webb,[30] C. Wendt,[33] H. Wenzel,[14] W. C. Wester, III,[14] T. Westhusing,[10] A. B. Wicklund,[1] E. Wicklund,[7] R. Wilkinson,[21] H. H. Williams,[21] P. Wilson,[5] B. L. Winer,[25] J. Wolinski,[30] D. Y. Wu,[16] X. Wu,[23] J. Wyss,[20] A. Yagil,[7] W. Yao,[14] K. Yasuoka,[31] Y. Ye,[11] G. P. Yeh,[7] P. Yeh,[28] M. Yin,[6] J. Yoh,[7] T. Yoshida,[19] D. Yovanovitch,[7] I. Yu,[34]

J. C. Yun,[7] A. Zanetti,[23] F. Zetti,[23] L. Zhang,[33] S. Zhang,[16] W. Zhang,[21] and S. Zucchelli[2]

(CDF Collaboration)

[1] *Argonne National Laboratory, Argonne, Illinois 60439*

[2] *Istituto Nazionale di Fisica Nucleare, University of Bologna, I-40126 Bologna, Italy*

[3] *Brandeis University, Waltham, Massachusetts 02254*

[4] *University of California at Los Angeles, Los Angeles, California 90024*

[5] *University of Chicago, Chicago, Illinois 60637*

[6] *Duke University, Durham, North Carolina 27708*

[7] *Fermi National Accelerator Laboratory, Batavia, Illinois 60510*

[8] *Laboratori Nazionali di Frascati, Istituto Nazionale di Fisica Nucleare, I-00044 Frascati, Italy*

[9] *Harvard University, Cambridge, Massachusetts 02138*

[10] *University of Illinois, Urbana, Illinois 61801*

[11] *Institute of Particle Physics, McGill University, Montreal H3A 2T8, and University of Toronto, Toronto M5S 1A7, Canada*

[12] *The Johns Hopkins University, Baltimore, Maryland 21218*

[13] *National Laboratory for High Energy Physics (KEK), Tsukuba, Ibaraki 305, Japan*

[14] *Lawrence Berkeley Laboratory, Berkeley, California 94720*

[15] *Massachusetts Institute of Technology, Cambridge, Massachusetts 02139*

[16] *University of Michigan, Ann Arbor, Michigan 48109*

[17] *Michigan State University, East Lansing, Michigan 48824*

[18] *University of New Mexico, Albuquerque, New Mexico 87131*

[19] *Osaka City University, Osaka 588, Japan*

[20] *Universita di Padova, Istituto Nazionale di Fisica Nucleare, Sezione di Padova, I-35131 Padova, Italy*

[21] *University of Pennsylvania, Philadelphia, Pennsylvania 19104*

[22] *University of Pittsburgh, Pittsburgh, Pennsylvania 15260*

[23] *Istituto Nazionale di Fisica Nucleare, University and Scuola Normale Superiore of Pisa, I-56100 Pisa, Italy*

[24] *Purdue University, West Lafayette, Indiana 47907*

[25] *University of Rochester, Rochester, New York 14627*

[26] *Rockefeller University, New York, New York 10021*

[27] *Rutgers University, Piscataway, New Jersey 08854*

[28] *Academia Sinica, Taiwan 11529, Republic of China*

[29] *Superconducting Super Collider Laboratory, Dallas, Texas 75237*

[30] *Texas A&M University, College Station, Texas 77843*

[31] *University of Tsukuba, Tsukuba, Ibaraki 305, Japan*

[32] *Tufts University, Medford, Massachusetts 02155*

[33] *University of Wisconsin, Madison, Wisconsin 53706*

[34] *Yale University, New Haven, Connecticut 06511*

This paper presents a measurement of the mass of the W boson using data collected with the CDF detector during the 1992-93 collider run at the Fermilab Tevatron. A fit to the transverse mass spectrum of a sample of 3268 $W \rightarrow \mu\nu$ events recorded in an integrated luminosity of 19.7 pb^{-1} gives $M_W^{\mu} = 80.310 \pm 0.205$ (stat.) $\pm$ 0.130 (syst.) GeV/c^2. A fit to the transverse mass spectrum of a sample of 5718 $W \rightarrow e\nu$ events recorded in 18.2 pb^{-1} gives $M_W^{e} = 80.490 \pm 0.145$ (stat.) $\pm$ 0.175 (syst.) GeV/c^2. Combining the muon and electron results, accounting for correlated uncertainties, yields $M_W = 80.410 \pm 0.180$ GeV/c^2.

Section 1

INTRODUCTION

The relations among the masses and couplings of gauge bosons allow incisive tests of the Standard Model of the electroweak interactions [1]. These relations are precisely specified at Born level; higher-order radiative corrections, which are sensitive to the top quark mass, $M_{\rm top}$, and the Higgs boson mass, $M_{\rm Higgs}$, have also been calculated [2]. Measurements of the properties of the Z boson, as well as measurements of atomic transitions, muon decay, and deep-inelastic scattering, tightly constrain the relationship between allowed values of $M_{\rm top}$ and the W mass, M_W [3]. Precise measurements of M_W and of $M_{\rm top}$, if inconsistent with the allowed range of predictions, could indicate the existence of new phenomena at or above the electroweak scale. Alternatively, within the confines of the Standard Model, such measurements predict $M_{\rm Higgs}$. The measurement of the W mass is unique among electroweak measurements in its sensitivity to charged currents at large momentum transfer.

The direct measurement of the W mass has to date been possible only at the antiproton-proton colliders at CERN and Fermilab, accelerators with sufficient center-of-mass energy to produce the W. A summary of previously published measurements is given in Table 1.1. We present here a new measurement with a precision twice that of the best previously published value.

Experiment	Reference	Mode	Mass (GeV/c^2)
UA1-83	[4]	$e\nu$	81 ± 5
UA2-83	[5]	$e\nu$	80^{+10}_{-6}
UA1-84	[6]	$\mu\nu$	81^{+6}_{-7}
UA1-86	[7]	$e\nu$	83.5 ± 2.9
UA2-87	[8]	$e\nu$	80.2 ± 1.5
UA1-89	[9]	$\mu\nu$	81.8 ± 6.5
UA1-89	[9]	$\tau\nu$	$89 \pm 3 \pm 6$
CDF-89	[10]	$e\nu$	80.0 ± 4.1
UA2-90	[11]	$e\nu$	80.53 ± 0.49
CDF-90	[12]	$e\nu, \mu\nu$	79.91 ± 0.39
UA2-92	[13]	$e\nu$	80.36 ± 0.37

Table 1.1: Some previously published W mass measurements. Not all of the above measurements are independent. The mode is the decay channel of the W used in the measurement.

This paper describes the measurement of the W mass using W bosons observed in antiproton-proton ($\bar{p}p$) collisions produced at the Fermilab Tevatron with a center-of-mass energy of 1800 GeV. The results are from an analysis of the decays of the W into a muon and neutrino in a data sample of integrated luminosity of 19.7 pb^{-1}, and decays of the W into an electron and neutrino in an 18.2 pb^{-1} subset, collected by the Collider Detector at Fermilab (CDF) during the period from August 1992 to May 1993.

The paper is structured as follows. A description of the detector and an overview of the analysis are given in Section 2. The calibration and alignment of the central tracking chamber, which provides the momentum scale for the mass measurement, is described in Section 3. Sections 4, 5, and 6 are largely parallel: Section 4 describes muon identification and the determination of the momentum resolution; Section 5 describes electron identification, the transfer of the momentum scale to the calorimeter energy scale, and the determination of the energy resolution; Section 6 describes the determination of the

detector response to hadrons recoiling against the W in the event, necessary to infer the neutrino momentum scale. The knowledge of the lepton and recoil responses is incorporated in a Monte Carlo model of W production and decay, described in Section 7. Section 8 describes the effects of background processes and radiative corrections on the mass measurement. Section 9 gives details of the fitting method used to extract the W mass from a comparison of the data and the model. Each of these sections ends with a summary of numerical results. Section 10 presents a global summary of the measured values and the experimental uncertainties. Finally, the measured W mass is compared to previous measurements and current predictions.

Section 2

OVERVIEW

This section begins with a discussion of how the nature of W boson production and decay motivates the strategy used to measure the W mass. The aspects of the detector critical to the measurement are then described. A brief description of the data samples used for the calibrations and for the mass measurement follows. A summary of the analysis strategy concludes the section.

2.1 Nature of W Events

The dominant mechanism for production of W bosons in antiproton-proton collisions is predicted to be antiquark-quark annihilation, with additional contributions from higher-order diagrams [14]. The W is produced with momentum in the transverse and longitudinal directions relative to the center-of-mass of the antiproton-proton collision[1]. This momentum is balanced by the momentum of hadrons produced in association with the W, referred to as the "recoil", as illustrated in Figure 2.1.

[1]CDF uses a cylindrical coordinate system with the z (longitudinal) axis along the proton beam axis; r is the transverse coordinate, and ϕ is the azimuthal angle. Pseudorapidity (η) is defined as $\eta \equiv -ln(tan(\theta/2))$, where θ is the polar angle relative to the proton-beam direction. See Figure 2.2.

The W boson decays used in this analysis are the two-body leptonic decays producing an electron or muon and a neutrino. Since the apparatus cannot detect the neutrino and cannot measure the z-component of the recoil momentum, much of which is carried in fragments of the initial proton and anti-proton at small angles to the beams, there is insufficient information to reconstruct the invariant mass of the W on an event-by-event basis. Rather, this analysis uses the transverse mass of each W event, which is analogous to the invariant mass except that only the components of energy flow transverse to the beamline are used. Specifically,

$$(M_T^W)^2 = (E_T^\ell + E_T^\nu)^2 - (\mathbf{E}_T^\ell + \mathbf{E}_T^\nu)^2, \tag{2.1}$$

where M_T^W is the transverse mass of the W, E_T^ℓ is the transverse energy of the charged lepton (electron or muon), and E_T^ν is the transverse energy of the neutrino.[2] The boldface denotes two-component vector quantities. The transverse energy of the neutrino is not measured, but rather is inferred from momentum imbalance in the calorimeters,

$$\mathbf{E}_T^\nu = -(\mathbf{E}_T^\ell + \mathbf{u}), \tag{2.2}$$

where $\mathbf{u}$ denotes the transverse energy vector of the recoil (see Figure 2.1).

When $|\mathbf{u}| \ll E_T^\ell$, the transverse mass measurement of Equation 2.1 becomes

$$M_T^W \approx 2E_T^\ell + u_{||}, \tag{2.3}$$

where $u_{||}$ is the transverse energy of the recoil projected along the direction of the charged lepton, $(\mathbf{u}\cdot\mathbf{E}_T^\ell)/E_T^\ell$. The resolutions on the measurements of the charged lepton energy and the recoil must be understood to make adequate predictions of the transverse mass shape; the distribution in $u_\perp$, the component perpendicular to $u_{||}$, is used as a sensitive test of the adequacy of the

[2] Although energy is a scalar quantity, "transverse energy" commonly denotes the transverse component of the vector whose *magnitude* is the energy of the particle and *direction* is parallel to the momentum of the particle.

modeling. In addition, effects which systematically bias $u_{||}$ must be accounted for. The transverse mass is invariant to first order under Lorentz boosts in the transverse direction; uncertainties associated with the W boson transverse momentum spectrum enter into the mass measurement primarily through mismeasurements of the W recoil transverse energy, $\mathbf{u}$, and, to a lesser extent, through acceptance effects. Note that the approximation of Equation 2.3 is shown only to illustrate these points and that the true transverse mass is used everywhere in this analysis.

2.2 Detector

This section briefly describes those aspects of the CDF detector pertinent to the W mass measurement. A more detailed description can be found in Reference [15]; recent detector upgrades are described in References [16] and [17].

The CDF detector is an azimuthally and forward-backward symmetric magnetic detector designed to study $\bar{p}p$ collisions at the Tevatron. The magnetic spectrometer consists of tracking devices inside a 3-m diameter, 5-m long superconducting solenoidal magnet which operates at 1.4 T. The detector is divided into a central region ($30° < \theta < 150°$), end-plugs ($10° < \theta < 30°$, $150° < \theta < 170°$), which form the pole pieces for the solenoidal magnet, and forward/backward regions ($2° < \theta < 10°$, $170° < \theta < 178°$). Muon chambers are placed outside (at larger radius) of the hadronic calorimeters in the central region; toroidal steel magnets and chambers provide additional muon coverage and shielding on each end. An elevation view of one quarter of the CDF detector is shown in Figure 2.2.

2.2.1 Tracking Detectors

A four-layer silicon microstrip vertex detector (SVX) [17], used in this analysis to provide a precision measurement of the beam axis, is located directly outside the 1.9-cm radius beryllium beampipe. The four layers of the SVX are at radii of 3.0, 4.2, 5.7, and 7.9 cm from the beamline. Outside the SVX is a set of vertex time projection chambers (VTX) [18], which provides r-z tracking information out to a radius of 22 cm for $|\eta| < 3.25$. The VTX is used in this analysis for finding the z position of the antiproton-proton interaction (the event vertex). The event vertex is necessary for event selection, lepton track reconstruction, and the calculation of $\not\!\!E_T$. Both the SVX and VTX are mounted inside the central tracking chamber (CTC) [19], a 3.2-m long drift chamber that extends in radius from 31.0 cm to 132.5 cm. The CTC has 84 sampling wire layers, organized in 5 axial and 4 stereo "super-layers" [19]. Axial super-layers have 12 radially separated layers of sense wires, parallel to the z axis, that measure the r-ϕ position of a track. Stereo super-layers have 6 sense wire layers, with a $\sim 3^\circ$ stereo angle, that measure a combination of r-ϕ and z information. The stereo angle direction alternates at each stereo super-layer. Axial and stereo data are combined to form a 3-dimensional track. In this analysis, the electron or muon momentum is measured from the curvature, azimuthal angle, and polar angle of the track as the particle traverses the magnetic field. The CTC momentum measurement is the ultimate source of all energy calibrations in this experiment. Details of the calibration and alignment of the CTC are given in Section 3.

2.2.2 Calorimeters

The electromagnetic and hadronic calorimeters subtend 2π in azimuth and from -4.2 to 4.2 in pseudorapidity (η). The calorimeters are constructed with a projective tower geometry, with towers subtending ap-

proximately 0.1 in pseudorapidity by 15° in ϕ (central) or 5° in ϕ (plug and forward). Each tower consists of an electromagnetic calorimeter followed by a hadronic calorimeter at larger radius. The energies of central electrons, used in the mass measurement, are measured from the electromagnetic shower produced in the central electromagnetic calorimeter (CEM) [20]. The central calorimeter is constructed as 24 "wedges" in ϕ for each half of the detector ($-1.1 < \eta < 0$ and $0 < \eta < 1.1$). Each wedge has 10 electromagnetic towers, which use lead as the absorber and scintillator as the active medium, for a total of 480 CEM towers.[3] A proportional chamber measures the electron shower position in the ϕ and z directions at a depth of ~ 6 radiation lengths in the CEM [20]. For the purposes of triggering and data sample selection, the CEM calibrations are derived from testbeam data taken during 1984-85. To compensate for scintillator aging, the tower gains were corrected in March 1992 using Cesium-137 gamma-ray sources. Details of the calibration of the CEM are given in Section 5.

The central calorimeters also measure the energy flow of particles produced in association with the W. Outside the CEM is a similarly segmented hadronic calorimeter (CHA) [21]. Electromagnetic and hadronic calorimeters which use multi-wire proportional chambers as the active sampling medium extend this coverage to $|\eta| = 4.2$ [22]. In this analysis, however, the recoil energy is calculated only in the region of full azimuthal symmetry, $|\eta| < 3.6$. Understanding the response of these devices to the recoil from bosons is problematic as it depends on details of the flow and energy distributions of the recoil hadrons. Instead, the energy response to recoil energy is mapped out using $Z \rightarrow ee$ events. Details of the calibration of the calorimeters to recoil energy are given in Sections 6 and 7.

[3]There are actually only 478 physical CEM towers; the locations of two towers are used for the cryogenic penetrations for the magnet.

2.2.3 Muon Detectors

Four layers of drift chambers, embedded in the wedge directly outside (in radius) of the CHA, form the central muon detection system (CMU) [23]. The CMU covers the region $|\eta| < 0.6$. Outside of these systems there is an additional absorber of 0.6 m of steel followed by a system of four layers of drift chambers (CMP). Approximately 84% of the solid angle for $|\eta| < 0.6$ is covered by CMU, 63% by CMP, and 53% by both. Muons from W decay are required in this analysis to produce a track in the CMU that matches a track in the CTC. The CMP is used in this measurement only in the Level 1 and Level 2 triggers. Details of the muon selection and reconstruction are given in Section 4.

2.2.4 Trigger and Data Acquisition

The CDF trigger is a three-level system that selects events for recording to magnetic tape. The crossing rate of proton and antiproton bunches in the Tevatron is 286 kHz, with a mean interaction rate of 0.6 interactions per crossing at a luminosity of 3.6×10^{30} cm^{-2} sec^{-1}, typical of the data presented here. The first two levels of the trigger [24] consist of dedicated electronics with separate data paths from the data acquisition system. The third level [25], which is initiated after the event information is digitized and stored, uses a farm of commercial computers to reconstruct events. The overall rejection factors for each of the three levels are typically 600, 100, and 4, respectively. At Level 1, electrons are selected by the presence of a single calorimeter tower above a threshold; muons are selected by the presence of a track in the CMU, and where there is full coverage, also in the CMP. At Level 2, electrons from W decay can satisfy one of a number of triggers. Some require a track to be found in the r-ϕ plane by a fast hardware processor [26] and to match to a calorimeter cluster; others have no track requirement but

require a high-E_T cluster[24]. The muon Level 2 trigger requires a track with large transverse momentum (p_T) that matches to a muon chamber track. At Level 3, reconstruction programs that include three-dimensional track reconstruction identify high-p_T electrons or muons.

Events that pass the Level 3 triggers are sorted and recorded. A subset of events, typically those from rarer processes (such as W decay), is written to disk in a separate data stream as well as being recorded to magnetic tape with the bulk of the events. These events are reconstructed rapidly after the data are taken, and, being a smaller sample, are more easily available for analysis. All of the data samples below, with the exception of the inclusive electrons and the Υ samples, come from this data stream.

The data used in this anaysis come from a recorded integrated luminosity of 19.7 pb^{-1}[27]. A requirement that the data not have been recorded immediately after a long collision hall access, when the CEM phototube gains were unstable, removes 1.5 pb^{-1} from the electron sample.

2.3 Data Samples

Seven data samples are employed in this analysis. These are described briefly below and in more detail in subsequent sections as they are used. A list of the samples follows:

- **The $J/\psi \rightarrow \mu\mu$ sample.** A sample of $\sim 60,000$ $J/\psi \rightarrow \mu\mu$ candidates is used to determine the absolute momentum scale from a measurement of the J/ψ mass, and to set limits on systematic effects associated with track reconstruction.

- **The $\Upsilon \rightarrow \mu\mu$ sample.** A sample of ~ 2000 $\Upsilon \rightarrow \mu\mu$ candidates serves as a check on the momentum scale.

- **The $Z \rightarrow \mu\mu$ sample.** A sample of 330 dimuon events near the Z mass measures the momentum resolution from the width of the Z peak. The sample also serves as an additional check of the momentum scale.

- **The $W \rightarrow \mu\nu$ sample.** A sample of 3268 $W \rightarrow \mu\nu$ candidates is used to measure the W mass.

- **The inclusive electron sample.** A sample of $\sim 140,000$ central electrons with $E_T > 9$ GeV is used to understand the response of the central electromagnetic calorimeter (CEM) up to an overall normalization. A high-E_T subset of these events is used to align the CTC.

- **The $W \rightarrow e\nu$ sample.** A sample of 5718 $W \rightarrow e\nu$ candidates is used to set the absolute CEM energy scale from the momentum scale, and to measure the W mass.

- **The $Z \rightarrow ee$ sample.** A sample of 555 dielectron events near the Z mass is used to map out the response of the calorimeters to W boson recoil. A subset of this sample, 259 events where both electrons land in the CEM, measures the energy resolution and serves as a check of the energy scale.

2.4 Strategy of the Analysis

The determination of the momentum and energy scales[4] is crucial to the W mass measurement. Momentum is the kinematic quantity necessarily measured for muons; for electrons, the energy as measured in the calorimeter is the quantity of choice as it is much less sensitive than the momentum to the effects of bremsstrahlung [28]. The basic architecture of the CDF detector is a calorimeter behind a magnetic spectrometer. The spectrometer measures

[4]Throughout this paper, momentum measurements using the CTC are denoted as p, and calorimeter energy measurements are denoted as E.

the momentum of muons and electrons, and the calorimeter measures the energy of electrons. This configuration allows *in situ* calibrations of both the momentum and energy scales directly from the collider data. The alignment of the CTC wires is done with high momentum electrons, exploiting the charge independence of the electromagnetic calorimeter measurement (both positives and negatives should give the same momentum for a given energy). The momentum scale of the magnetic spectrometer is then calibrated using the reconstructed mass of the $J/\psi \rightarrow \mu\mu$ resonance. Conversely, the calorimeter is calibrated by normalizing the average calorimeter response to electrons (both e^+ and e^-) of a given momentum, exploiting the uniformity, stability, and linearity of the magnetic spectrometer. The momenta of lepton tracks from W decays reconstructed with the final CTC calibration typically change from the initial values used for data sample selection by less than 10%; the mean changes by less than 0.1%. The final CEM calibration differs tower-by-tower from the initial calibration on average by less than 1%, with an RMS spread of 3.5%.

The detector response to the recoil $|\mathbf{u}|$ is directly calibrated using $Z \rightarrow ee$ decays, in which the electron energies are well measured. This sample is used as a table from which one can look up the measured response $|\mathbf{u}|$ for a given p_T^Z. We assume that the response to the recoil from a Z of a given p_T is the same as that to the recoil from a W of the same p_T.

The observed transverse mass lineshape also depends on the transverse and longitudinal W momentum spectra, and the resolutions in momentum (for muons) and energy (for electrons). As an initial guess for the p_T^W spectrum, the observed $Z \rightarrow ee$ p_T spectrum, corrected for the effect of electron energy resolution, is used. This spectrum is tuned for consistency with the observed $u_\perp$ distribution. The longitudinal W momentum spectrum is constrained by restricting the choice of parton distribution functions to those consistent with the CDF W charge asymmetry measurement [29]. The mo-

mentum resolution is determined from the width of the $Z \rightarrow \mu\mu$ mass peak. The energy resolution is determined from the width of the $Z \rightarrow ee$ peak.

To extract the W mass, the measured W transverse mass spectrum is fit to transverse mass spectra simulated by Monte Carlo for a range of W masses and widths. Backgrounds are included in the simulated lineshapes. The mass shift due to electromagnetic radiative processes is calculated by Monte Carlo and is applied to the fitted mass. The uncertainties associated with known systematic effects are estimated by varying the magnitude of these effects within the Monte Carlo simulation and refitting the data.

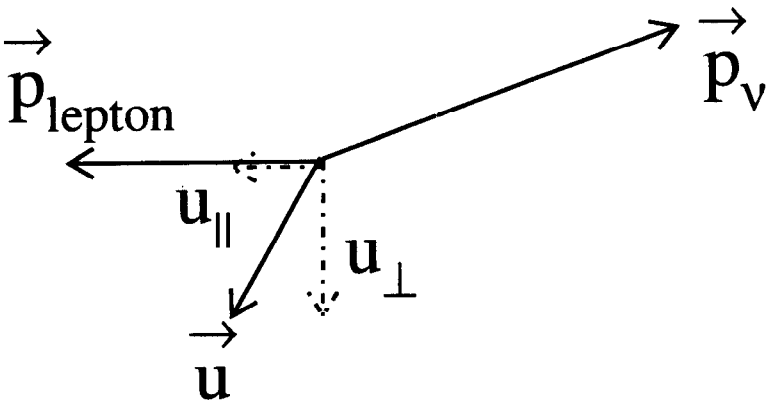

Figure 2.1: Kinematics of W boson production and decay for the events used in this analysis, as viewed in the plane transverse to the antiproton-proton beams. The vector **u** denotes the transverse energy vector of the recoil.

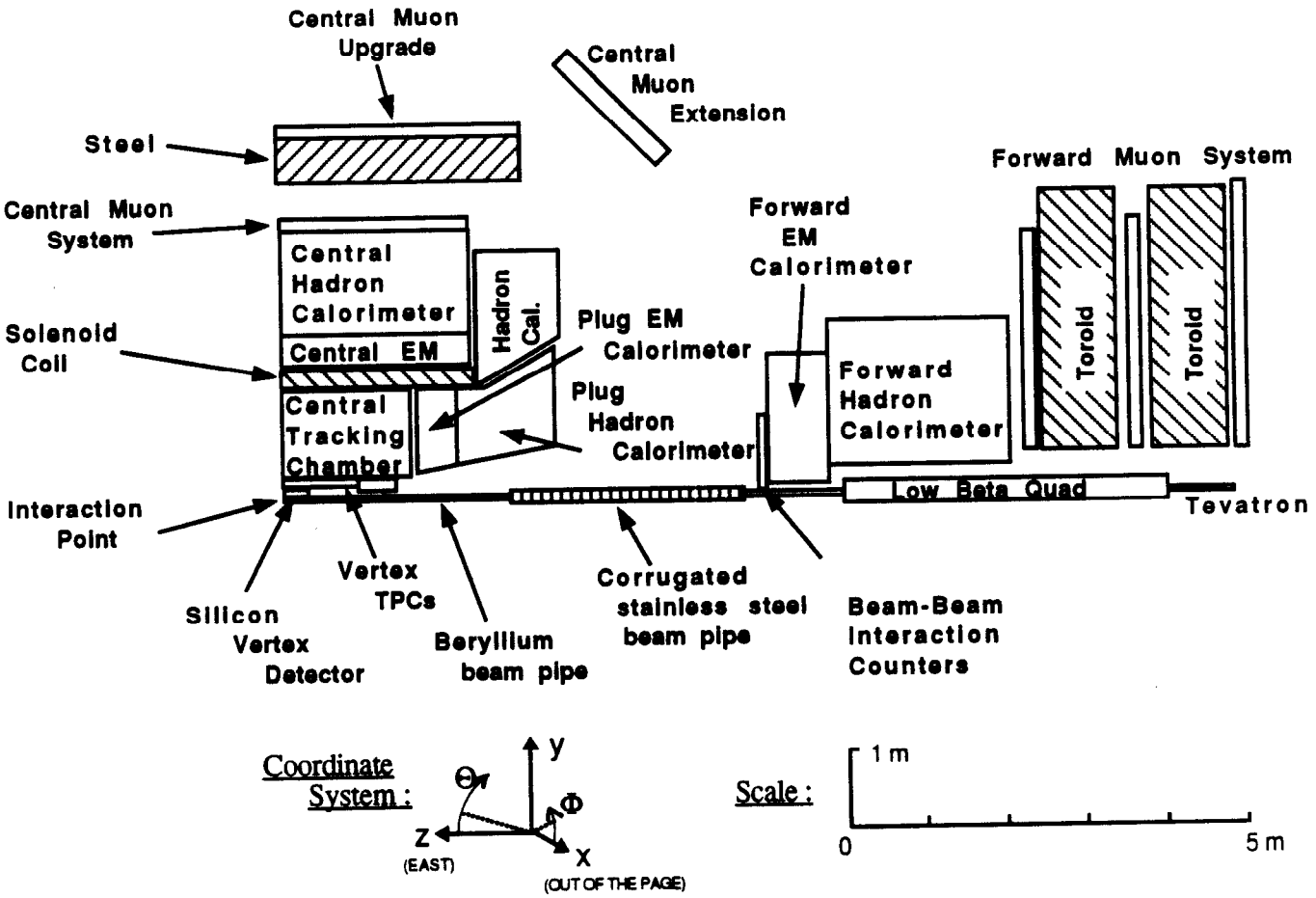

Figure 2.2: One quarter of the CDF detector. The detector is symmetric about the interaction point.

Section 3

MOMENTUM SCALE

In this section, the reconstruction of charged-particle trajectories and momenta using the central tracking chamber (CTC) is presented. The CTC calibration and alignment, and the determination of the absolute momentum scale using the $J/\psi \rightarrow \mu\mu$ resonance are described. Checks of the momentum scale from direct measurements of the $\Upsilon \rightarrow \mu\mu$ and $Z \rightarrow \mu\mu$ masses are given.

3.1 Track Reconstruction

The momentum of a charged particle is determined from its trajectory in the CTC. The CTC is operated in an axial magnetic field, uniform to within $\sim$1%. In a uniform field charged particles follow a helical trajectory. This helix is parametrized by: curvature, C (inverse diameter of the circle in r-ϕ); impact parameter, D_0 (distance of closest approach to $r = 0$); ϕ_0 (azimuthal direction at the point of closest approach to $r = 0$); z_0 (the z position at the point of closest approach to $r = 0$); and $\cot\theta$, where θ is the polar angle. The helix parameters are determined taking into account the non-uniformities of the magnetic field using the magnetic field map (see Section 3.3). The absolute

scale of the magnetic field was measured by inserting an NMR probe into a precise point in the tracking volume at the end of the data-taking period [30].

The momentum resolution is improved by a factor of two by constraining tracks to originate from the interaction point in the r-ϕ plane (the "beam constraint"). The z location of the interaction point (the 'event vertex') is determined by the VTX for each event with a precision of 1 mm. The distribution of event vertices has an RMS spread of 25−30 cm, depending on accelerator conditions. The r-ϕ location of the beam axis is measured by the SVX as a function of z with a precision of 10 μm. The beam axis is tilted with respect to the CTC axis by a slope that is about 400 microns per meter.

The measured muon momenta from $J/\psi \rightarrow \mu\mu$ decay are corrected for ionization energy loss (dE/dx) in traversing the $(8.9 \pm 0.9)\%$ of a radiation length of material (X_o) between the event vertex and the CTC tracking volume (See Section 5.6). The correction for this energy loss is negligible for the $W \rightarrow \mu\nu$ mass measurement, but is significant for the precision reconstruction of the J/ψ mass, used to normalize the momentum scale. For electrons, the effect of bremsstrahlung is not included in the electron track reconstruction, but is dealt with in the procedure used to transfer the momentum scale to the calorimeter energy scale, discussed in Section 5.

3.2 Calibration and Alignment

The CTC calibration and alignment proceeds in three steps. First, the relationship between the measured drift time and the distance to the sense wire is established. Second, the relative alignment of wires and layers in the CTC is performed. The final step is a fine-tuning of the alignment.

3.2.1 Time-to-distance calibration

Electronic pulsing, performed periodically during the data-taking period, gives relative time pedestals for each sense wire. Variations in drift properties for each super-layer are removed run-by-run [31]. Additional corrections for non-uniformity in the drift trajectories are made based on data from many runs. For each primary vertex found by the VTX, an interaction time is measured from the associated tracks. This procedure accounts for the variation of the interaction time, as well as for any drift in cable delays. After calibration, the CTC drift-distance resolution is determined to be 170 μm (outer layers) to 220 μm (inner layers), to be compared with $\sim$ 120 μm expected from diffusion alone, and $\sim$ 200 μm expected from test-chamber results.

3.2.2 Wire and layer alignment

The initial individual wire positions are taken to be the nominal positions determined during the CTC construction [19]. The distribution of differences between these nominal positions and the positions determined with an optical survey has an RMS of 25 μm. The 84 layers of sense wires are aligned relative to each other by requiring the ratio of energy to momentum E/p for electrons to be independent of charge.[1] A sample of about 10,000 inclusive electrons with $E_T > 18$ GeV is used for this alignment procedure. The alignment consists of rotating each entire layer on each end of the CTC by a different amount $r \times \Delta\phi$. The measured deviation of each layer from its nominal position after this alignment is shown in Figure 3.1.

3.2.3 Fine-tuning

The $W \rightarrow e\nu$ mass sample (see Section 5.3) is used to fine-tune the CTC alignment. The fine-tuning removes residual global ϕ-dependent and θ-

[1] For convenience, the requisite factor of c is dropped in the ratio E/p.

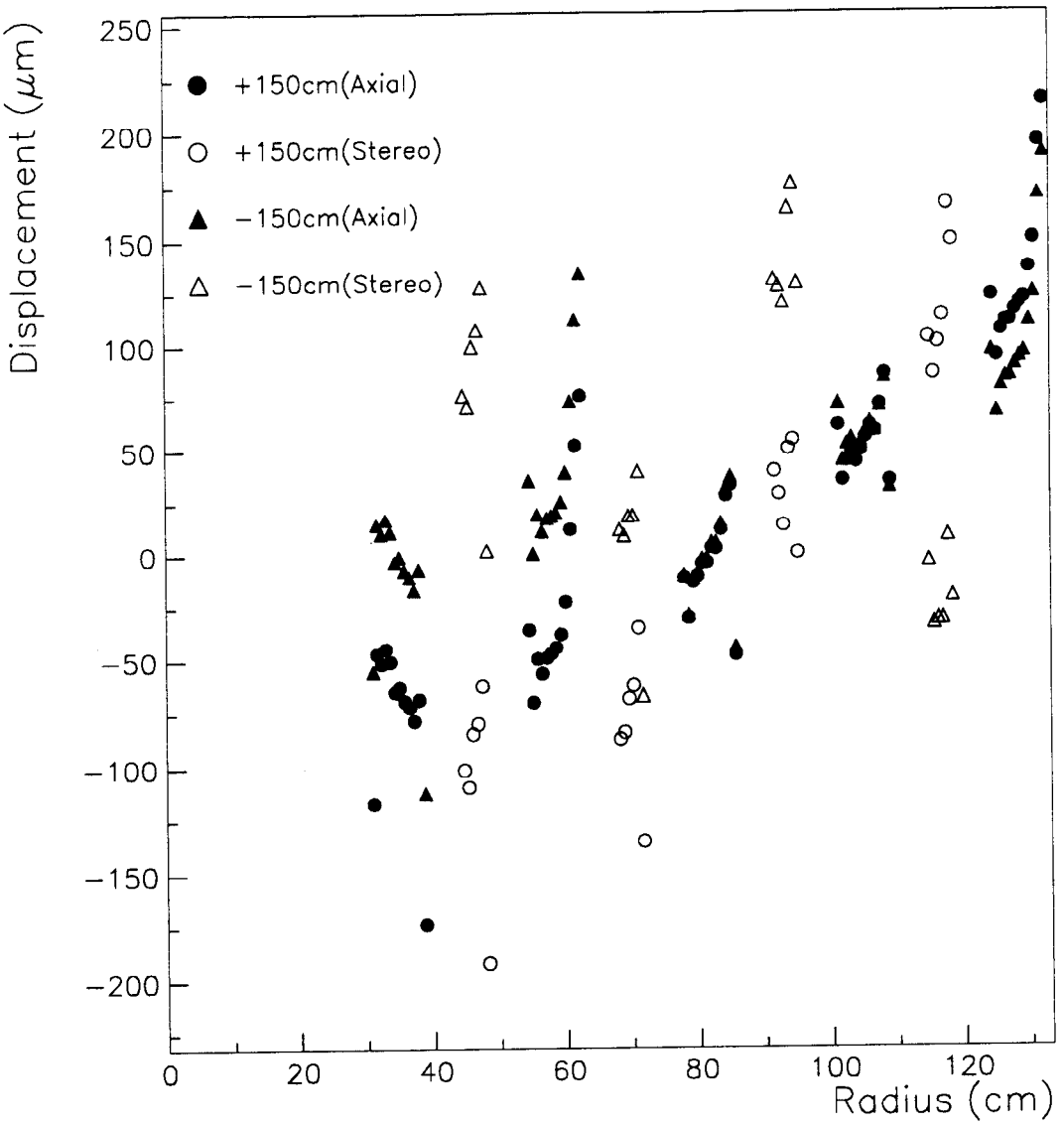

Figure 3.1: The deviation ($r \times \Delta\phi$) of each CTC layer from its nominal position at the end plates ($|z| = 150$ cm), versus the radius of the layer, r.

dependent charge splittings of $< E/p >$, using many fewer parameters than the CTC layer alignment. The overall difference in $< E/p >$ for the e^+ and e^- in this sample is $(0.06 \pm 0.12)\%$, which is consistent with zero. Note that a 0.12% difference in $< E/p >$ corresponds to a curvature distortion equivalent to displacing the outermost wire layer by about 8 μm in azimuth. A ϕ-modulated charge difference in $< E/p >$, which results from a residual misalignment of the CTC with respect to the beam axis, is observed. This modulation is removed with a correction of the form

$$\delta(1/p_T) = -0.00025 \times \sin(\phi - \phi_0), \tag{3.1}$$

where ϕ_0 is 3.6 radians and the coefficient corresponds to a beam position displacement of 30 ± 10 μm. A residual charge difference in $< E/p >$ that varies with z and θ is also observed. Assuming this is due to a rotation at each endplate of the outer radius of the CTC with respect to the inner radius, a correction of the form

$$\delta(1/p_T) = -0.00035 \times (\cot\theta + z_{\text{vertex}}/187), \tag{3.2}$$

with z_{vertex} in centimeters, is used. This corresponds to a curvature distortion equivalent to a wire displacement (at $\cot\theta = 1.0$, using $z_{\text{vertex}} = 0$) of 80 ± 25 μm. Other reasonable models of CTC twist could have been used without a significant difference in the correction.

Residual misalignments of the CTC wires can cause a systematic error on the W mass. Specifically, a residual modulation in θ, such as the one described in Equation 3.2, would introduce a momentum scale bias arising from the forward-backward charge asymmetry in W decay [32]. The systematic uncertainty due to the residual θ-dependence is studied using the simulation described in Section 7. Residual misalignments consistent with the statistical precision on the parameters in Equation 3.2 could contribute up to a 0.02% scale uncertainty, corresponding to 15 MeV/c^2 on the W mass. This is taken

Effect	Uncertainty (MeV/c^2)
Statistics	0.1
Muon energy loss before tracking	1.3
Beam constraint	0.3
Opening polar angle effect	—
Residual field non-uniformity	0.6
Background	0.1
Time variation	0.5
Radiative decay	0.2
Uncertainty in world-average $M_{J/\psi}$	0.1
SUBTOTAL	1.6
Extrapolation from $M_{J/\psi}$ to M_W	0.9
TOTAL	1.8

Table 3.1: Uncertainties on using the J/ψ mass to set the momentum scale for electrons and muons from W decays, expressed as the uncertainty on the J/ψ mass in MeV/c^2. The tabulation includes the uncertainty incurred when extrapolating from tracks in J/ψ decays to tracks with zero curvature.

as an uncertainty common to the electron and muon analyses. Figure 3.2 shows the E/p distributions for e^+ and e^- after all alignments.

3.3 Momentum Scale Determination

The momentum scale is determined by normalizing the observed $J/\psi \rightarrow \mu\mu$ peak to the world-average mass [34]. The invariant mass spectrum of 60,000 muon pairs from J/ψ decay is shown in Figure 3.3. A list of the systematic uncertainties on using the J/ψ mass to set the momentum scale is given in Table 3.1. The tabulation includes the uncertainty incurred when extrapolating from the momenta characteristic of J/ψ decay to the momenta of leptons from W decays, expressed as an uncertainty on the J/ψ mass. The entries in the table are described below in the order they appear.

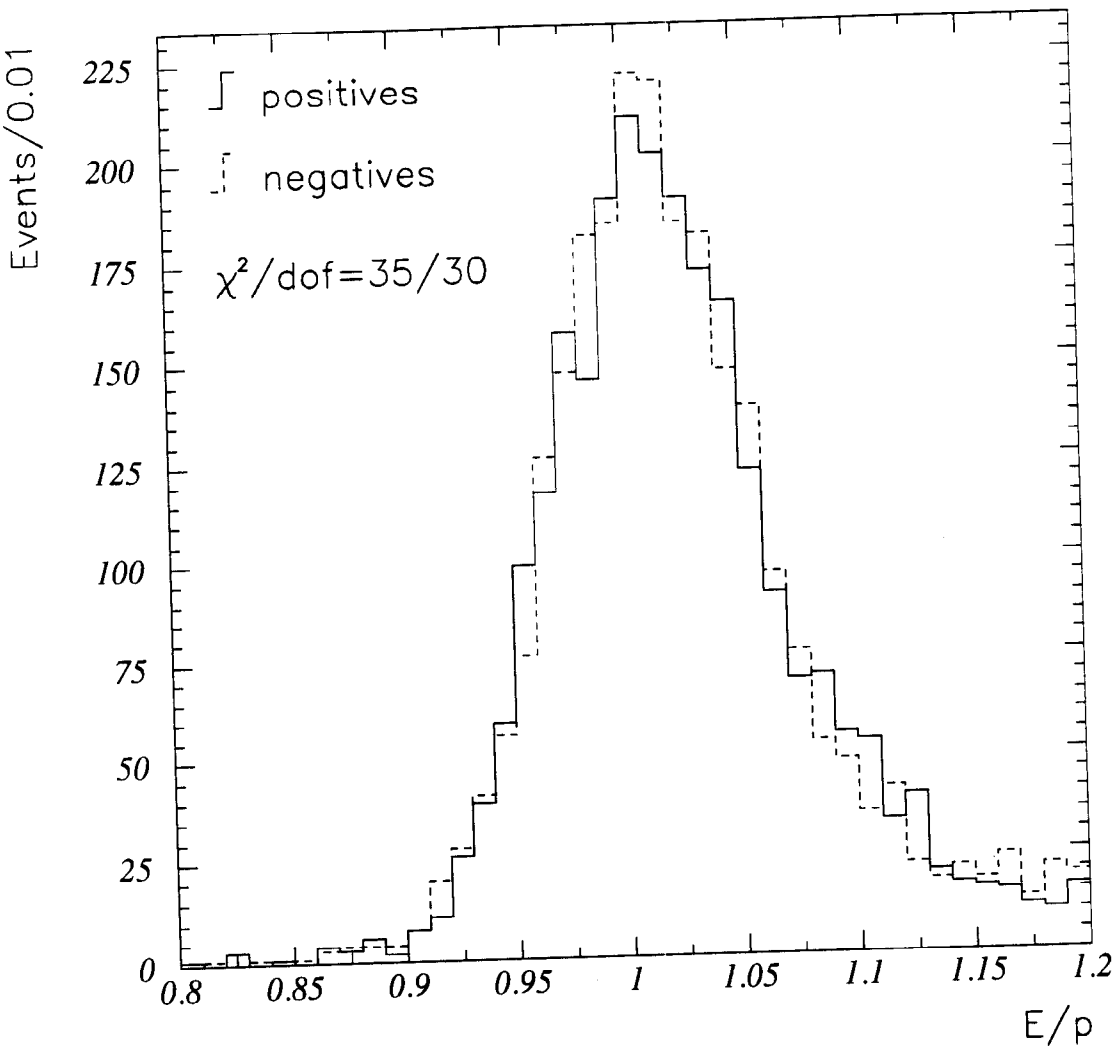

Figure 3.2: The ratio of E/p for central e^+ (solid) and e^- (dashed) in the $W \rightarrow e\nu$ sample after all CTC alignments and the beam constraint. The energy, E, used is calculated after all CEM calibrations have been performed [33].

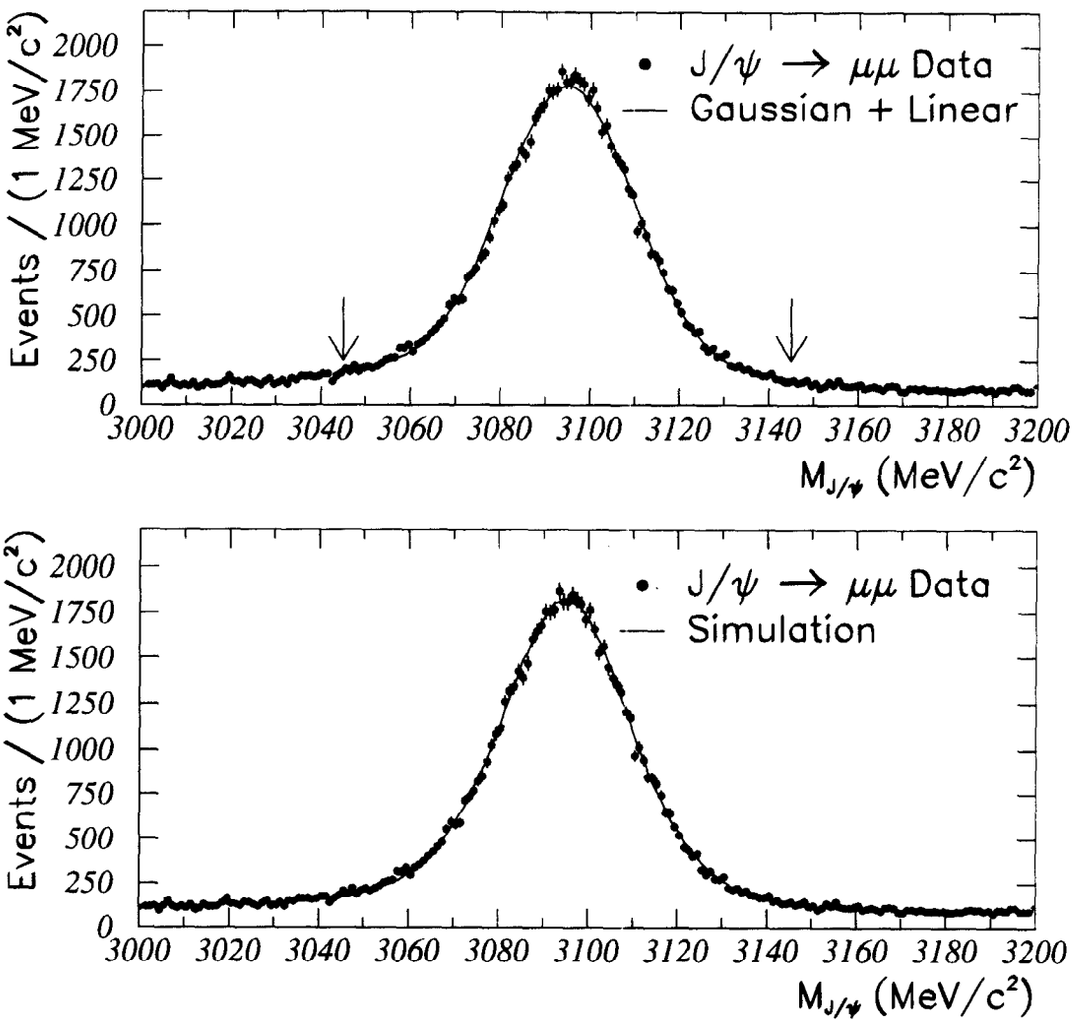

Figure 3.3: The measured dimuon mass spectrum (points), near the J/ψ mass in a 200 MeV/c^2 window. Upper: The curve is a Gaussian fit with a linear background in a 100 MeV/c^2 window. The arrows delimit the fit region. Lower: The curve is a Monte Carlo simulation including radiative effects.

Statistics: The J/ψ data are fit to a Gaussian with a linear background in a 100 MeV/c^2 window centered on the world-average mass. The fit determines the mean with a statistical accuracy of 0.1 MeV/c^2. Fits using wider windows yield shifts in the mass consistent with expected shifts due to the radiative tail. A fit to the shape derived from a simulation that includes radiative effects gives a consistent result (see Figure 3.3).

Muon Energy Loss: The momentum of each muon is corrected for energy loss in the material traversed by the muon. The amount of material is measured in radiation lengths from the tail of the E/p distribution for W electrons (see Section 5). For a given radiation length, the muon energy loss has a dependence on the type of material. A correction is made to the J/ψ mass based on the measured material. An uncertainty is calculated from the uncertainty in the amount and the type of material. The J/ψ mass correction due to energy loss is 3.7 ± 1.2 MeV/c^2.

Beam Constraint: Since many J/ψ mesons come from decays of B mesons, which decay some distance from the primary vertex, the measured J/ψ peak may be shifted by the application of the beam constraint. The difference in the J/ψ mass between a fit using the beam constraint and a fit using only a constraint that the two muons originate from the same point is 0.3 MeV/c^2. This difference is taken as an uncertainty.

Opening Polar Angle: A dependence of the measured J/ψ mass on the opening polar angle ($\Delta \cot\theta = \cot\theta_{\mu^+} - \cot\theta_{\mu^-}$) between the two muons is observed (see Figure 3.4). For the purpose of studying the systematics on the J/ψ mass only, the stereo angle dependence is reduced by scaling $\cot\theta$ as follows:

$$\cot\theta\ (scaled) = 0.999 \times \cot\theta. \tag{3.3}$$

The W mass measurement (as opposed to the J/ψ mass measurement) does

not use this $\cot\theta$ scaling since only the scale for transverse momentum is critical [35]. To keep the momentum scale determination independent of polar-angle effects, the mass is fitted versus $\Delta\cot\theta$ to a quadratic and the value at $\Delta\cot\theta = 0$ is used to determine the J/ψ mass [36].

Residual Field Non-Uniformity: The variations of the magnetic field both in magnitude and direction are small within the CTC active volume; $|\mathbf{B}(\mathbf{r}) - B(0)\,\hat{\mathbf{z}}|/B(0)$ has a maximum value of a few percent, occurring at the outer radius of the endplates of the CTC. Corrections to the track parameters for the field non-uniformity are based on a mapping of the field done in 1986, using a rotating search coil at a solenoid current of 5000 A [37]. During the data-taking period, the solenoid was actually run at a current of 4650 A. Due to saturation in the iron return yoke, the magnetic field is not exactly proportional to the solenoid current. A model of the iron structure and its saturation properties is used to correct for this, with the largest deviation from a simple scaling by 4650/5000 being 0.2% near the outer edge in z of the CTC. The model has been checked using search coil data taken at a few points with the solenoid at 4500 A, with agreement to within the measurement uncertainty of 2×10^{-4} T. The effect of the combined mapping and saturation corrections on the J/ψ mass is shown in Figure 3.5, as a function of $\cot\theta_{\mu^+} + \cot\theta_{\mu^-}$. The effects of any residual field non-uniformity are sought by looking at the variation of the J/ψ mass as a function of $\Sigma z^2 = z_{\mu^+}^2 + z_{\mu^-}^2$, where z is the track position at a radius of 100 cm. The mass is plotted as a function of Σz^2 in Figure 3.5 and the deviations are fit to a line [38]. The difference across the fit region is 0.6 MeV/c^2, which is taken as the uncertainty on the J/ψ mass.

Background: The uncertainty of the measured J/ψ mass due to uncertainty in the background shape is estimated by fitting both linear and quadratic background shapes to the data. It is determined to be less than 0.1 MeV/c^2.

Time Variation: An unexplained time variation of the J/ψ mass is observed

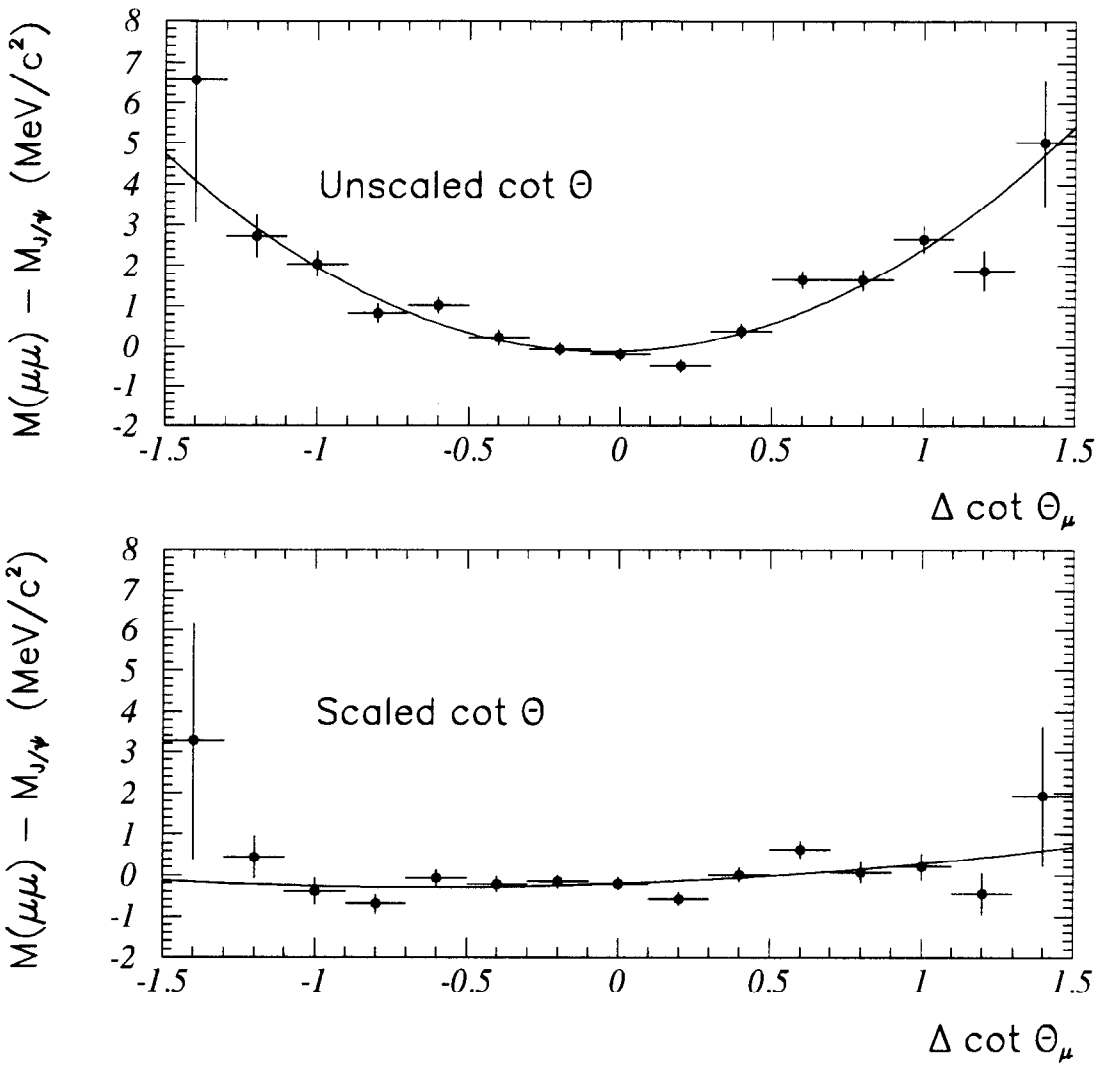

Figure 3.4: The variation of the measured J/ψ mass with $\Delta \cot\theta$ before (Upper) and after (Lower) scaling $\cot\theta$. The lines represent a quadratic fit.

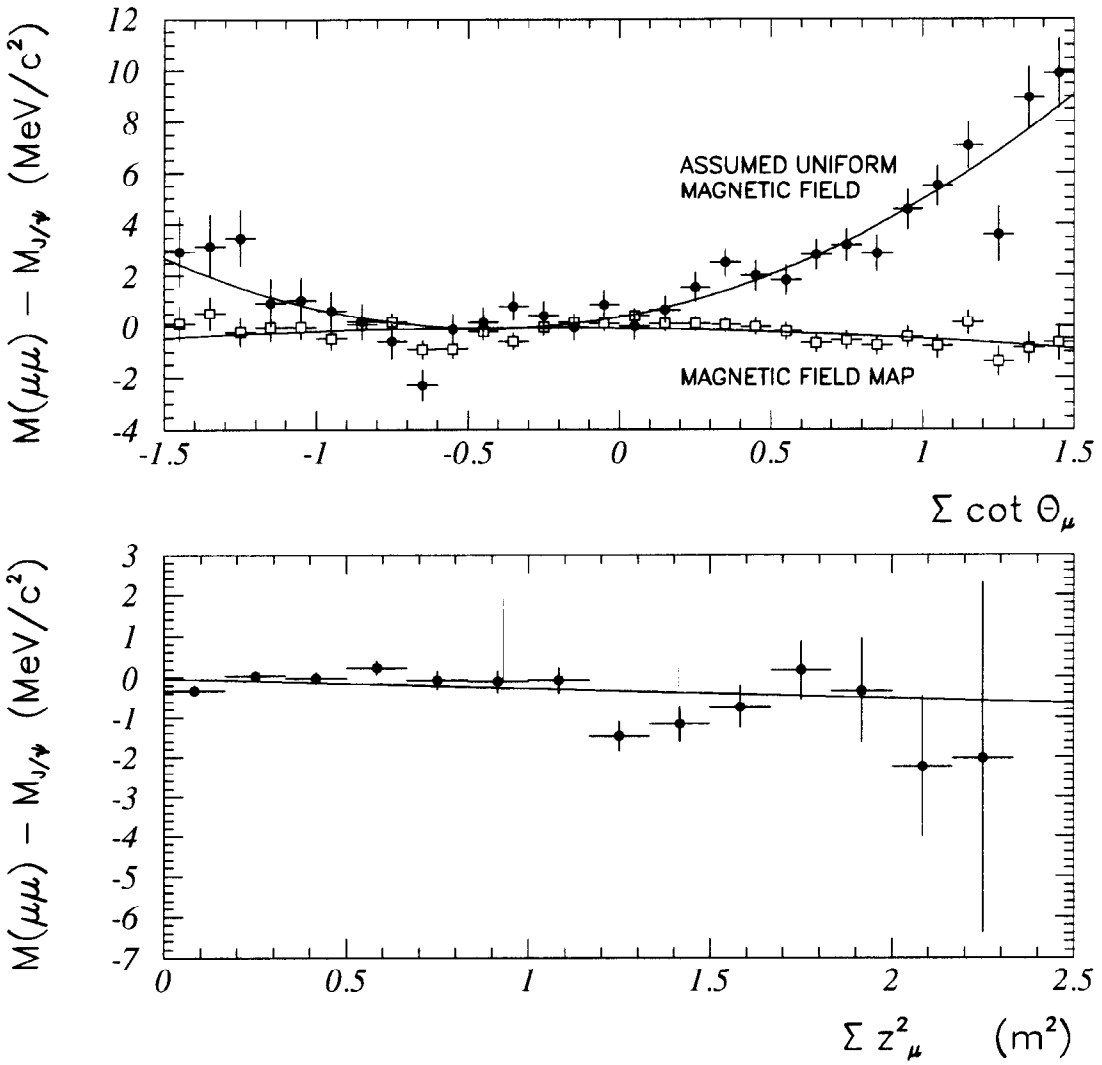

Figure 3.5: Upper: The variation of the measured J/ψ mass with $\cot\theta_{\mu^+} + \cot\theta_{\mu^-}$ before (solid) and after (open) applying the magnetic field map correction. Lower: The variation of the measured J/ψ mass with $\Sigma\ z^2 = z^2_{\mu^+} + z^2_{\mu^-}$ where z is measured at a radius of 100 cm.

over the data-taking period as shown in Figure 3.6. The RMS deviation, 0.5 MeV/c^2, is taken as a systematic uncertainty. If this variation is due solely to changes in the magnetic field, then the effect is properly averaged by the procedure of setting the momentum scale, and no uncertainty would need to be taken.

Radiative Decay: The measured mass must be corrected for QED radiative effects in J/ψ decay. The correction is determined using Monte Carlo simulation (see Figure 3.3) to be 0.56 ± 0.20 MeV/c^2. The systematic uncertainty represents possible variations from kinematics, modeling of resolutions, fitting procedures, and the background shape.

Uncertainty in the World-Average $M_{J/\psi}$: The uncertainty in the world-averaged J/ψ mass, 0.04 MeV/c^2, is included [34].

Extrapolation from $M_{J/\psi}$ to M_W: The momentum scale is set using muons from J/ψ decays in which the average muon p_T is $\sim$ 3 GeV/c. The average muon p_T from W decay is $\sim$ 38 GeV/c. However, the CTC does not directly measure momentum, but curvature, *i.e.*, inverse momentum, for which the difference between the J/ψ and the W is much smaller than the range in the J/ψ data. The most likely forms for non-linearity in the CTC momentum measurement are linear in the average $1/p_T^2$ of the two muons [39]. Figure 3.7 shows the variation of mass with the average $1/p_T^2$ of the two muons, before and after the scaling of cot θ given in Equation 3.3. Fitting a line and extrapolating from $< 1/p_T^2 >= 0.14$ (GeV/c)$^{-2}$ to $< 1/p_T^2 >= 0$ gives the systematic uncertainty due to non-linearity. To be conservative, the non-linearity measured before scaling by cot θ is used. The extrapolation yields an uncertainty of 0.9 MeV/c^2 when expressed as an uncertainty on the J/ψ mass.

The uncorrected measured value for the J/ψ mass, extracted by fitting the data in Figure 3.3 (see Section 3.3) and applying energy-loss and

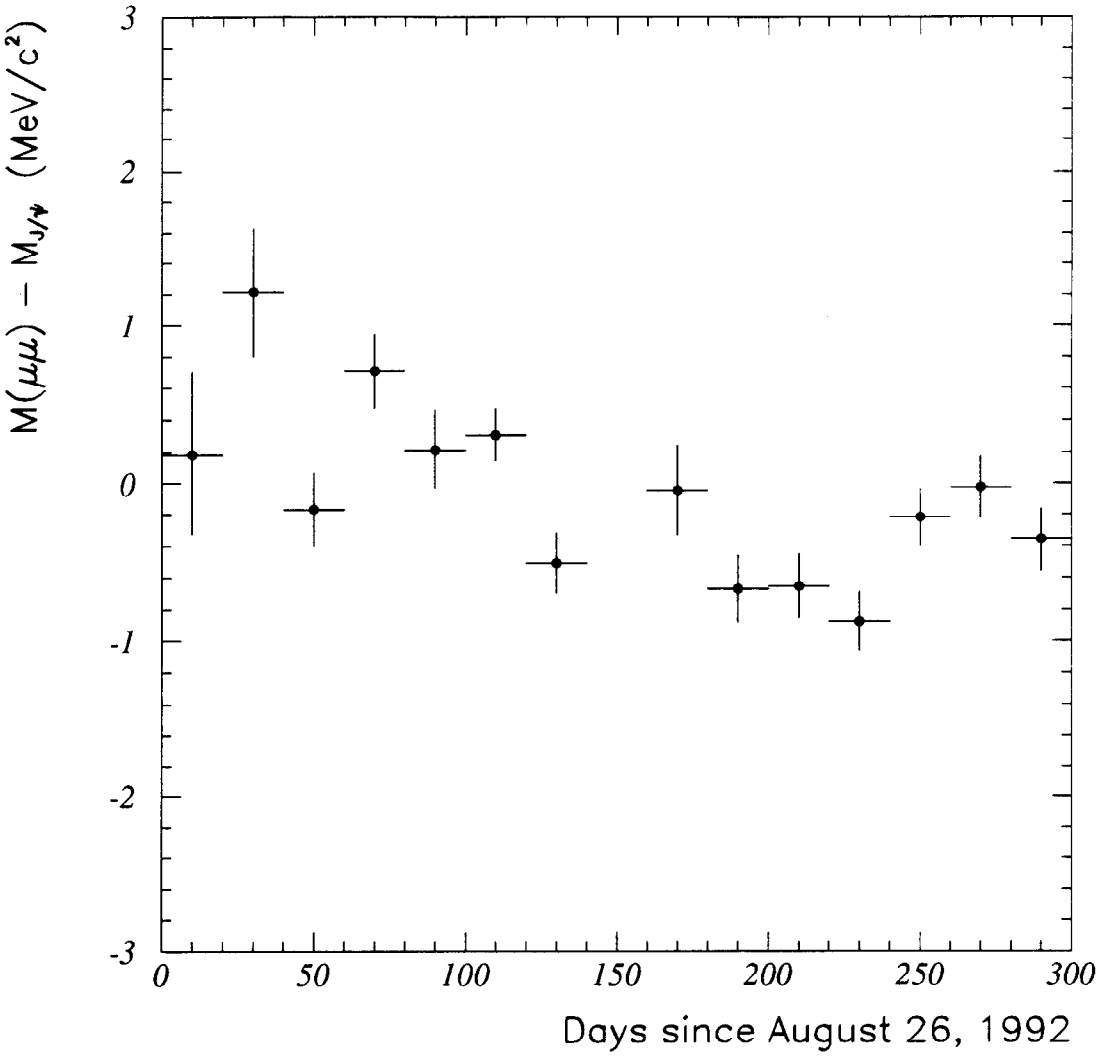

Figure 3.6: Variation of the measured J/ψ mass with time.

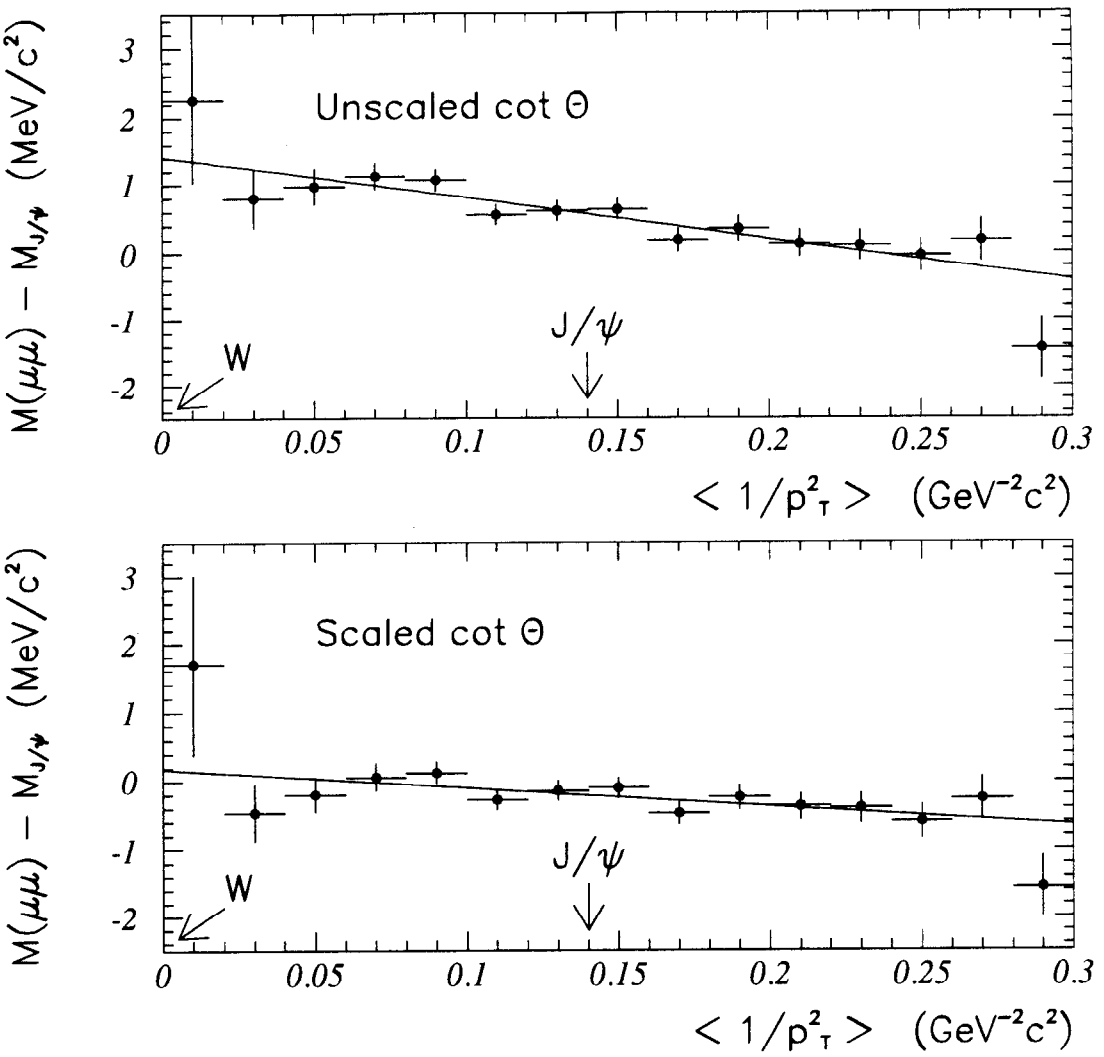

Figure 3.7: Variation of the measured J/ψ mass with the average of $1/p_T^2$ for the two muons. The leptons from W decays would lie in the first bin of this plot (0.001 $(\mathrm{GeV/c})^{-2}$). The average for J/ψ decays is 0.14 $(\mathrm{GeV/c})^{-2}$. The upper plot is before the cot θ scaling; the lower plot is after. The slope in the lower plot is a factor of two smaller.

Resonance	Corrected Mass (MeV/c^2)	World-Average Mass (MeV/c^2)
$\Upsilon(1S) \to \mu\mu$	$9460 \pm 2 \pm 6$	9460.4 ± 0.2
$\Upsilon(2S) \to \mu\mu$	$10029 \pm 5 \pm 6$	10023.3 ± 0.3
$\Upsilon(3S) \to \mu\mu$	$10334 \pm 8 \pm 6$	10355.3 ± 0.5
$Z \to \mu\mu$	$91020 \pm 210 \pm 55$	91187 ± 7

Table 3.2: Measured masses of the $\Upsilon \to \mu\mu$ and $Z \to \mu\mu$ resonances compared to the published values [34]. The first uncertainty on the corrected value is from statistics. The second is the systematic uncertainty from the momentum scale.

radiative corrections, is 3097.3 ± 1.6 MeV/c^2. The momentum scale is corrected by a factor of 0.99984 ± 0.00058 for the J/ψ mass to agree with the world average of 3096.88 ± 0.04 MeV/c^2 [34], where the uncertainty on the correction factor includes the term accounting for the extrapolation to the W mass. This corresponds to a correction of -11 ± 50 MeV/c^2 at the W mass.

3.4 Checks

The mass peaks of the first three Υ resonances are shown in Figure 3.8. These check the CTC momentum scale using pairs of tracks with larger opening angles than in $J/\psi \to \mu\mu$ decays. The measured mass values, after the absolute scale determination and a QED radiation correction of $+3 \pm 1$ MeV/c^2, are shown in Table 3.2. The agreement for the 1S and 2S masses is good; the value for the 3S peak shows a marginal discrepancy. Note that the 3S peak area is dominated by background.

The mass of the Z boson measured in $Z \to \mu\mu$ decays checks the momentum scale using tracks with curvatures comparable to those used to measure the W mass. The measurement is limited by the finite statistics in the peak. The measurement, described in detail in Section 4, includes the

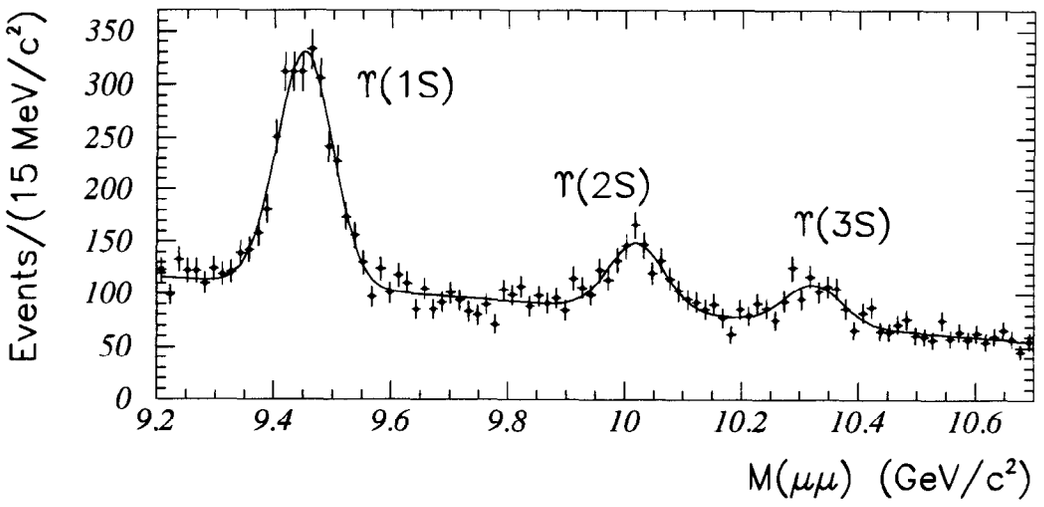

Figure 3.8: The dimuon mass spectrum near the Υ mass. The fits are Gaussians with a quadratic background.

effects of Drell-Yan interference, radiative decays ($Z \rightarrow \mu\mu\gamma$) and the detector resolutions discussed in Section 7. The measured value, $M_Z = 91.02 \pm$ 0.21 (stat.) $\pm$ 0.07 (syst.) GeV/c^2, is in good agreement with the LEP result of $M_Z = 91.187 \pm 0.007$ GeV/c^2 [34]. The tracking resolution is extracted simultaneously with the momentum scale; the result is given in the following section.

3.5 Summary

The absolute momentum scale is determined by normalizing the measured J/ψ mass to the world-average mass. The momentum scale needs to be corrected by a factor of 0.99984 ± 0.00058. A 50 MeV/c^2 systematic uncertainty in the W mass measurement is ascribed to the procedure. The possibility of remaining misalignments adds a 15 MeV/c^2 uncertainty to the W mass measurement.

Section 4

MUON MEASUREMENT

A description of muon reconstruction is given. The $W \rightarrow \mu\nu$ and $Z \rightarrow \mu\mu$ event samples are described. The momentum resolution is extracted from the width of the $Z \rightarrow \mu\mu$ peak and the momentum scale is checked from the measured Z mass.

4.1 Muon Identification

The W mass analysis uses muons traversing the central muon system (CMU), which consists of four layers of drift cells directly outside (in radius) the central hadron calorimeters (CHA), covering the region $|\eta| < 0.6$. Muon tracks in the CMU are reconstructed using the drift chamber time-to-distance relationship in the transverse (ϕ) direction, and charge division in the longitudinal (z) direction. Resolutions of 250 μm in the drift direction and 1.2 mm in z are determined from cosmic-ray studies [23]. Track segments consisting of hits in at least three layers are found separately in the r-ϕ and r-z planes. These two sets of segments are merged and a linear fit is performed to generate three-dimensional track segments.

Muons from W or Z decays are identified in the following manner.

To be considered a muon candidate, the muon track in the CTC must have p_T greater than 18 GeV/c. The track is extrapolated to the muon chambers (CMU) through the electromagnetic and hadronic calorimeters. There are approximately five hadronic absorption lengths of material between the CMU and the CTC. The muon extrapolation must match to a track segment in the CMU. The $r \times \Delta\phi$ matching is required to be within 2 cm; the RMS spread of the matching is 0.5 cm. In addition, the muon is required to have an energy deposit in the calorimeters consistent with that of a high-p_T muon. The energy in the CEM tower(s) traversed by the muon, which is 0.3 GeV on average, must be less than 2 GeV; the energy in the CHA tower(s), which is 2 GeV on average, must be less than 6 GeV.

To increase the number of $Z \rightarrow \mu\mu$ events, one of the two muons is not required to have a track segment in the muon chambers, but is only required to have an energy deposit in the calorimeters consistent with that of a high-p_T muon. This allows muon acceptance out to $|\eta| \sim 1.0$.

4.2 $W \rightarrow \mu\nu$ Sample

The event sample selection for the $W \rightarrow \mu\nu$ mass measurement is intended to produce a sample with low background and with well-understood muon and neutrino kinematics. The selection yields a sample that can be accurately modelled by simulation, and also preferentially selects those events with the best resolution on the transverse mass. The $W \rightarrow \mu\nu$ sample extraction begins with 11748 events that pass a Level 3 high-p_T muon trigger and satisfy the requirements on the muon and neutrino of $p_T^\mu > 18$ GeV/c and $E_T^\nu > 18$ GeV. From these, a final sample is selected with the criteria listed in Table 4.1. The event vertex chosen is the one reconstructed by the VTX to be closest in z to the origin of the muon track, and is required to be within 60 cm in z of the origin of the detector coordinates. To reduce backgrounds

Criterion	Events Remaining
Initial Sample	11748
$\lvert z_{\text{vertex}} \rvert < 60$ cm	11127
$p_T^\mu > 25$ GeV/c	7612
$E_T^\nu > 25$ GeV	6797
$\lvert D_o \rvert < 0.2$ cm	6155
$\lvert z_{\text{vertex}} - z_{\text{track}} \rvert < 2$ cm	5754
No other tracks with $p_T > 10$ GeV/c	4972
No jets with $E_T > 30$ GeV	4839
$\lvert \mathbf{u} \rvert < 20$ GeV	4663
Fit region: $65 < M_T^W < 100$ GeV/c^2	3268

Table 4.1: Criteria used to select the $W \rightarrow \mu\nu$ sample.

from heavy flavor and other jet production, as well as from $W \rightarrow \tau\nu$ decays, p_T^μ and E_T^ν are required to be greater than 25 GeV. To reduce background from cosmic rays, the following two cuts are applied. First, the muon track must satisfy $|D_o| < 0.2$ cm, where D_o is the impact parameter in the r-ϕ plane of the muon track with respect to the origin of the detector[1]. Second, the muon track must satisfy $|z_{\text{vertex}} - z_{\text{track}}| < 2$ cm, where z_{track} and z_{vertex} are the z position of the muon track and of the vertex closest to the muon track, respectively. These criteria also remove some muons which come from the decay-in-flight of pions and kaons. Backgrounds from $Z \rightarrow \mu\mu$ and remaining cosmic rays are reduced by rejecting events containing any additional track with $p_T > 10$ GeV/c. To reduce background from heavy-flavor decays and jets faking leptons, events containing a jet with $E_T > 30$ GeV and events with recoil energy (see Section 6.1) $|\mathbf{u}| > 20$ GeV are rejected. The final W sample contains 4663 events, of which 3268 are in the region $65 < M_T < 100$ GeV/c^2.

[1]The beam position and the origin of the detector differ by ~0.1 cm in the r-ϕ plane.

4.3 $Z \rightarrow \mu\mu$ Sample

A sample of $Z \rightarrow \mu\mu$ events is used to check the momentum scale and to measure the momentum resolution in the high-p_T region. The sample extraction begins with 1181 events that pass a Level-3 muon trigger and have two muon candidates, each with $p_T > 18$ GeV/c. As described in Section 4.1, at least one muon is required to pass through the CMU (the "first" muon). The "second" muon is not required to pass through the muon chambers. Selection criteria are applied for the final Z sample as listed in Table 4.2. Both muons are required to have $p_T > 25$ GeV/c. The second muon is required to traverse all wire layers of the CTC so that the track resolutions of both muons are the same as the resolution of muons from W decay. To reduce cosmic rays, the same impact parameter and z-vertex matching criteria used to select the $W \rightarrow \mu\nu$ events are applied to both muon tracks. Additional cosmic rays are removed when the two muon tracks can be fit as one continuous track, consistent with being a cosmic ray. To reduce background from heavy-flavor decays and jets faking leptons, events with a (third) track of $p_T > 10$ GeV/c, with a jet of $E_T > 30$ GeV, or with $|\not{\mathbf{u}}| > 20$ GeV are rejected. The event selection yields 330 Z candidates in the invariant mass range from 76 to 106 GeV/c^2. There are no same-sign ($++$ or $--$) events in this sample.

4.4 $Z \rightarrow \mu\mu$ Mass Spectrum

To measure the Z mass and the muon momentum resolution, the mass distribution of the $Z \rightarrow \mu\mu$ data, shown in Figure 4.1, is fit to simulated lineshapes, which are generated at various values of Z mass and momentum resolution, with the Z width fixed to the world average [34]. The Z events are simulated with a leading order calculation ($p_T^Z = 0$) that includes the Drell-Yan γ and Z contributions and radiative decays, $Z \rightarrow \mu\mu\gamma$ [40, 41]. The radiative

Criterion	Events Remaining
Initial sample	1181
$\|Z_{\text{vertex}}\| < 60$ cm	1083
First muon $p_T^\mu > 25$ GeV/c	966
Second muon $p_T^\mu > 25$ GeV/c	928
Second muon traverses all CTC layers	750
$\|D_0\| < 0.2$ cm for both muon tracks	493
$\|z_{\text{vertex}} - z_{\text{track}}\| < 2$ cm for both muon tracks	415
Two muons not consistent with a cosmic ray	408
No other tracks with $p_T > 10$ GeV/c	385
No jets with $E_T > 30$ GeV	377
$\|\mathbf{u}\| < 20$ GeV	359
$76 < M_Z < 106$ GeV/c^2	330

Table 4.2: Criteria used to select the $Z \rightarrow \mu\mu$ sample.

decays shift the mass by 310 MeV/c^2. The simulated Z is given a transverse momentum selected from the $Z \rightarrow \mu\mu$ data (see Section 7).

Table 4.3 contains a list of the systematic uncertainties on the mass and resolution. The largest uncertainty, other than that from the momentum scale, is from radiative effects due to not including initial state electromagnetic radiation in the calculation. The effect of the missing diagram is evaluated by using another calculation [42], which does include initial state radiation. The uncertainty is estimated to be 40 MeV/c^2 on the Z mass. The choice of parton distribution functions contributes a negligible uncertainty. The uncertainty from the choice of the p_T^Z spectrum is shown to be negligible for variations constrained by the measured p_T^Z spectrum.

The fitted mass is

$$M_Z = 91.020 \pm 0.210(\text{stat.}) \pm 0.040(\text{syst.}) \pm 0.055(\text{scale}) \text{ GeV/c}^2. \quad (4.1)$$

This value is consistent with the value of $M_Z = 91.187 \pm 0.007$ GeV/c^2 [34]. The momentum resolution is extracted from the fit to the observed Z width,

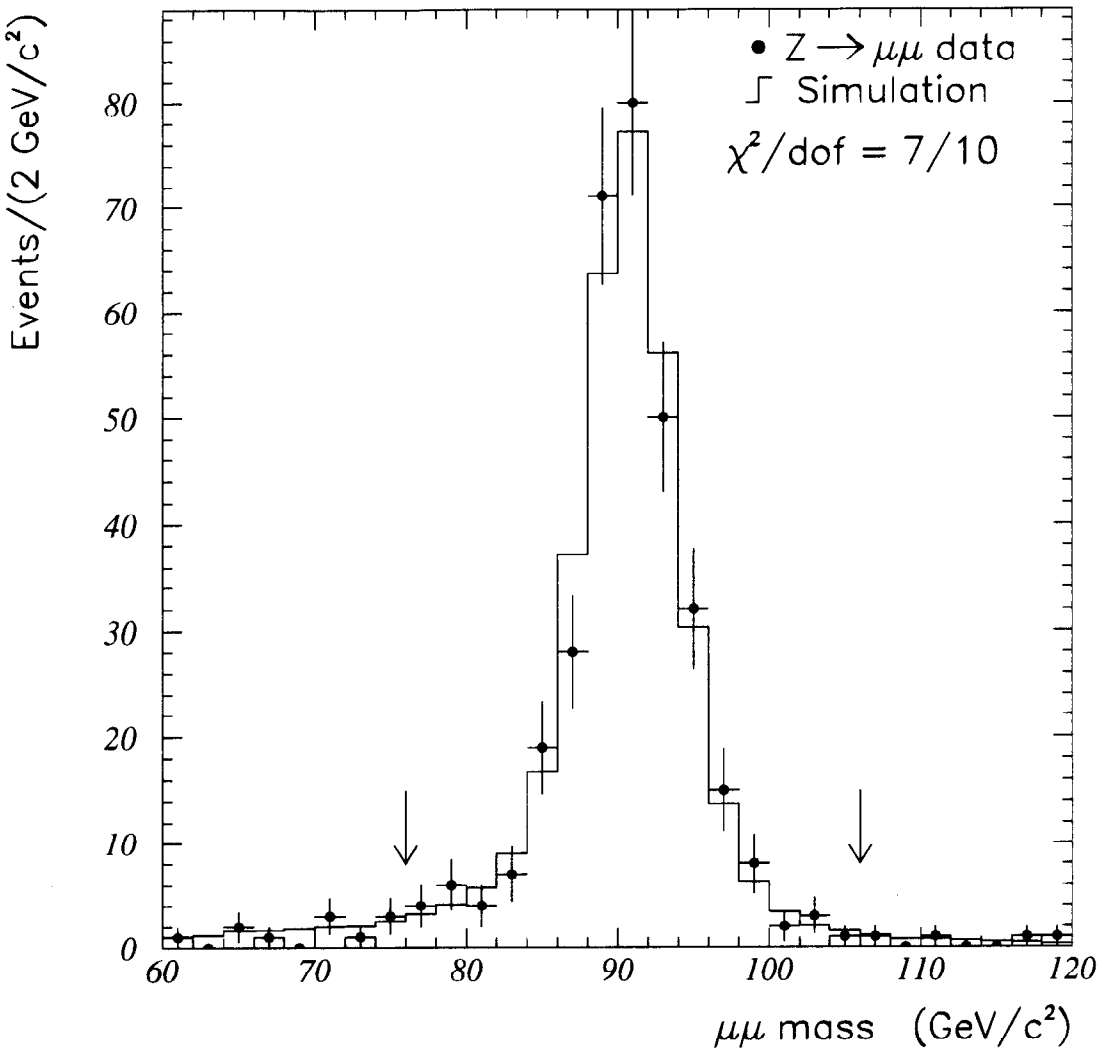

Figure 4.1: The dimuon mass spectrum near the Z mass. The arrows indicate the fit region of 76 to 106 GeV/c^2.

Effect	Uncertainty on M_Z^μ ($\mathrm{MeV/c^2}$)	Uncertainty on $\delta p_T/p_T^2$ $(\mathrm{GeV/c})^{-1}$
Statistics	210	0.000085
Momentum Scale	55	–
Radiative Corrections	40	0.000010
Fitting	10	negligible
Parton Distribution Functions	negligible	
p_T^Z spectrum	negligible	
Total	220	0.000086

Table 4.3: Summary of uncertainties in measuring the Z mass and the momentum resolution.

using $\Gamma_Z = 2.490 \pm 0.007$ GeV [34]:

$$\delta p_T/p_T^2 = 0.000810 \pm 0.000085(\mathrm{stat.}) \pm 0.000010(\mathrm{syst.})\ (\mathrm{GeV/c})^{-1}. \quad (4.2)$$

This resolution is used in the simulation of track momenta for the W mass measurement.

4.5 Summary

The track momentum resolution at high-p_T is measured to be $\delta p_T/p_T^2 = 0.00081 \pm 0.00009\ (\mathrm{GeV/c})^{-1}$. The track momentum scale in the high-p_T region is checked from the invariant mass distribution of $Z \to \mu\mu$ events. The extracted mass of the Z is $M_Z = 91.02 \pm 0.22\ \mathrm{GeV/c^2}$.

Section 5

ELECTRON MEASUREMENT

The measurement of the electron energy dominates the transverse mass measurement for the $W \rightarrow e\nu$ analysis. Section 5.1 begins with a description of the central electron reconstruction algorithm. Section 5.2 describes a calibration of the CEM which equalizes the energy response from tower to tower, reduces dependences on shower position, and corrects for time-dependences. The $W \rightarrow e\nu$ and $Z \rightarrow ee$ samples are described in Sections 5.3 and 5.4. The extraction of the energy resolution from the $Z \rightarrow ee$ data is described in Section 5.5; a check using the $W \rightarrow e\nu$ data is also described. In Section 5.6, the $W \rightarrow e\nu$ data are used to determine the energy scale using a fit to the peak of the E/p spectrum. A measurement of the CEM energy non-linearity, which affects the Z mass measurement, but not the W mass measurement, is described in Section 5.7. Finally, in Section 5.8, the measurement of the mass of the $Z \rightarrow ee$ peak is presented as a check of the energy scale.

5.1 Electron Reconstruction

The energy of a central electron is reconstructed from the sum of the energies measured in a cluster of towers in the CEM. For each tower, the geometric mean of the charge from the two phototubes, one on each side in azimuth, is used as the measure of the tower energy.[1] To construct clusters of energy, seed towers are chosen from an event as the towers with the largest transverse energy. The two towers on either side in the z direction ("shoulder towers") are included in the cluster, unless this would require crossing the boundary at $\eta = 0$, in which case the cluster consists of just two towers. Once a tower is used as a shoulder, it cannot be used as a seed. Central electromagnetic clusters whose seed tower is in the rings of towers with $1.0 < |\eta| < 1.1$ are excluded from this analysis. The energy of the electron is taken as the sum of electromagnetic energies in the cluster of seed and shoulder towers. Individual clusters continue to be identified in this way until no towers above the seed tower threshold of 5 GeV remain. For the cluster to be considered as an electron, the ratio of the hadronic energy summed over the towers in the cluster to the electromagnetic energy in the cluster must be less than 10%.

5.2 Energy Calibration, Excluding Scale

To improve the energy resolution of the CEM calorimeter, corrections are applied to account for known variations of the response due to differences among towers, dependences on shower position within a tower, and time dependences over the course of the data-taking period. These corrections are determined using inclusive central electrons with $E_T > 9$ GeV, which have their momentum and energy measured independently using the CTC and the CEM, respectively. The momentum measurement includes the beam-

[1]The geometric mean is used to reduce the dependence of the energy measurement on local shower position due to light attenuation in the scintillator.

constraint, described in Section 3.1. These electrons are predominantly produced from the decays of particles containing charm or bottom quarks. The trigger selection and electron identification are similar to those described in Reference [43]. An additional requirement that E_T+p_Tc >22 GeV is applied so that the E/p distributions are minimally biased by the hardware trigger thresholds at E_T = 8 GeV and p_T = 9 GeV/c. A sample of about 140,000 electrons is selected with the same fiducial criteria and from the same runs as the electrons in the $W \rightarrow e\nu$ sample. These data are used to remove calorimeter non-uniformities and time-dependence as described below.

Tower-by-tower calibration: An average gain for each tower is determined for the first and second halves of the data-taking period, before and after an accelerator shutdown in January 1993, during which the collision hall was open for several weeks. The responses are determined using the $100 - 200$ electrons per tower collected in each half of the data-taking period. Approximately 20 of the CEM towers without enough inclusive electrons to be calibrated are excluded from being seed towers for at least one of the halves of the data-taking period.

Response maps: The variations in response ("response maps") due to the position of the shower within the tower were measured in the testbeam in 1984-85 [20] for each of the 10 tower types in a wedge. The high statistics of the inclusive electron sample allows additional adjusting of the response maps for each tower type with 0.5% sensitivity. Figures 5.1 and 5.2 show the relative response for electrons in the final W sample, after all corrections, as a function of shower position in the azimuthal and z directions. In these figures, $x_{\rm LOCAL}$ denotes the distance of the shower from the center of a calorimeter tower in the azimuthal direction, z denotes the position of the shower along the z-axis from the center of the detector along the calorimeter, and $z_{\rm EDGE}$ denotes the distance of the shower from the nearest edge of the calorimeter

tower in the z direction. The shower position is measured at a depth of 6 X_0 in the calorimeter.

Time-dependent correction: The energy response is observed to drop by 3.5% over the data-taking period. This change is also observed in the Cesium-137 source calibrations. The variation is reduced by fitting the energy response measured with the inclusive electron data as a function of time. The correction consists of eight independent slopes, one for each of the four segments of the high-voltage distribution system, for each half of the data-taking period. Figure 5.2 shows the average energy response, after all corrections, as a function of elapsed time during the data-taking period. No obvious pattern is observed in the changes among the towers. There is a weak correlation with the segmentation of the high-voltage distribution, which is also the physical segmentation of the calorimeter. However, in spite of some (also weak) correlations with temperature effects, no conclusive explanation for the effect has yet been found.

Figure 5.3 shows the distribution of the total correction factors for the electrons in the W sample. The factors include the corrections due to individual tower response, shower position within a tower, and time. The spread of these corrections is small, 3.5%, with no electron receiving a correction larger than 15%.

The inclusive electron data is not used to set the absolute energy scale for the calorimeter because the sample contains a large background from hadrons misidentified as electrons. The sample also contains electrons from photon conversions and electrons from heavy-flavor decays. The energy flow near the electron for such processes is difficult to model. Consequently, electrons from W decay are used to determine the absolute energy scale as described in the following sections.

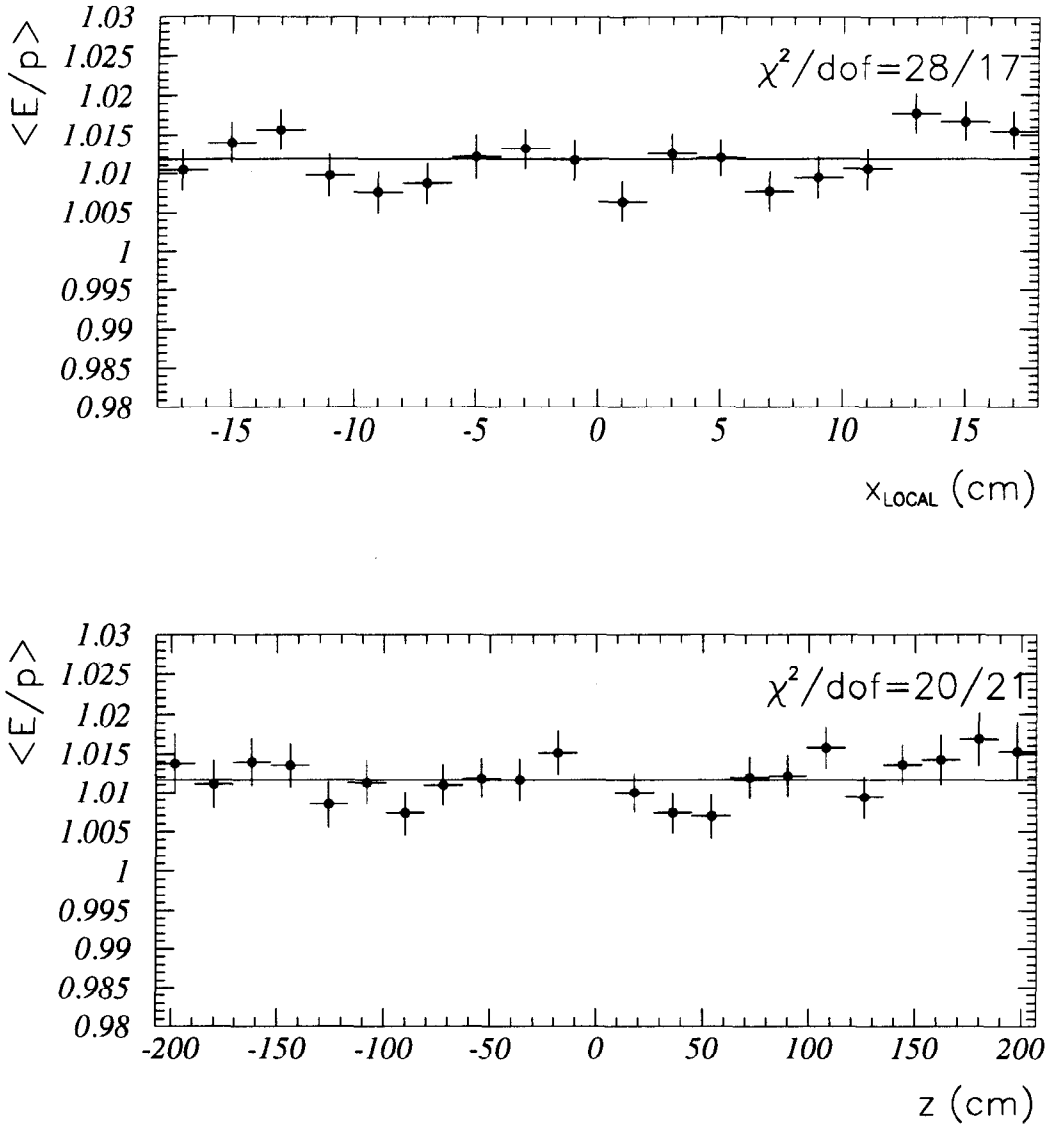

Figure 5.1: The mean of E/p in the range 0.9 to 1.1 for the electrons in the W sample after all corrections. Upper: as a function of azimuthal distance from the center of the tower. Lower: as a function of z measured from the center of the detector. For each plot the line represents the average.

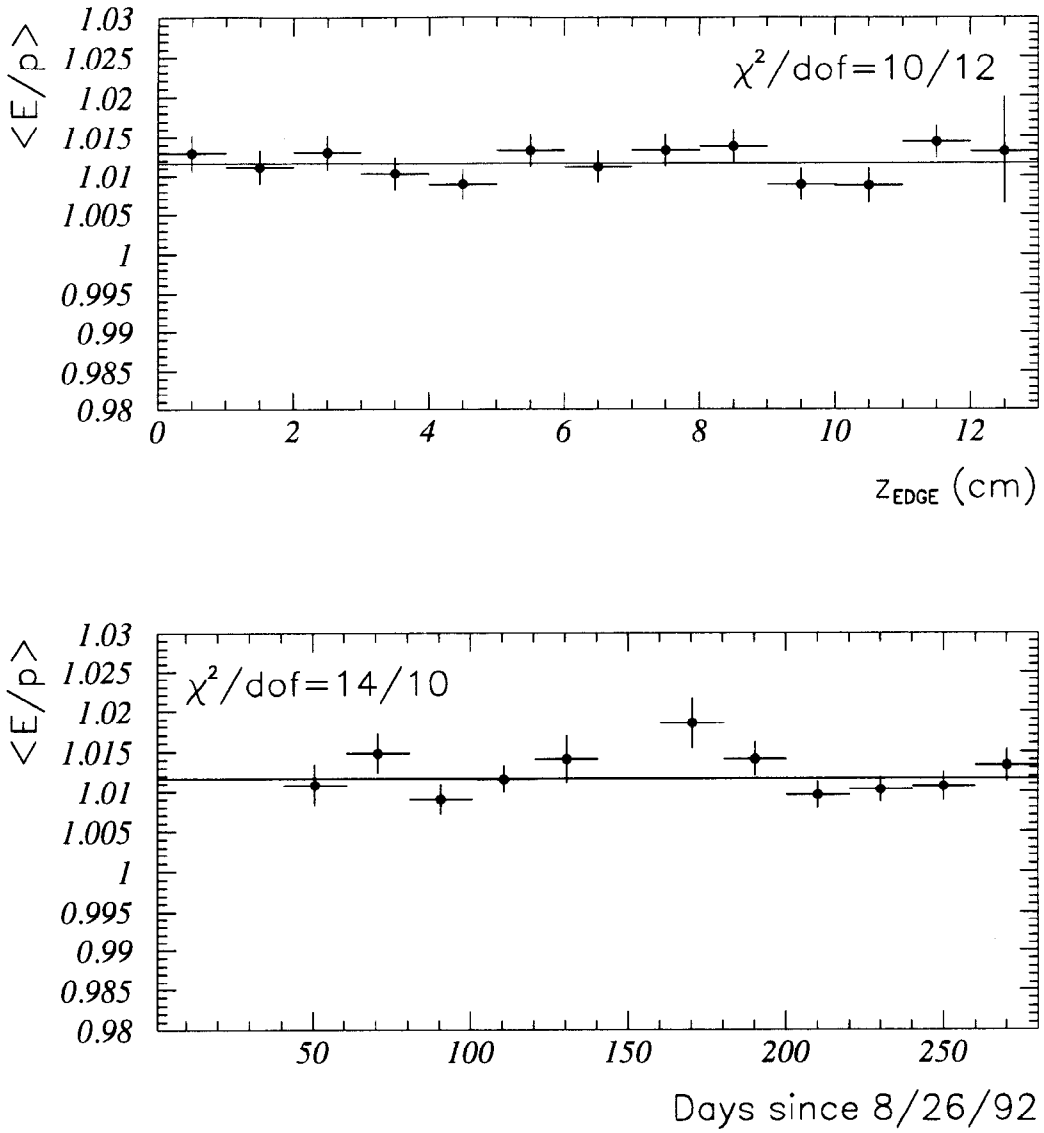

Figure 5.2: The mean of E/p in the range 0.9 to 1.1 for the electrons in the W sample after all corrections. Upper: as a function of the distance to the closest tower boundary in the z direction. Lower: as a function of the number of days since August 26, 1992. For each plot the line represents the average.

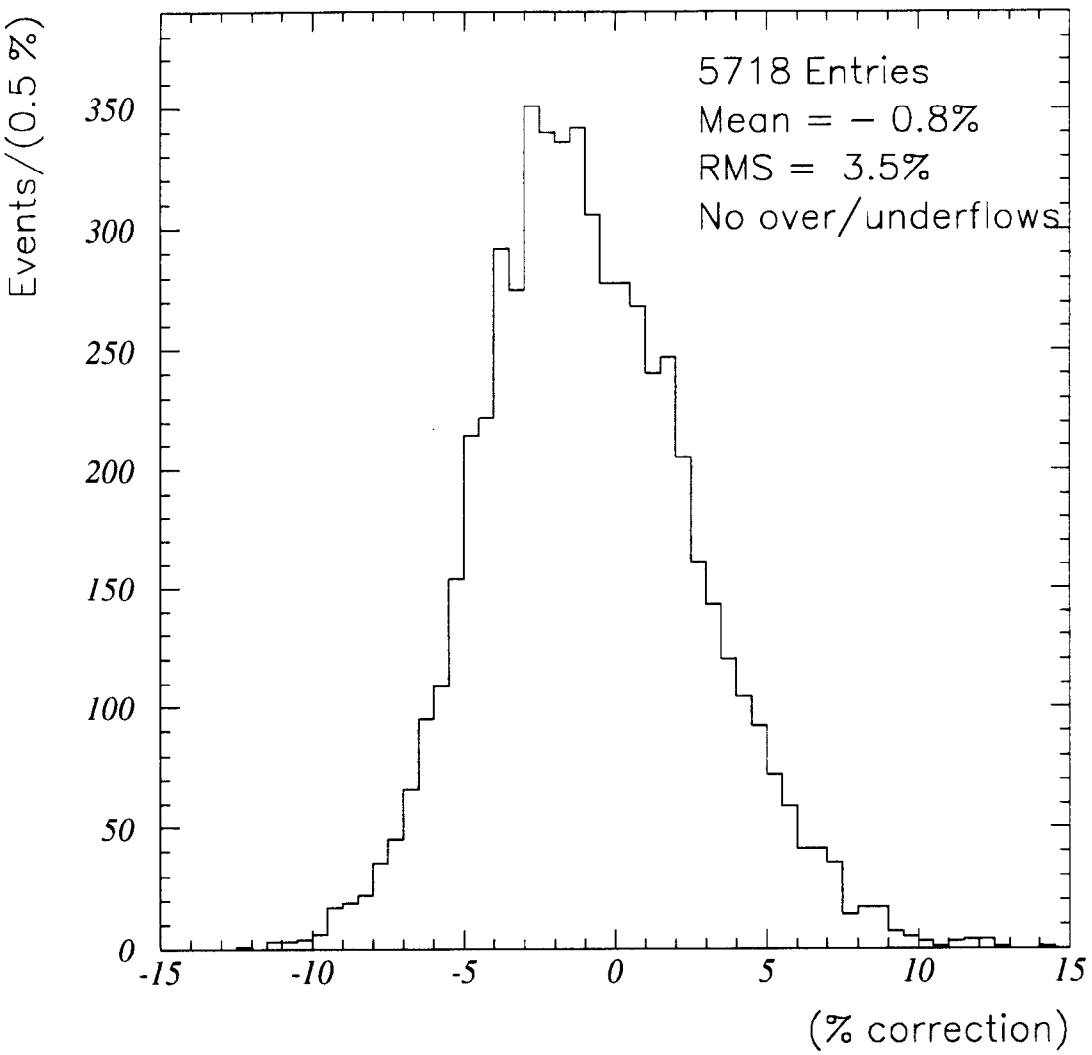

Figure 5.3: Distribution of total correction factors applied to the energies of the electrons in the $W \rightarrow e\nu$ sample.

Criterion	Events Remaining	Luminosity (pb^{-1})
Original Sample	26887	19.7
Run not immediately after a long access	24722	18.2
Exactly one electron candidate	23693	
$\|z_{\text{vertex}}\| < 60$ cm	22425	
RMS Electron track residuals < 350 μm	21815	
Electron track can be attached to a vertex	21549	
Electron track impact parameter <1.0 cm	21519	
Electron track beam constr. pull $< 3.0\sigma$	20189	
electron is fiducial	14001	
$E_T^e > 25$ GeV	13025	
$E_T^\nu > 25$ GeV	10739	
$p_T^e > 15$ GeV/c	10399	
$\|\mathbf{u}\| < 20$ GeV	9072	
No jets with $E_T > 30$ GeV	8961	
No other track with $p_T > 10$ GeV/c	8657	
Track isolation around electron	8067	
Fit region: $65 < M_T^W < 100$ GeV/c^2	5718	
Scale Fit region: $0.9 < E/p < 1.1$	4425	

Table 5.1: Criteria used to select the $W \rightarrow e\nu$ sample.

5.3 $W \rightarrow e\nu$ Sample

The event selection for the $W \rightarrow e\nu$ mass measurement is intended to produce a sample with low background and well-understood electron and neutrino kinematics. The selection begins with a 26887-event sample collected (using the online calibrations) by selecting events having $E_T^\nu > 22$ GeV and an electron with $E_T^e > 22$ GeV, $p_T^e > 13$ GeV/c, and electromagnetic energy fraction greater than 90%. The criteria applied to make the final sample are listed in Table 5.1. A line-by-line description of each of the criteria in Table 5.1 constitutes the rest of this section. Events from runs immediately after a long detector access are removed since temperature and other conditions in

the collision hall were unstable. To reduce background from $Z \rightarrow ee$ events, one and only one electron candidate may be present in the event [44]. The event vertex is chosen as the closest one reconstructed by the VTX to the origin of the electron track and must be within 60 cm in z of the origin of the detector coordinates. The RMS residuals of hits used in the fitted track must be less than 350 μm. The electron track after the beam-constraint must extrapolate to within 5 cm in z of the event vertex. The r-ϕ impact parameter of the electron track relative to the beam axis before the application of the beam constraint must be less than 1 cm. The electron position in the central detector must pass extremely tight fiducial criteria [45]. The transverse momentum of the electron track must change by less than three standard deviations when beam-constrained. The electron E_T and the neutrino E_T are each required to be greater than 25 GeV, after all calibrations, to reduce backgrounds while retaining most of the W events. The electron track p_T, after all calibrations and the beam-constraint, must be greater than 15 GeV/c. Note that the minimum transverse energy requirement presupposes knowledge of the electron energy scale so the event selection and calibration procedure requires one complete iteration. Rejecting events with jets with $E_T > 30$ GeV or events with recoil $|\mathbf{u}| > 20$ GeV reduces background. In addition, these criteria keep the events with the best resolution in transverse mass, and they yield a sample which is easier to simulate. No event with another track with p_T >10 GeV/c is allowed. A track-isolation requirement rejects events with tracks of $p_T > 1$ GeV/c within a cone of $\sqrt{(\Delta\phi)^2 + (\Delta\eta)^2} < 0.25$ around the electron track. This reduces background without excessively biasing the topology of the event. The final W sample contains 8067 events, of which 5718 are in the region $65 < M_T^W < 100$ GeV/c^2.

5.4 $Z \rightarrow ee$ Sample

The $Z \rightarrow ee$ sample serves two purposes in understanding the electron energy response. The width of the $Z \rightarrow ee$ peak measures energy resolution. The extracted Z mass serves as a check on the determination of the energy scale.

The selection of $Z \rightarrow ee$ events with one electron detected in the CEM is kept as close as possible to that of the $W \rightarrow e\nu$ event selection described above, requiring one central electron, and a second electromagnetic cluster within $|\eta| < 4.2$. The criteria used to extract the $Z \rightarrow ee$ sample from the 3366 candidates are listed in Table 5.2. Most of these criteria are described in the preceding section. If both electrons from the Z are detected in the CEM, then which electron is considered "first" is determined randomly. Otherwise, the central electron is dubbed "first." The requirement that the second-electron E_T be above 25 GeV uses an E_T that is inferred from the first electron and the underlying event, so that the Z selection closely mimics the requirement on neutrino transverse energy in the W selection. The event selection yields 543 $Z \rightarrow ee$ candidates in the range $81 < M_Z < 101$ GeV/c^2. From this sample, a subset of 259 central-central $Z \rightarrow ee$ events is used to extract the Z mass and to measure the electron energy resolution. There are no same-sign events in the 259-event central-central sample.

5.5 Energy Resolution

The width of the $Z \rightarrow ee$ peak is used to measure the electron energy resolution. The energy resolution is parameterized by

$$(\frac{\delta E}{E})^2 = (\frac{(13.5 \pm 0.7)\%\ \mathrm{GeV}^{\frac{1}{2}}}{\sqrt{E_T}})^2 + \kappa^2, \qquad (5.1)$$

where the first term is the "stochastic term" due to statistical fluctuations in energy response among electron showers, measured with an electron test-

Criterion	Events Remaining	Exposure (pb^{-1})
Original Sample	3366	19.7
Run not immediately after a long access	3114	18.2
Exactly two electron candidates (one in CEM)	2535	
$\|z_{vertex}\| < 60$ cm	2422	
First electron track residuals (RMS) < 350 μm	2379	
First electron track can be attached to a vertex	2361	
First electron track impact parameter <1.0 cm	2361	
First electron track beam constr. pull $< 3.0\sigma$	2244	
First electron fiducial (CEM)	1555	
Second electron fiducial (CEM, PEM, FEM)	1241	
First $E_T^e > 25$ GeV	1121	
Second E_T^e ("inferred") > 25 GeV	994	
First $p_T^e > 15$ GeV/c	950	
Second $p_T^e > 15$ GeV/c (if central)	947	
$\|u\| < 20$ GeV	857	
No jets with $E_T > 30$ GeV	853	
No extra track with $p_T > 10$ GeV/c	681	
Track isolation around first electron	628	
Track isolation around second electron	612	
$81 < M_Z < 101$ GeV/c^2	543	
Central-Central	259	
Central-Plug	246	
Central-Forward	38	

Table 5.2: Criteria used to select the $Z \rightarrow ee$ sample.

beam [20] [2] In the second term, κ^2 accounts for residual gain variations not corrected by the calibration procedure. For example, imperfections in the time-dependent or position-dependent calibration would be absorbed by κ.

The value of κ is extracted from the observed width of the $Z \rightarrow ee$ peak. The main contributions to this width are the intrinsic width of the Z, radiative decays ($Z \rightarrow ee\gamma$), and the smearing due to CEM energy resolution. The fractional RMS of the peak in the interval $81 < M_{ee} < 101$ GeV/c^2 is $(3.45 \pm 0.18)\%$. Lineshapes of $Z \rightarrow ee$ including the above three contributions to the width are generated using an event simulation similar to that used for the W events (described in Section 7) for different assumed constant terms. The data indicate that the best constant term to use in Equation 5.1 is

$$\kappa = (1.0 \pm 1.0)\%. \tag{5.2}$$

The lower bound is determined by the constraint that κ be positive.

A consistency check can be made by examining the width of the spectrum of the ratio of E/p for the electrons in the $W \rightarrow e\nu$ sample. The effects contributing to the width of the E/p peak are the CEM energy resolution, the CTC momentum resolution, and bremsstrahlung. The ratio of sigma to mean[3] of the E/p peak fit to a Gaussian (see Figure 5.6) over the interval $0.9 < E/p < 1.1$ is $(4.30 \pm 0.05)\%$. This ratio becomes $(4.03 \pm 0.05)\%$ when the spreading due to bremsstrahlung is removed. Using Equations 4.2 and 5.1, and the $< E_T^e >$ of these electrons (38.2 GeV), indicates that κ=$(1.1 \pm 1.1)\%$, which agrees well with the number obtained from the $Z \rightarrow ee$ data [46].

The value of κ is also consistent with expectations based on simple calculations. Since only 100-200 inclusive electrons were available to set the gain in each tower for the first and second halves of the data-taking period, and since the RMS of E/p for the inclusive electrons is 9%, κ should be at

[2]The denominator uses E_T because of the tower construction[20].

[3]This is different from the fractional RMS over a finite interval.

least 0.8%. Imperfections in the calibration procedure would make κ slightly larger.

5.6 Energy Scale Calibration

The energy scale of the CEM calorimeter is determined from a line-shape comparison of the observed E/p distribution for electrons from $W \rightarrow e\nu$ decay to a detailed Monte Carlo prediction of this distribution. The electron may lose energy to photons either as it is created from the W decay (internal bremsstrahlung) or as it passes through material (external bremsstrahlung). Since the associated photons are usually collinear with the electron, they often are included in the electron calorimeter cluster, so that the energy response is relatively unaffected by the bremsstrahlung process. In the case of either internal or external bremsstrahlung, the electron momentum, p, is typically lower than the electron energy measurement, E, producing the long tail in E/p.

The modeling of the E/p spectrum uses the same event modeling described in Section 7 and also includes the contribution from the three-body W decay matrix element for $W \rightarrow e\nu\gamma$ [40, 41]. Electrons and photons are stepped through the material from the beam line through the CTC; the processes of electron bremsstrahlung and photon conversion as described by Tsai [47] are included. The simulation propagates the electron and its associated photons to the calorimeter, and forms an electromagnetic cluster.

The simulation of the shape of the E/p distribution requires knowledge of the amount of material traversed by the electrons before their momentum is measured, since low-energy bremsstrahlung shifts the peak of E/p. The amount of material traversed by an electron travelling from its origin to the middle of the CTC is extracted from a direct accounting, created when the material was constructed or installed. The mean material traversed by

Effect	Uncertainty (on ξ)	Uncertainty ($\%X_0$)
Statistics	0.10	0.6
Backgrounds	0.03	0.2
Resolution	negligible	
Window definitions	0.10	0.6
Total Uncertainty	0.14	0.9%

Table 5.3: Uncertainties in measuring the amount of material inside the tracking volume. The scale factor, ξ, is a factor multiplying the material extracted from the direct accounting.

electrons in the W sample is predicted to be 6.4% X_0 as shown in Figure 5.4. The amount of material actually present is measured from the size of the E/p "tail" relative to the "peak", which effectively counts the number of hard bremsstrahlung events. The value of

$$\frac{\text{number of events with } 1.3 < E/p < 2.0}{\text{number of events with } 0.8 < E/p < 1.2} \tag{5.3}$$

is measured to be 470/4686. For the simulation to reproduce this tail, the accounting of the material must be increased by a scale factor, ξ, of 1.40 ± 0.14. The sources of the uncertainty on this number are summarized in Table 5.3. A statistical uncertainty of 0.10 (0.6% X_0) is due to the finite number of events in the tail. An uncertainty of 0.03 (0.2% X_0) is the limit on the effect of backgrounds in the sample, measured by adding requirements on the r-z shower profile shape and the track–shower match. The electron momentum and energy resolutions are varied and the effect on the estimate of the amount of material is negligible. An additional uncertainty of 0.10 (0.6% X_0) is taken to account for variations as the window definitions for the "peak" and "tail" are changed. This is comparable to the statistical uncertainty and is probably double counting, but is taken to be conservative. Thus, the average amount of material traversed by a W electron is $(8.9 \pm 0.9)\%$ X_0, compared to the

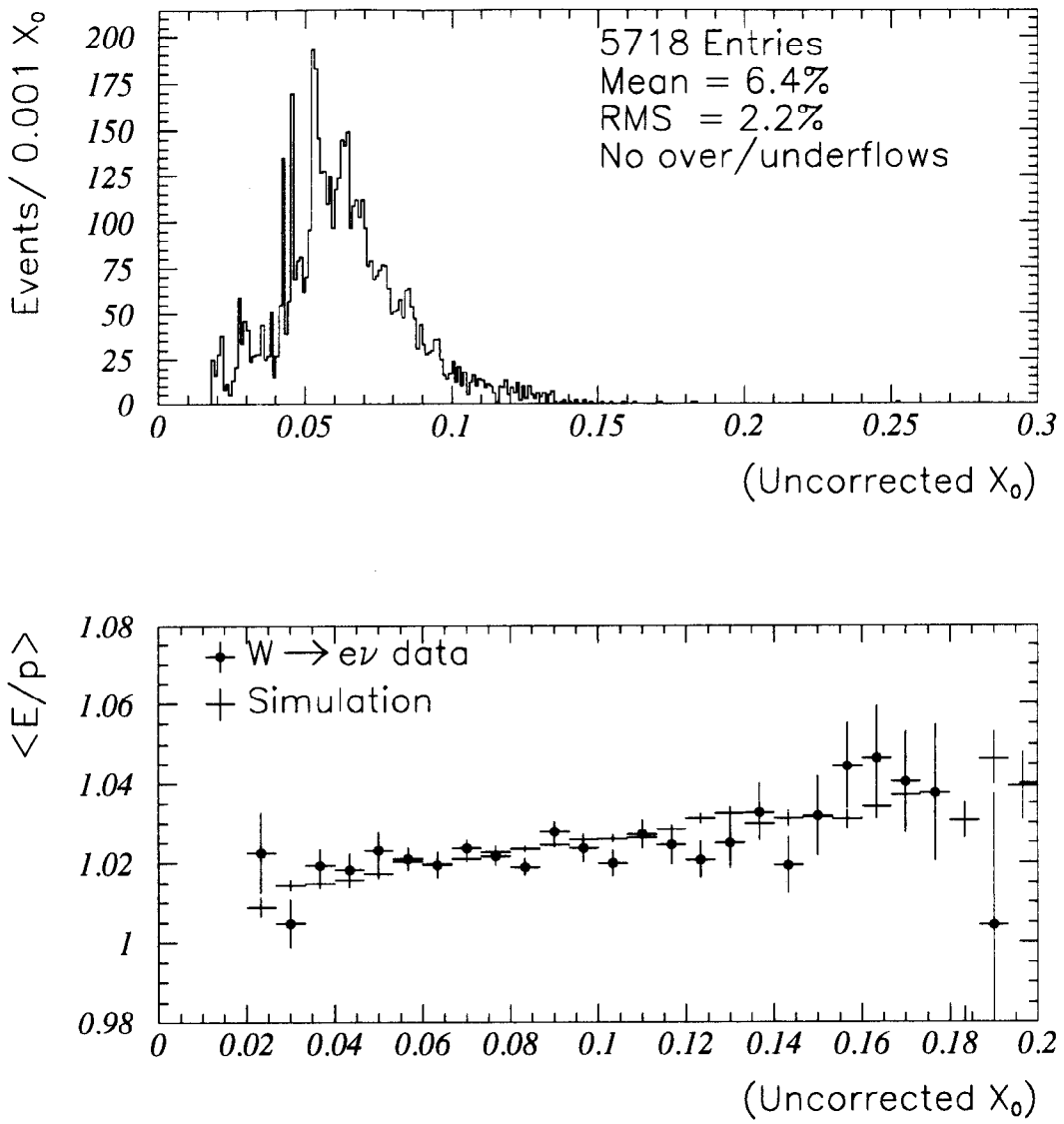

Figure 5.4: Upper: Amount of material traversed by each electron in the W sample up to the middle of the tracking volume as predicted by the direct accounting. Lower: Variation of $< E/p >$ in the data and simulation before scaling material. The mean of $< E/p >$ is taken in the interval from 0.8 to 1.2.

result from direct accounting of 6.4% X_0. This discrepancy was of concern, but subsequent studies of the amount of material using photon conversions measure $(8.1 \pm 0.4)\%$ X_0 (see Appendix A). As another check, the material is measured from the tail of the E/p distribution from the "first" electron in $Z \rightarrow ee$ events to be $(8.7 \pm 1.7)\%$ X_0, in good agreement with the value extracted from the $W \rightarrow e\nu$ data.

The value of ξ is found to be independent of the azimuthal or polar location of the electron, the event vertex position, location of shower within a tower, and time. The measured value of $< E/p >$ versus the amount of material (taken from the direct accounting) traversed by electrons in the W sample is compared to the predictions from the simulation in Figure 5.4. Note that even if the material distribution is replaced by a delta function with the same mean, the fitted energy scale and calculated amount of material change negligibly.

One may also look for anomalous behaviour of the measured amount of material for different ranges of electron E_T. A significant disagreement could indicate inadequate modeling of the electron E_T spectrum, the bremsstrahlung process, the p_T requirement, the energy dependence of the resolutions, or an energy dependence of the electron identification criteria. As shown in Table 5.4, the simulation predicts a slight rise in the number of events in the tail relative to the peak as electron E_T increases, mostly due to the p_T requirement. There is no statistically significant pattern of disagreement between data and simulation.

The simulation produces lineshapes of the E/p spectrum for a range of energy scales and momentum resolutions. The fitting procedure, applied to the region $0.9 < E/p < 1.1$, is similar to that used in the two-parameter fits described in Sections 5.1 and 9. Using the electron resolution described in Equation 5.2, the best-fit momentum resolution is

$$\delta p_T/p_T^2 = 0.000809 \pm 0.000023 \text{ (stat.)} \pm 0.000105 \text{ (syst.) } (\text{GeV/c})^{-1}, \quad (5.4)$$

Range (GeV)	tail/peak	ratio (data) (%)	ratio (simulation) (%)
$25 \leq E_T < 30$	9/88	10.2 ± 3.4	10.3 ± 0.8
$30 \leq E_T < 35$	119/1057	11.3 ± 1.0	9.8 ± 0.2
$35 \leq E_T < 40$	226/2275	9.9 ± 0.7	10.1 ± 0.2
$40 \leq E_T < 45$	99/1184	8.4 ± 0.8	10.4 ± 0.2
$45 \leq E_T < 50$	32/249	12.9 ± 2.3	11.1 ± 0.5
$50 \leq E_T < 55$	9/69	13.0 ± 4.3	12.1 ± 1.2

Table 5.4: Energy dependence of the size of the tail of the E/p spectrum relative to its peak.

which agrees well with the momentum resolution obtained from the $Z \rightarrow \mu\mu$ peak (see Equation 4.2). The sources of the systematic uncertainties on $\delta p_T/p_T^2$ are 0.000016 $(\mathrm{GeV/c})^{-1}$ from the uncertainty on ξ, 0.000085 $(\mathrm{GeV/c})^{-1}$ from the electron resolution, and 0.000061 $(\mathrm{GeV/c})^{-1}$ from doubling the size of the fit region to $0.8 < E/p < 1.2$. The fractional RMS (in the interval $0.9 < E/p < 1.1$) in the data, $(4.00 \pm 0.04)\%$, agrees well with the prediction, $(4.00^{+0.33}_{-0.16})\%$. The best fit for the E/p spectrum is shown in Figures 5.5 to 5.7.

Systematic uncertainties on the energy scale and momentum resolution arising from uncertainties in the amount of material, the electron energy resolution, and other effects are investigated by fitting artificial data with these effects modified [48]. The results of varying the amount of material are shown in Table 5.5. Using the 0.14 uncertainty on ξ, (0.9% X_0), an uncertainty on the energy scale of 0.09% is extracted from Table 5.5. A similar study for the electron resolution is summarized in Table 5.6, from which the resolution is seen to contribute a 0.06% uncertainty on the energy scale. A 0.02% shift is seen as the fit window is doubled, which is taken as an additional systematic uncertainty due to fitting. Table 5.7 summarizes the systematic uncertainties in setting the energy scale. The uncertainties at the W mass are 65 $\mathrm{MeV/c^2}$ from the finite statistics in the E/p peak, 70 $\mathrm{MeV/c^2}$ from the material mea-

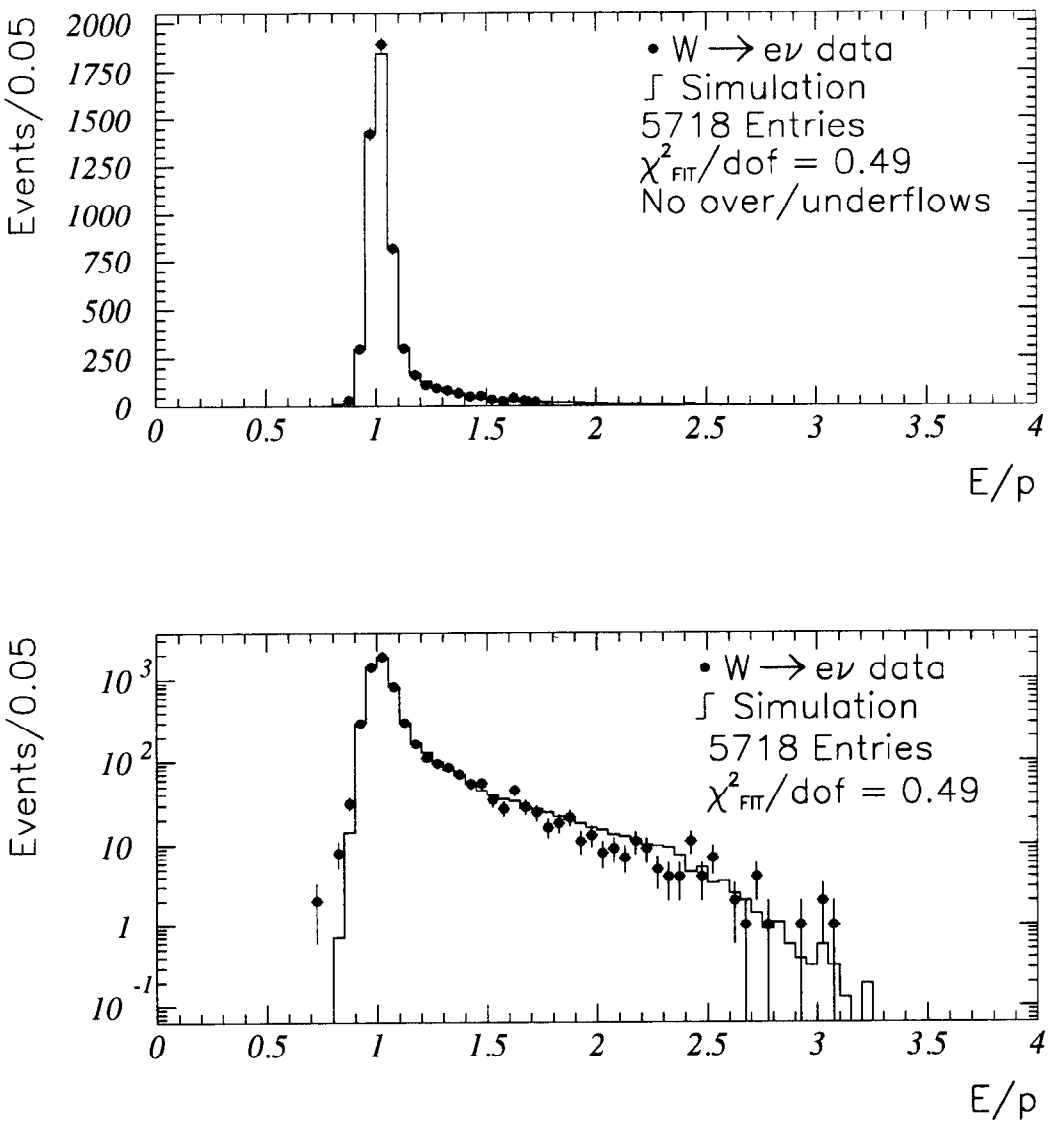

Figure 5.5: The distribution of E/p for electrons in the W sample (points) and the best-fit simulation (histogram). The value of $\chi^2_{\rm FIT}$ is for the region used by the fit, $0.9 < E/p < 1.1$. Upper: linear scale. Lower: logarithmic scale.

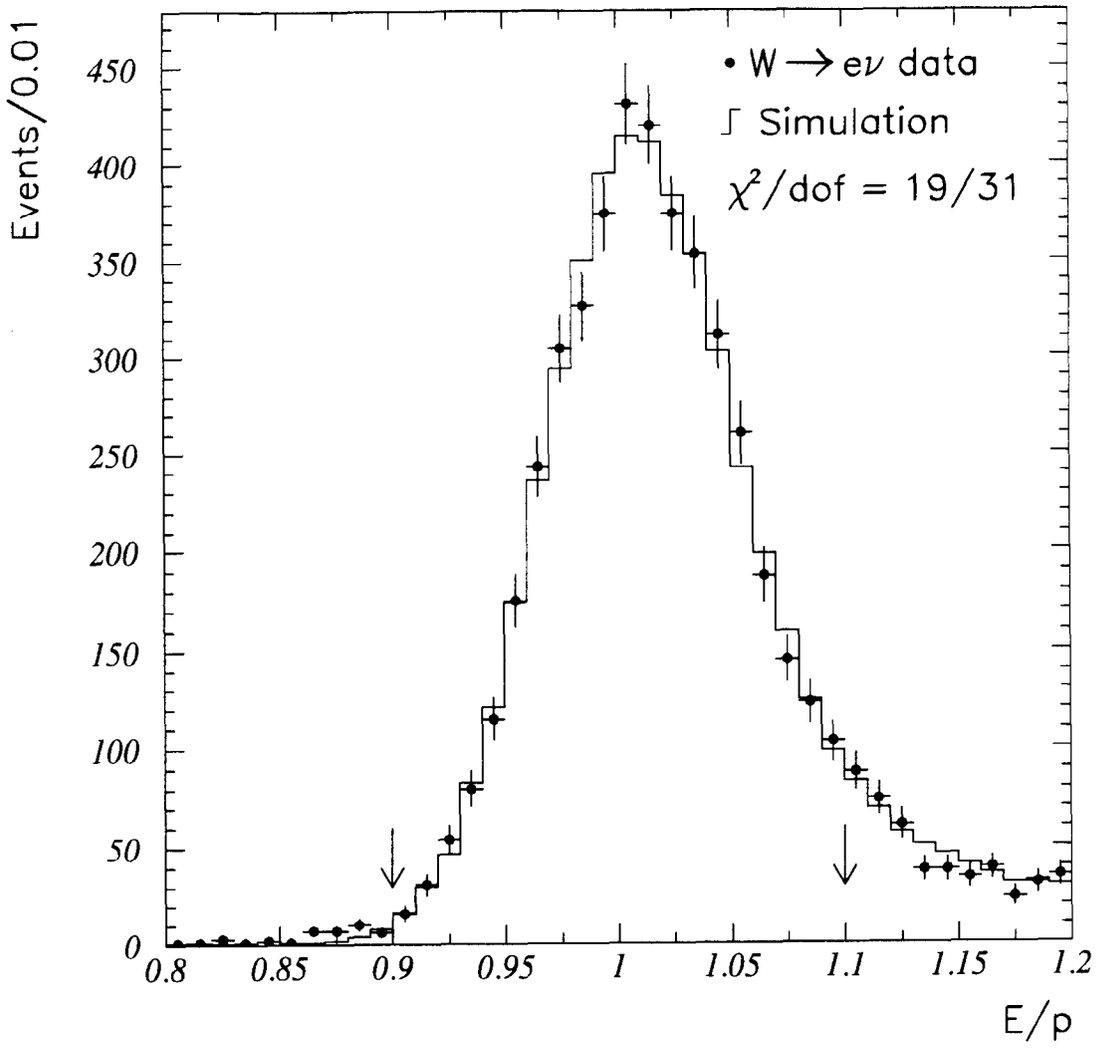

Figure 5.6: Peak of E/p for electrons in the W sample. The points are the electron data and the histogram is the best-fit simulation. The arrows delimit the fitting region. The χ^2 is calculated over the full region.

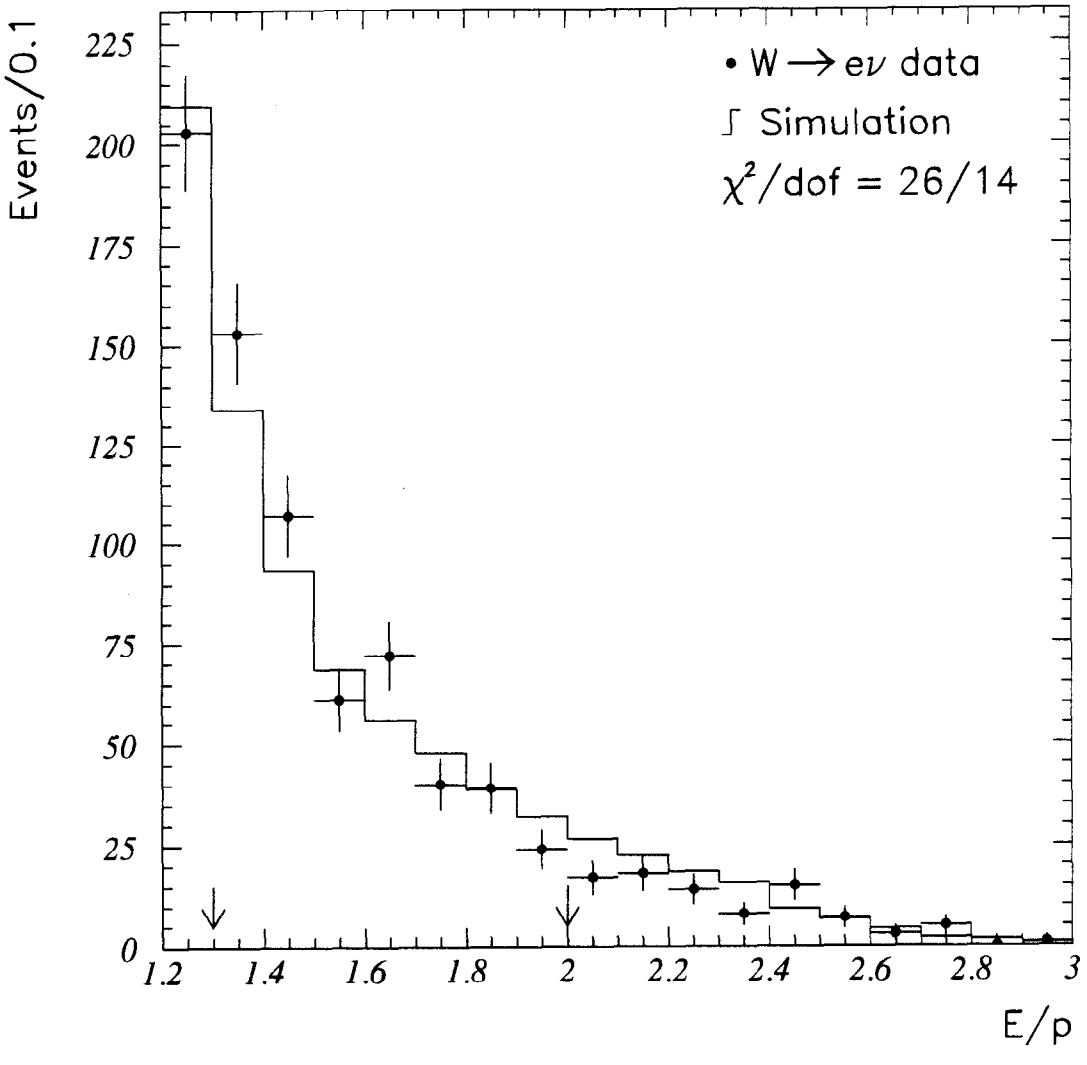

Figure 5.7: Tail of E/p for electrons in the W sample. The points are the electron data and the histogram is the best-fit simulation. The arrows delimit the fitting region. The χ^2 is calculated over the full region.

Material Scale (ξ)	Energy Scale (%)	$\delta p_T/p_T^2$ ((GeV/c)$^{-1}$)
1.00	99.72 ± 0.01	0.000764
1.20	99.87 ± 0.01	0.000783
1.40	$\equiv 100.00$	$\equiv 0.000809$
1.60	100.08 ± 0.01	0.000811
1.80	100.17 ± 0.01	0.000822

Table 5.5: Variation of the fitted energy scale and track resolution as the material scaling factor is changed from its favored value.

κ (%)	Energy Scale (%)	$\delta p_T/p_T^2$ ((GeV/c)$^{-1}$)	RMS(E/p) (%)
0.0	99.96 ± 0.01	0.000752	3.84 ± 0.01
0.5	99.94 ± 0.01	0.000761	3.80 ± 0.01
1.0	$\equiv 100.00$	$\equiv 0.000809$	4.00 ± 0.01
1.5	100.01 ± 0.01	0.000848	4.15 ± 0.01
2.0	100.04 ± 0.01	0.000904	4.33 ± 0.01

Table 5.6: Variation of the fitted energy scale and track resolution as κ (see Equation 5.2) is changed from its favored value.

Effect	Uncertainty (%)	ΔM_W^e (MeV/c^2)
Statistics in E/p peak	0.08	65
Material scale	0.09	70
Electron resolution	0.06	50
Fitting	0.02	15
Total	0.136	110

Table 5.7: Uncertainties incurred setting the energy scale from the momentum scale.

surement, 50 MeV/c^2 from the electron resolution, and 15 MeV/c^2 from the shift due to doubling the size of the fit window. The total uncertainty on the W mass from E/p, added in quadrature, is 110 MeV/c^2; combined with the uncertainty on the momentum scale the total uncertainty is 120 MeV/c^2.

5.7 Non-Linearity of Energy Response

A non-linearity in the energy response would affect the Z mass measurement, since the calibration is made with W electrons, and the electrons from Z events have larger average transverse energies. A measurement of non-linearity is only necessary for using the Z mass as a check, and is not used in the W mass measurement. Two measurements of the non-linearity are made.

One measurement of the non-linearity attempts to observe a direct gain variation with E_T. However, unlike the variation of the energy response with respect to energy-independent variables such as shower position, the variation of the response with respect to transverse energy will be biased by the resolutions. The bias arises because fluctuations in the energy correlate the E_T and E/p measurements. Because the energy response is assumed to be linear in the simulation, an E_T dependence in the difference of the residuals of the data and simulation is a measurement of the non-linearity of the energy response. Figure 5.8 shows the dependence of E/p on electron E_T both in the data and simulation, where the mean has been taken over the interval $0.9 < E/p < 1.1$. The residuals, obtained by dividing the two curves and subtracting 1.0, are also shown fit to a line. In the W calibration data, $< E_T^e >$=38.2 GeV and in the $Z \rightarrow ee$ data, $< \sqrt{E_T^{e1} E_T^{e2}} >$=42.5 GeV. The slope of the residuals in Figure 5.8 is $(0.00051 \pm 0.00022 \pm 0.00043)$ GeV^{-1}, where the first uncertainty is statistical and the second results from varying the E and p resolutions. This measurement corresponds to a correction at the Z mass of -200 ± 190 MeV/c^2, where the uncertainty is largely systematic.

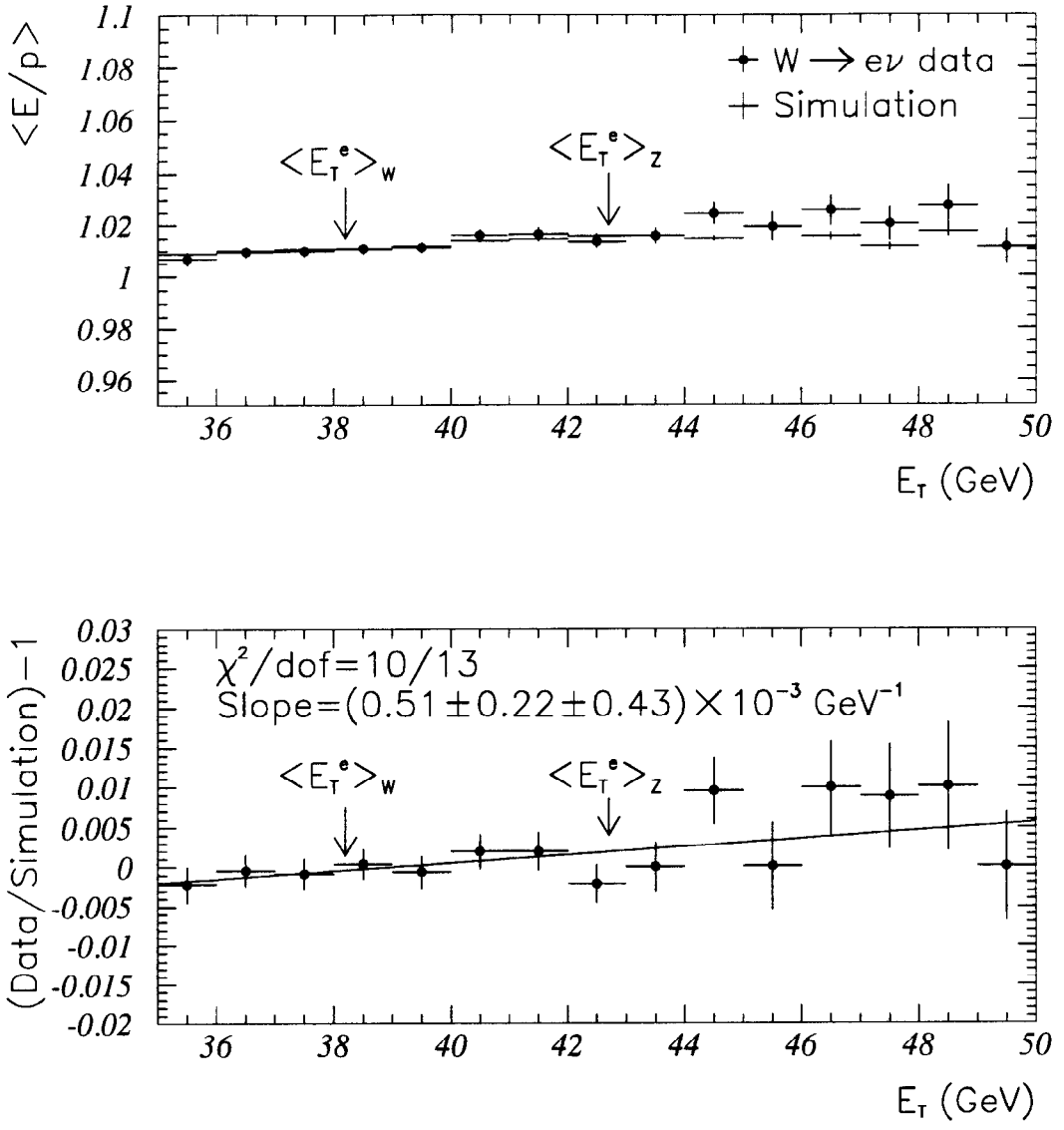

Figure 5.8: Upper: Variation of the mean of E/p with electron transverse energy in the data and the radiative simulation. Lower: The residuals of the ratios from the upper plot (data/simulation-1). The arrows indicate the mean E_T of the W and Z samples.

Another measurement of the CEM energy non-linearity is made by repeating the E/p calibration using the "first" electron from $Z \rightarrow ee$ events. The ratio of the energy scale determined from these electrons relative to that determined from W decays is 1.00051 ± 0.00243 (stat.). A systematic uncertainty on this scale determination, due to varying the E and p resolutions, is an order of magnitude smaller than the statistical uncertainty and is considered negligible. This measurement corresponds to a correction at the Z mass of $+45 \pm 230$ MeV/c^2. The uncertainty is dominated by statistical uncertainty.

The two measurements of the energy non-linearity are combined by taking a weighted average. Thus, the Z mass measured in the following section is corrected for the effect of a non-linearity by a -100 ± 145 MeV/c^2 mass shift. Since the difference between $< E_T^e >$ in the E/p fit region and the $< E_T^e >$ for the entire W mass fitting sample is 0.12 GeV, the effect of non-linearity in the energy scale on the W mass measurement is smaller than 5 MeV/c^2.

5.8 $Z \rightarrow ee$ Mass

The data are fit to lineshapes made with different Z masses. The fit range includes electron-positron pairs with invariant mass between 81 and 101 GeV/c^2. The modeling of the production and measurement of Z bosons is similar to that for W bosons described in Section 7. The Z simulation includes both the Drell-Yan [49] γ and Z amplitudes and includes the radiative decay, $Z \rightarrow ee\gamma$ [40, 41]. Including radiative decays in the simulation shifts the mass by 140 MeV/c^2.

A summary of the uncertainties in measuring the Z mass is shown in Table 5.8. A line-by-line description of the entries in this table completes this paragraph. The mass is determined with a statistical precision of 185 MeV/c^2. The choice of parton distribution functions contributes less than a 5 MeV/c^2 uncertainty to the Z mass measurement. The parameterization of the electron

Effect	ΔM_Z^{ee} (MeV/c^2)
Statistics	185
CEM constant term	< 5
Parton distribution function	< 5
Non-linearity	145
Backgrounds	10
Radiative Correction	30
Fitting	5
Scale	135
Total	270

Table 5.8: Uncertainties in determining the Z mass. Uncertainties less than 5 MeV/c^2 are considered negligible.

resolution also contributes less than a 5 MeV/c^2 uncertainty to the Z mass measurement. As described in the previous section, the fitted Z mass is corrected by -100 ± 145 MeV/c^2 to account for a possible calorimeter non-linearity in transferring the scale measured for W electrons to Z electrons. The total background rate from jets faking electrons, from electrons from heavy-flavor, and from $Z \rightarrow \tau\tau$ is estimated, in the same way as described in Section 8 for the W sample, to be less than 0.4 events. The worst-case shift in the Z mass caused by backgrounds is 10 MeV/c^2, which is taken as an uncertainty. The uncertainty due to radiative corrections is 30 MeV/c^2 (see Section 4). The finite statistics used in the lineshapes for fitting contribute a 5 MeV/c^2 uncertainty. Reducing the fit window to $86 < M^{ee} < 96$ GeV/c^2 shifts the mass by 9 ± 50 MeV/c^2, where the uncertainty reflects the statistical power of the check. The uncertainty in setting the energy scale, described in Section 5.6, corresponds to a 135 MeV/c^2 uncertainty at the Z mass.

The measured Z mass using electrons is

$$M_Z = 90.880 \pm 0.185 \text{ (stat.)} \pm 0.200 \text{ (syst.) GeV/c}^2. \qquad (5.5)$$

This is 1.1 standard deviations below the LEP value of 91.187 ± 0.007 GeV/c^2 [34]. The data and best fit are shown in Figure 5.9. The uncertainty is dominated by limited statistics and the ability to measure a non-linearity, rather than the energy scale uncertainty. These are the reasons why the $Z \rightarrow ee$ mass is not used to set the absolute energy scale.

5.9 Summary

The electron energy resolution is studied and a value of $\kappa = (1.0 \pm 1.0)\%$ is measured for the constant term in Equation 5.1. The energy scale contributes a 120 MeV/c^2 uncertainty on the W mass, of which 110 MeV/c^2 is from E/p and 50 MeV/c^2 is from the momentum scale. The measured Z mass using electrons is $M_Z = 90.88 \pm 0.27$ GeV/c^2.

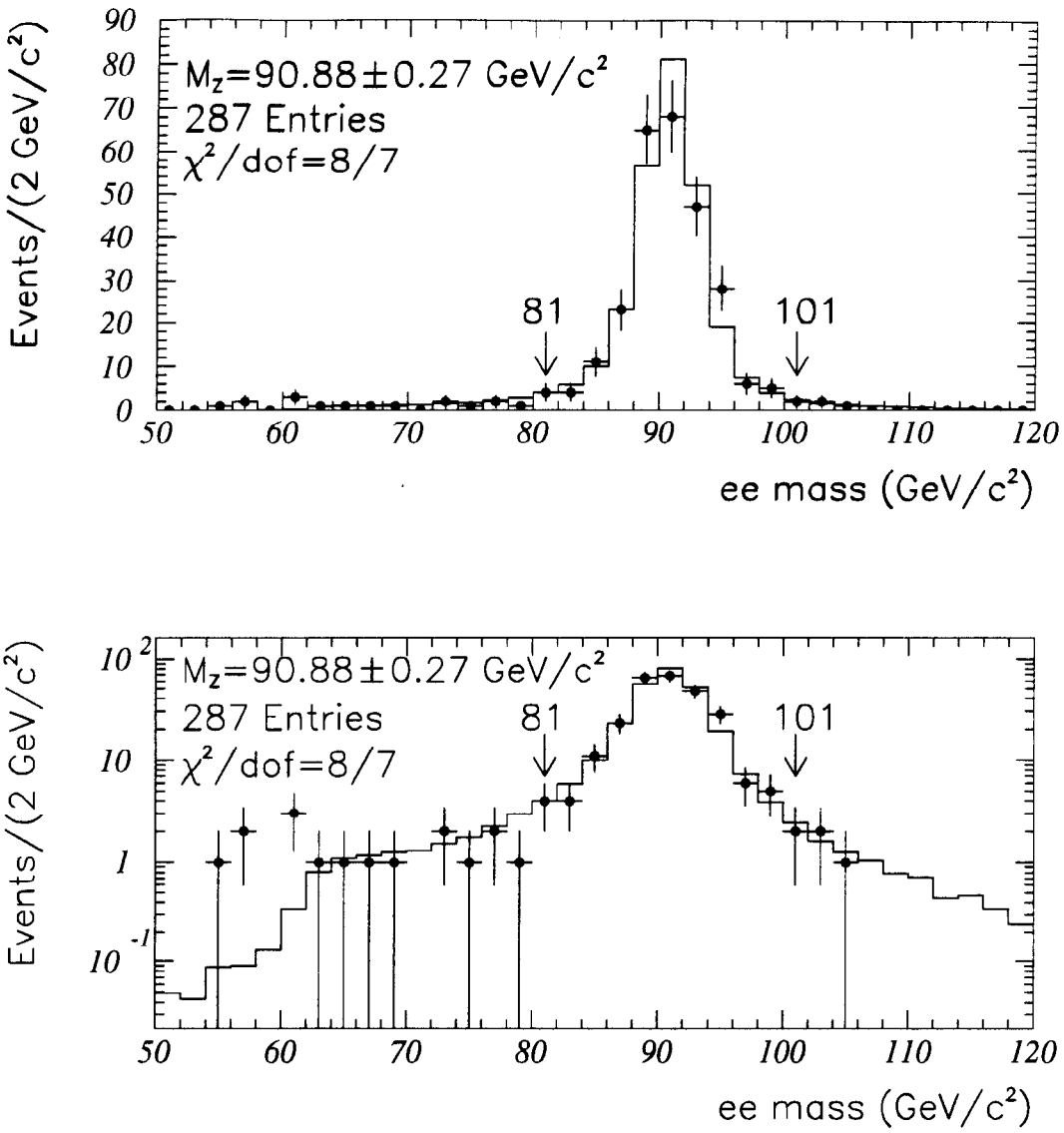

Figure 5.9: Upper: The dielectron mass spectrum around the Z peak. The points are the data shown on a linear scale. Lower: logarithmic scale. The solid line is the simulation for the best-fit mass. In the fit region, delimited by arrows, there are 259 events.

Section 6

RECOIL MEASUREMENT

The only kinematic quantities used in the W mass determination are the total transverse momentum of the recoiling hadrons and the transverse momentum of the charged lepton. This section describes the reconstruction of the recoil transverse momentum, including the corrections applied to avoid biasing the transverse mass measurement.

6.1 Recoil Reconstruction

The recoil transverse energy vector, $\mathbf{u}$, is calculated using a vector sum of energies over all calorimeter towers within $|\eta| < 3.6$,

$$\mathbf{u} = \sum_{\text{EM, HAD}} \sum_{\text{towers}} E^{\text{tower}} \, (\hat{\mathbf{n}} \cdot \hat{\mathbf{r}}) \, \hat{\mathbf{r}}, \tag{6.1}$$

where E^{tower} is the energy measured in the electromagnetic (EM) or hadronic (HAD) calorimeter tower, $\hat{\mathbf{n}}$ is the unit vector pointing in the direction of the center of the tower from the event vertex, and $\hat{\mathbf{r}}$ is the unit vector in the radial direction. Towers near the charged lepton are excluded from the sum as described in Section 6.1.1. The energy thresholds for calorimeter towers are set calorimeter-by-calorimeter (CEM, CHA, etc.) several standard devi-

ations above the noise typical of that system, and range from 100 MeV for the central detectors to 800 MeV for the forward hadronic detectors [12].[1] The electromagnetic and hadronic calorimeter compartments typically use a slightly different $\hat{\mathbf{n}}$ as the vertex position is in general not at $z = 0$.

The recoil transverse energy vector, $\mathbf{u}$, is decomposed into its components $u_\perp$ and $u_{||}$, which are perpendicular and parallel to the direction of the charged lepton, respectively. This decomposition is chosen since the measurement of $u_\perp$ is much less subject to systematic biases from bremsstrahlung, shower leakage, and charged-lepton selection than the measurement of $u_{||}$. Consequently, it is the $u_\perp$ distribution which constrains the event modeling discussed in Section 7. Effects which could lead to a $u_{||}$ bias, with corresponding effects on the W mass (see Equation 2.3), are the energy flow near the charged lepton, and energy-dependent or topology-dependent inefficiencies in the charged-lepton identification. The handling of these effects is described in the following two sections, and is summarized in Table 6.1.

6.1.1 Charged-lepton removal

The electromagnetic and hadronic energies in the towers near the charged lepton are excluded from the sum in Equation 6.1. The measurement of $\mathbf{u}$ must be corrected for this; otherwise their exclusion would produce a bias on $< u_{||} >$ and therefore on the W mass. Energy flow near the charged lepton is measured by studying the transverse energy in the towers adjacent in azimuth to the electron cluster in $W \rightarrow e\nu$ events. The observed energy is the sum of two contributions: first, the recoil, and second, leakage and bremsstrahlung from the electron [50]. Figure 6.1 shows that measuring the average energy of these towers as a function of the position of the electron shower resolves the two contributions. This figure also shows that the average

[1] Note that the threshold is in energy, and not transverse energy. The thresholds in E_T are thus smaller by a factor of sin θ.

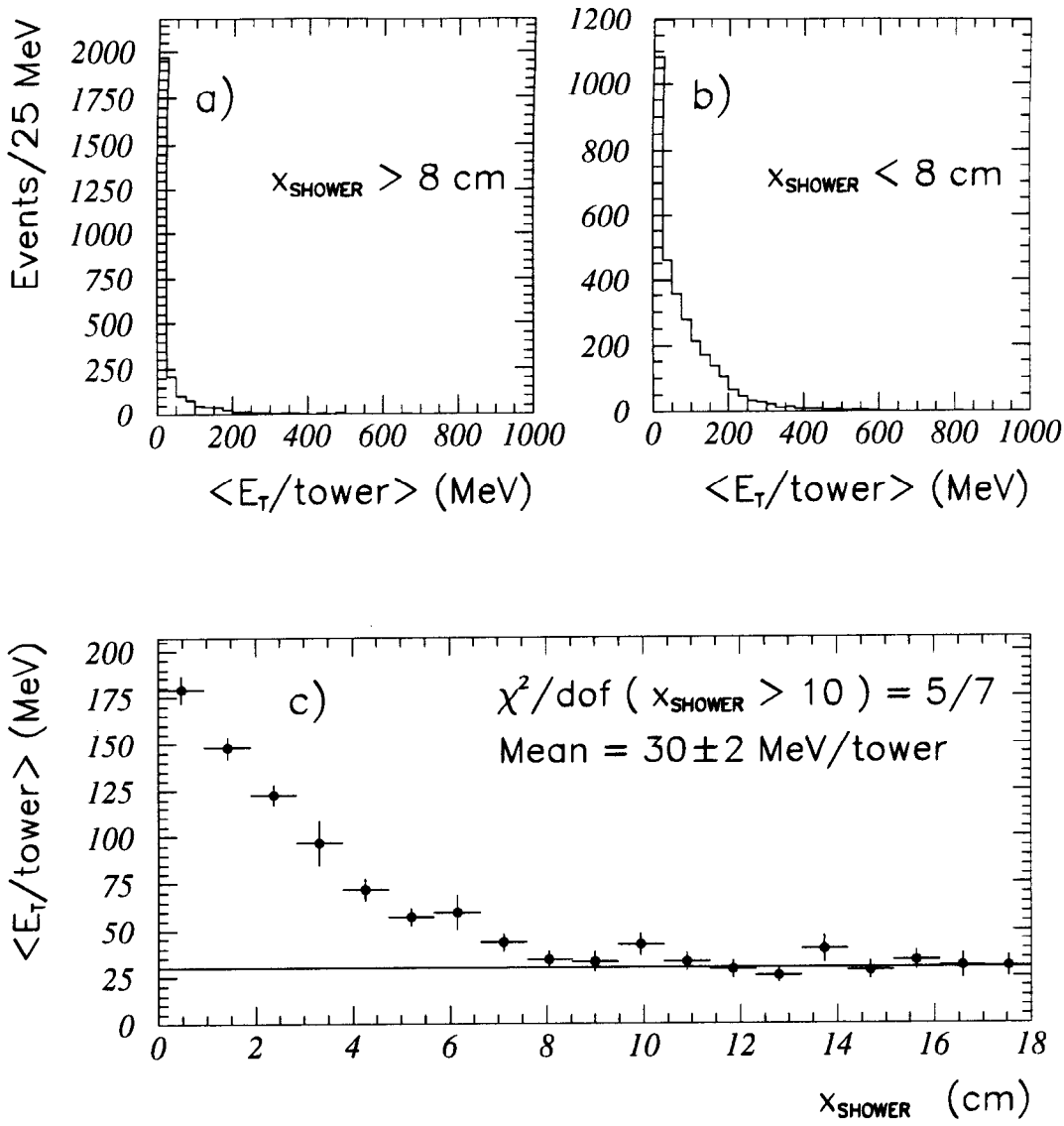

Figure 6.1: The distribution of average transverse energy per tower adjacent to the electron cluster in azimuth; *a*) $x_{\text{shower}} > 8$ cm and *b*) $x_{\text{shower}} < 8$ cm, where x_{shower} is the electron shower distance from the fiducial boundary. The fiducial boundary is 5 cm from the physical boundary of the tower. *c*) The average transverse energy in towers adjacent in azimuth to the electron cluster (neighbor towers) as a function of x_{shower}.

transverse energy per tower not related to the electron is 30 $\pm$ 2 MeV. A similar study using towers near the muon in the $W \rightarrow \mu\nu$ sample finds the same average transverse energy per tower. Thus, 30 MeV is added back into each $W \rightarrow \ell\nu$ event for every tower removed from the sum in Equation 6.1.

For the $W \rightarrow e\nu$ events, the two or three towers defining an electron cluster (see Section 5.1) are always removed from the sum in Equation 6.1. In addition, whenever the electron shower is within 8 cm of the fiducial boundary in azimuth, the towers (either two or three, depending on the number of towers in the cluster) adjacent to the electron cluster in that azimuthal direction are also removed. Since on average 4.5 towers are removed, the mean uncertainty on $< u_{\parallel} >$ is 9 MeV. From Equation 2.3 and the fact that $< M^W > \approx 1.1 \times < M_T^W >$, the resulting uncertainty on the W mass due to electron removal is found to be 10 MeV/c^2.

For the $W \rightarrow \mu\nu$ events, the towers the muon traverses are removed from the sum in Equation 6.1. The average number of towers removed is 1.5, leading to an uncertainty on the W mass of 3 MeV/c^2. This uncertainty is completely correlated with the corresponding uncertainty in the $W \rightarrow e\nu$ measurement.

For $Z \rightarrow ee$ and $Z \rightarrow \mu\mu$ events, this tower subtraction is applied to both leptons.

6.1.2 Charged-lepton identification bias

The charged-lepton identification (ID) requirements may also introduce a bias on $< u_{\parallel} >$ and the W mass. For example, if the W decays such that the charged lepton travels in the same direction as the recoil, there is greater opportunity for the recoil particles to cause the electron or muon identification to fail. These biases are investigated by tightening the charged-lepton identification requirements and measuring the subsequent shifts in $< u_{\parallel} >$ and M_W.

Effect	$\Delta < u_{\|\|} >$		ΔM_W	
	e (MeV)	μ (MeV)	e (MeV/c^2)	μ (MeV/c^2)
charged-lepton removal	9	3	10	3
charged-lepton ID	44	20	25	10
TOTAL	45	20	25	10

Table 6.1: Summary of systematic uncertainties on $< u_{||} >$ and M_W due to removing the charged lepton from the event and due to biases incurred from charged-lepton identification.

In $W \rightarrow e\nu$ events, tightening the electromagnetic fraction requirement shows that its inefficiency may cause up to a 3 MeV bias on $< u_{||} >$ and a $+20 \pm 10$ MeV/c^2 shift of the W mass [51]. Increasing the size of the track isolation cone around the electron shows that the inefficiency of the isolation requirement biases $< u_{||} >$ by -44 MeV and shifts the W mass by less than 15 MeV/c^2. In $W \rightarrow \mu\nu$ events, tightening the calorimeter energy requirement in the direction of the muon indicates that it causes a bias of -20 MeV on $< u_{||} >$ and a -10 MeV/c^2 shift on the W mass. The shifts are small and are taken only as uncertainties (See Table 6.1).

6.1.3 Comparison to simulation

The simulation described in Section 7 predicts $< u_{||} >$ for the $W \rightarrow e\nu$ sample to be -457 MeV. This agrees with the measurement of $-473 \pm 72 \pm 45$ MeV, where the first uncertainty is statistical and the second is the limit on the systematic bias estimated above (Table 6.1). The $< u_{||} >$ prediction for muons is -377 MeV compared to $-514 \pm 100 \pm 20$ MeV for the data. These results are summarized in the first lines of Tables 7.3 and 7.4.

The distributions of |u| for the electron and muon data samples are shown in Figure 6.2. The distributions of the components $u_\perp$ and $u_{||}$ are shown

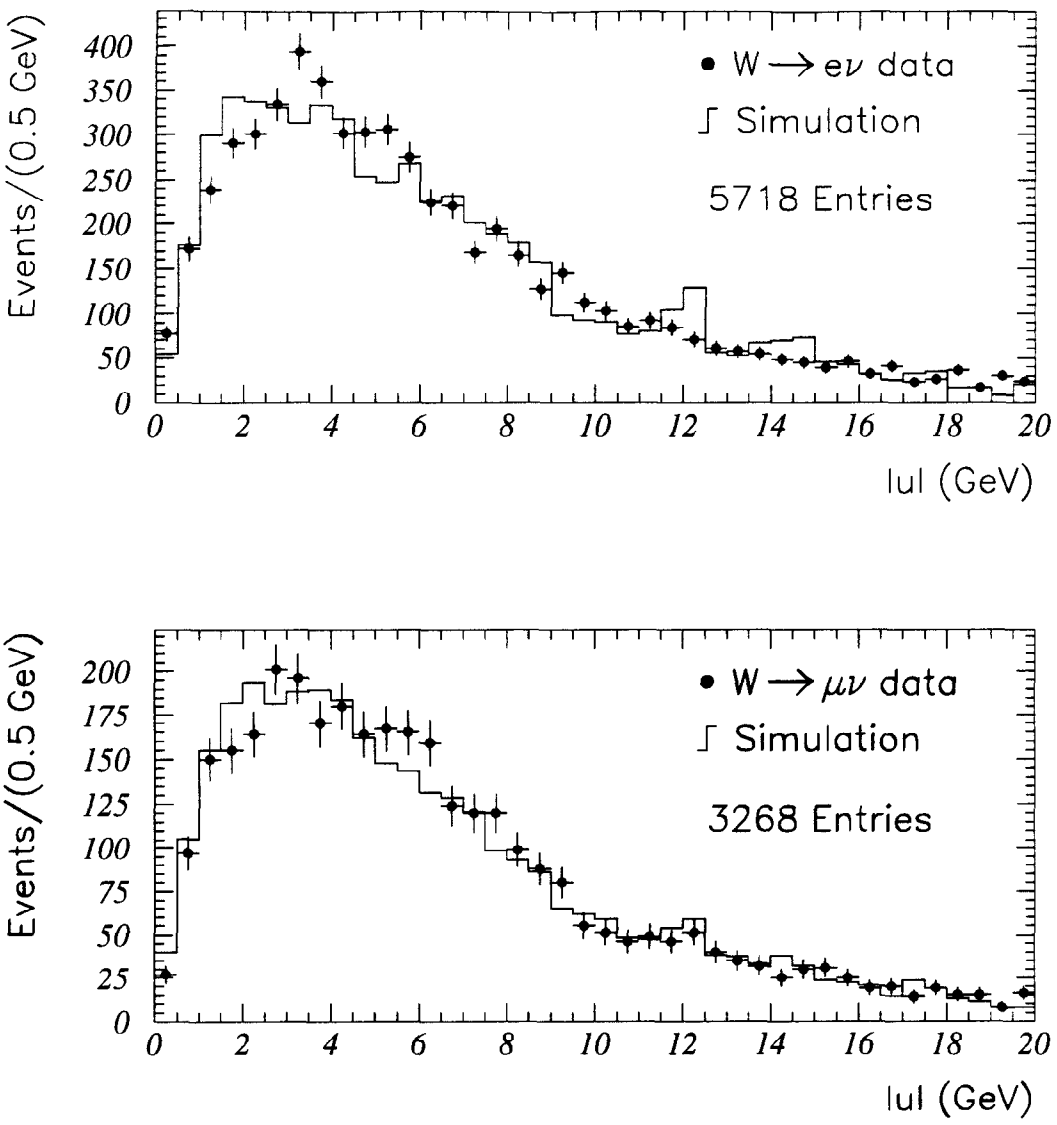

Figure 6.2: Upper: Distribution of $|\mathbf{u}|$ from the $W \rightarrow e\nu$ data (points) and simulation (histograms). The data have a mean of 6.20 ± 0.06 (stat.) GeV and RMS of 4.27 ± 0.06 (stat.) GeV, to be compared to the predictions from the simulation described in Section 7 of 6.21 GeV and 4.31 GeV, respectively. Lower: The same distributions for $W \rightarrow \mu\nu$ data. The mean and RMS of the data are 6.32 ± 0.08 GeV and 4.27 ± 0.08 GeV, compared to 6.22 GeV and 4.30 GeV from the simulation.

for the electron and muon data in Figure 6.3. The results of the simulation are superimposed.

6.2 Summary

The identification of charged leptons and their separation from the recoil energy summation affect $< u_{\parallel} >$ and thereby the W mass. The combination of these effects contributes an uncertainty on the W mass of 25 MeV/c^2 in the $W \rightarrow e\nu$ channel and 10 MeV/c^2 in the $W \rightarrow \mu\nu$ channel, of which 5 MeV/c^2, due to the lepton removal, is common.

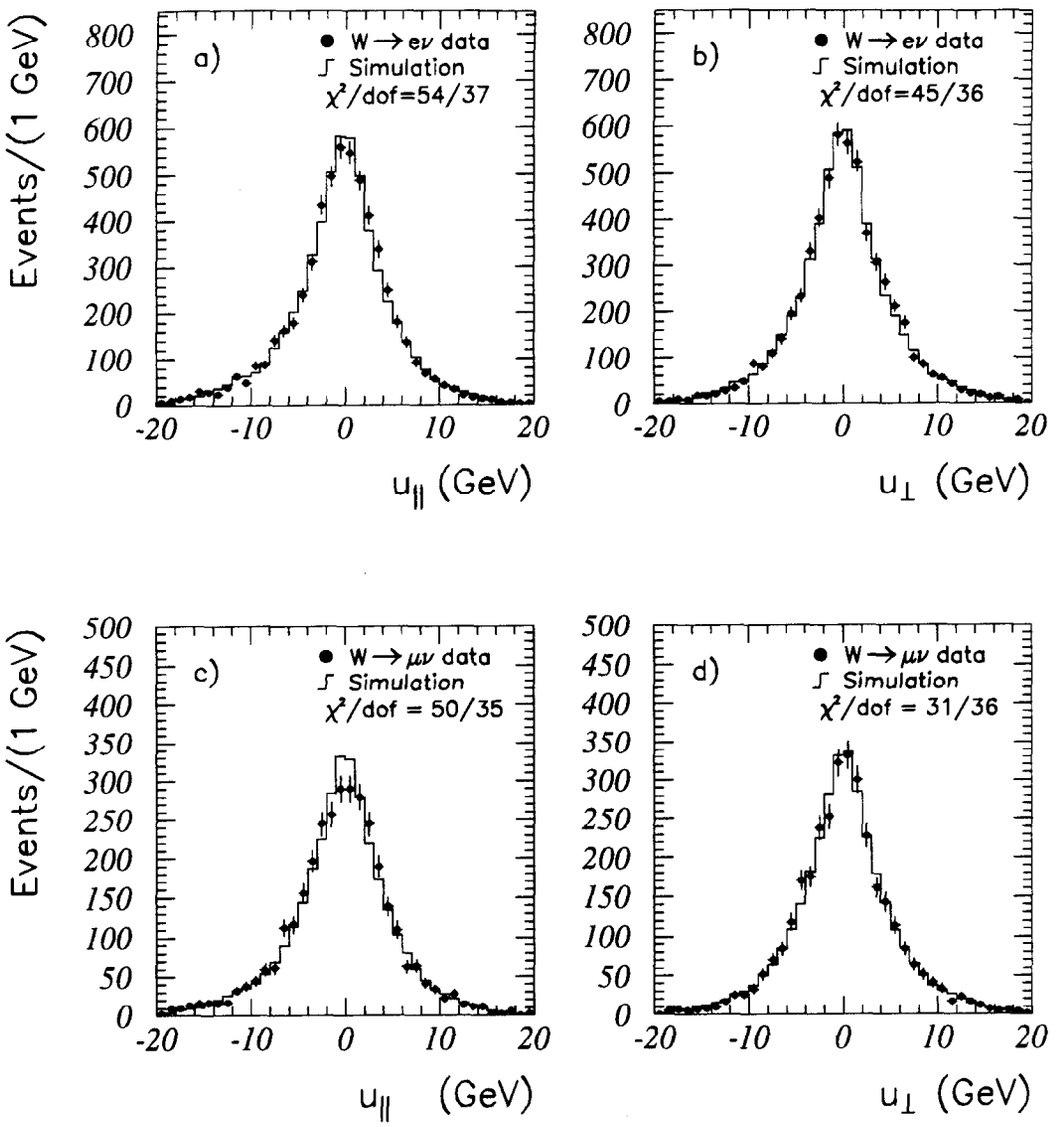

Figure 6.3: a) Distribution of $u_{\parallel}$ and b) distribution of $u_{\perp}$ for the $W \rightarrow e\nu$ channel. Also, c) distribution of $u_{\parallel}$ and d) distribution of $u_{\perp}$ for the $W \rightarrow \mu\nu$ channel. The data are represented by points and the simulation by a histogram. The mean and RMS of each distribution from data and simulation are given in the first lines of Tables 7.3 and 7.4

Section 7

EVENT MODELING

This section describes the modeling of W boson production and decay, which is implemented as a Monte Carlo event simulation. The model is compared to the data using the relevant variables for this analysis: E_T^ℓ, E_T^ν, $u_{||}$, $u_\perp$, $|\mathbf{u}|$, and M_T^W. The contributions to the systematic uncertainty on the W mass are calculated.

7.1 W Production Model

The simulation generates W events according to a Breit-Wigner distribution and a leading-order ($p_T^W = 0$) model of quark-antiquark annihilation. The distributions in momentum of the quarks are based on the MRS D'_ parton distribution functions [52]. The simulated W is Lorentz-boosted in the center-of-mass frame of the quark-antiquark pair with a transverse momentum, p_T^W. The p_T^W spectrum is derived from the $Z \rightarrow ee$ data (see Section 7.3.1), and is shown in Figure 7.1.

The $Z \rightarrow ee$ data are also used to model the detector response to W recoil [53]. The distributions in momentum of the individual recoiling particles, and the detector response to them, are difficult to model or measure

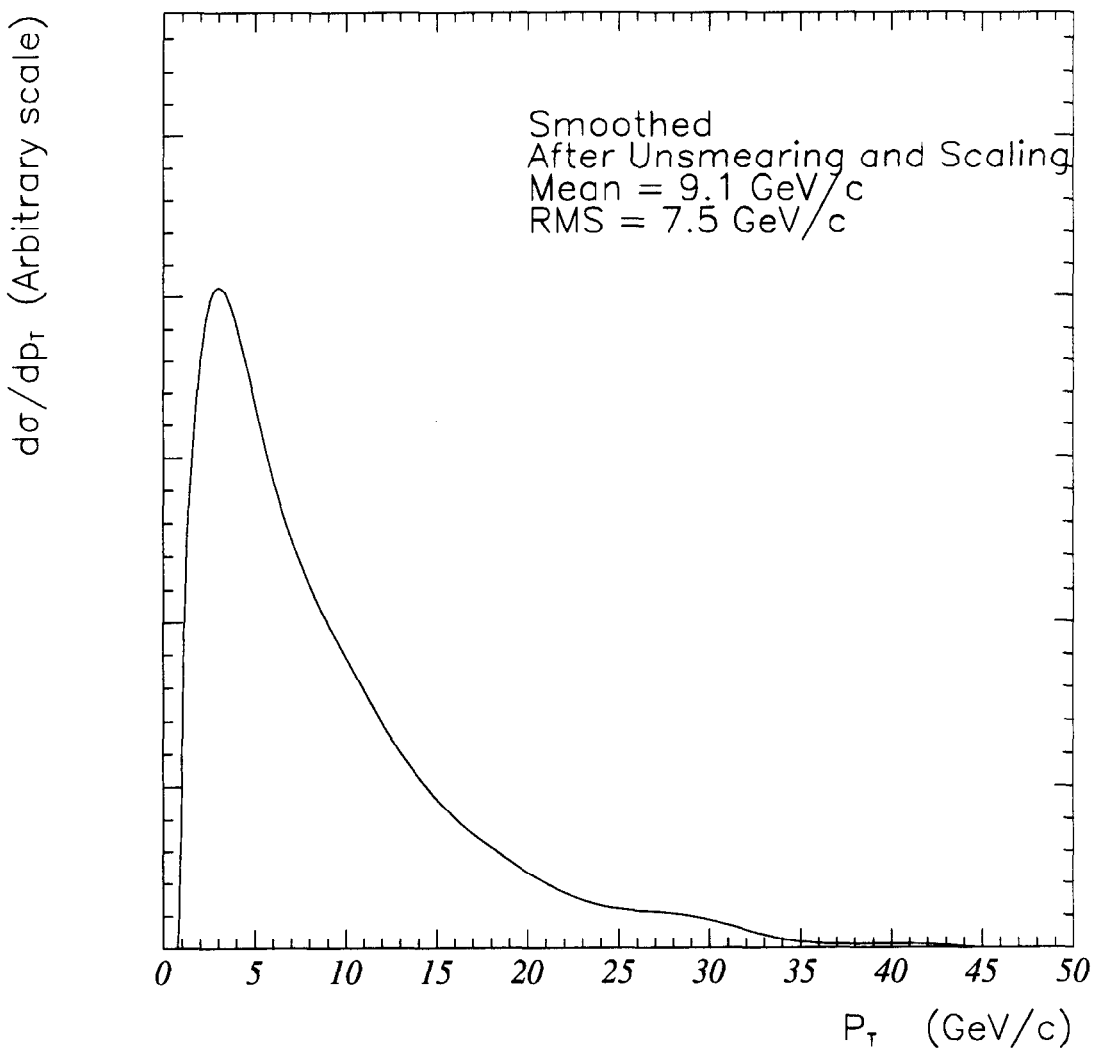

Figure 7.1: The p_T^W spectrum used in the W event simulation. The spectrum is derived from 555 $Z \rightarrow ee$ events and the "bump"near 30 GeV/c is not statistically significant.

at the requisite precision. However, Z bosons are produced at the Tevatron in the same p_T range as W bosons. Because both electrons in $Z \rightarrow ee$ events are detected and the electron energies are measured with better resolution than the recoil, the detector can be calibrated over the necessary range of recoil momenta using $Z \rightarrow ee$ decays. Specifically, when the W simulation generates a W with a particular transverse momentum, the $\mathbf{u}$ measurement from a $Z \rightarrow ee$ event with similar transverse momentum is inserted as the W recoil. The advantage of this technique is that the detector response to the recoil, taken directly from data, does not need to be modeled. Figure 7.2 shows a scatter plot of $|\mathbf{u}|$ versus p_T^Z for the $Z \rightarrow ee$ events.

It is instructive to examine the behavior of the projections of $-\mathbf{u}$ and $\mathbf{p}_\mathbf{T}^\mathbf{Z}$ along the axis defined by the angular bisector of the two electron directions, the "η-axis" (see inset to Figure 7.3). A scatter plot of these projections, u_η versus p_η (see Figure 7.3), has two advantages over Figure 7.2. First, the low-p_T recoil response is no longer obscured. Second, this projection of $\mathbf{p}_\mathbf{T}^\mathbf{Z}$ is the least subject to measurement error due to electron energy resolution. Using the latter feature and the observation that the two of the three farthest outliers in Figure 7.2 (see caption) are also the farthest outliers in Figure 7.3, suggests that it is the recoil measurement, not the charged-lepton energy measurement which is causing the deviation. In support of this interpretation, these three events all lie in the tail of the z-vertex distribution where the recoil measurement is expected to worsen because there are larger cracks into which hadrons can escape undetected. These events illustrate how the method of inserting the measured recoil from $Z \rightarrow ee$ events reproduces rare deviations from a simple parametrization.

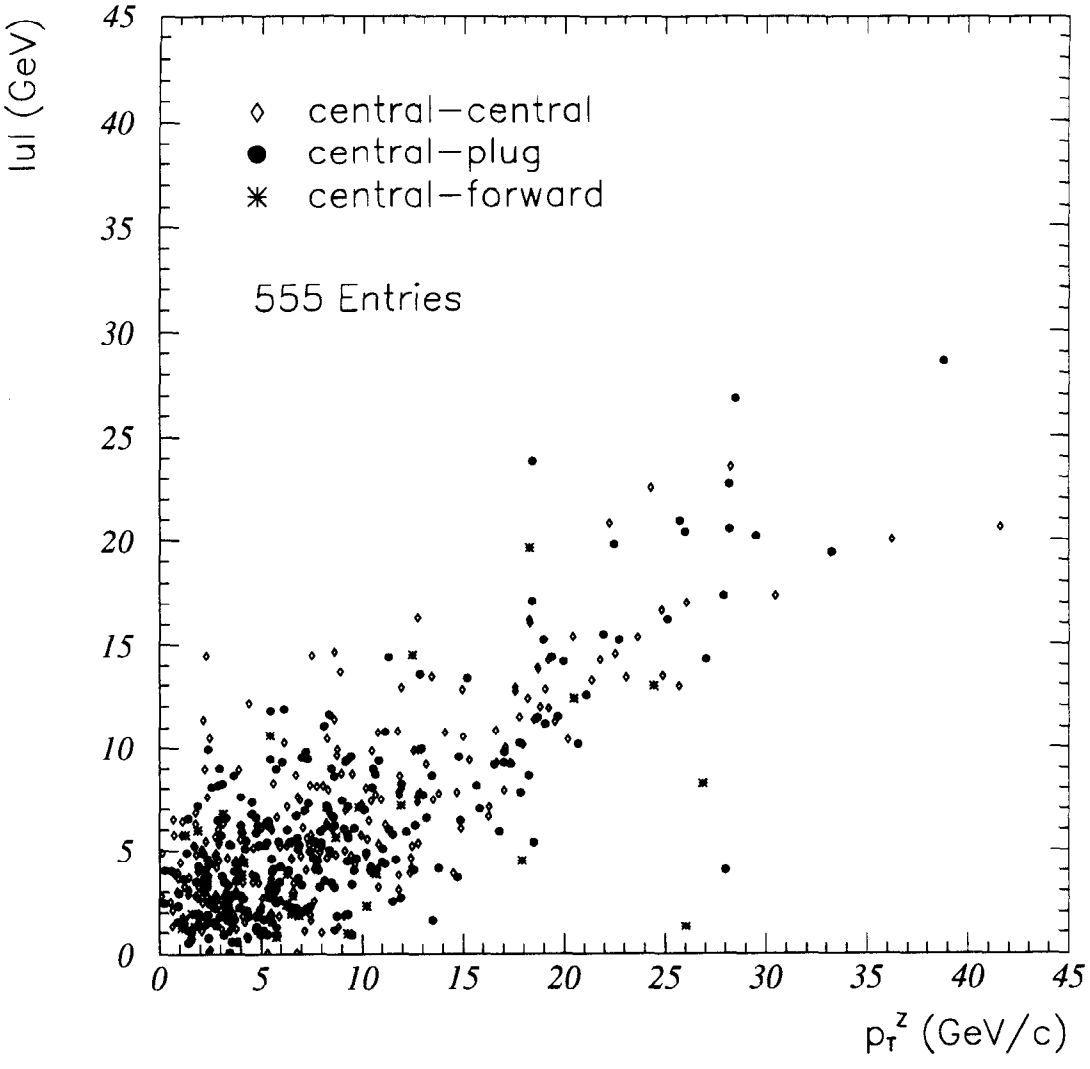

Figure 7.2: Scatter of $|\mathbf{u}|$ versus p_T for the $Z \rightarrow ee$ events. There are 555 events, rather than the 543 events listed in Table 5.2, since the $|\mathbf{u}| < 20$ GeV requirement has been removed. The "outliers" referred to in the text are the three events with $p_T > 25$ GeV/c and $|\mathbf{u}| < 10$ GeV.

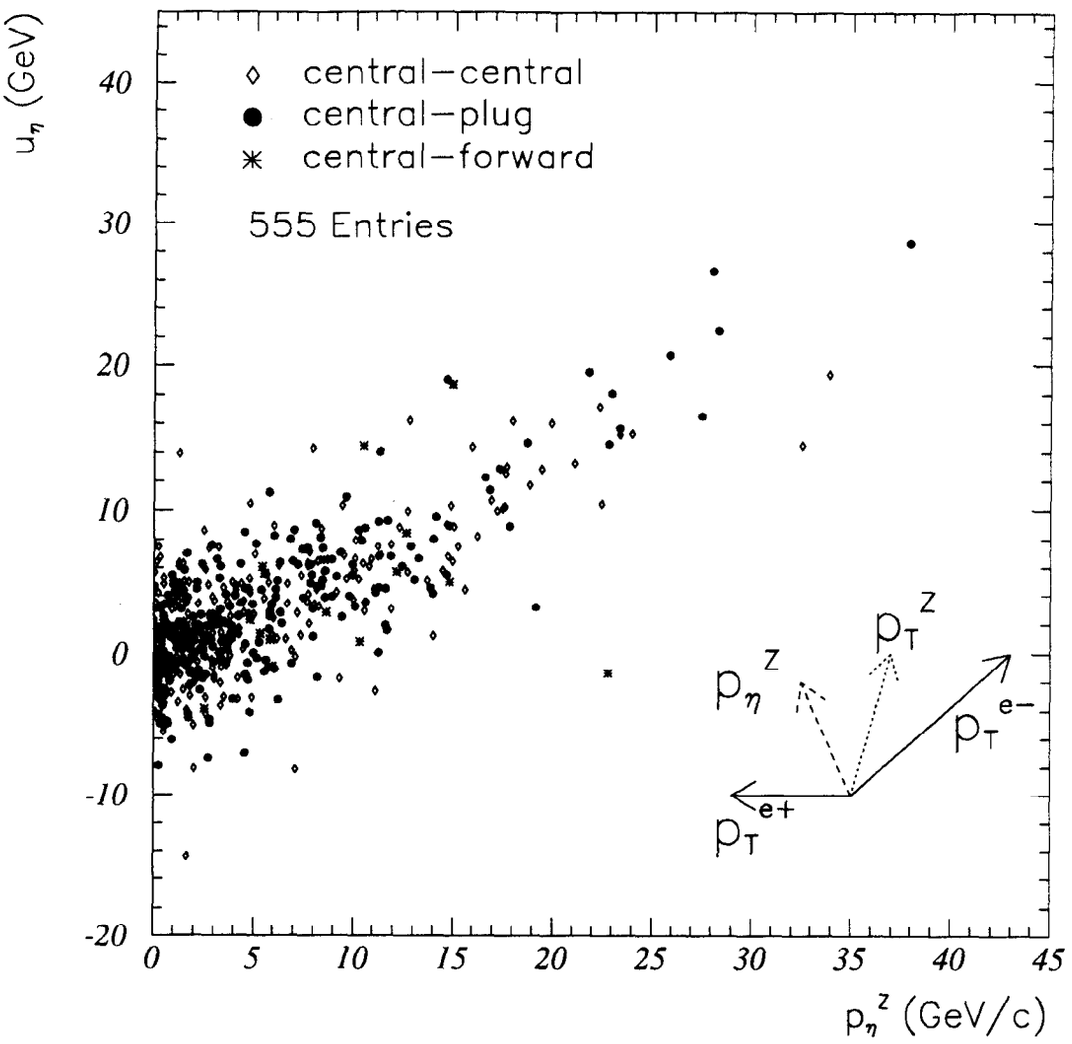

Figure 7.3: Scatter of u_η versus p_η for the $Z \rightarrow ee$ events. There are 555 events, rather than the 543 events listed in Table 5.2, since the $|\mathbf{u}| < 20$ GeV requirement has been removed. The "outliers" referred to in the text are the two events with $p_\eta > 17$ GeV/c and $u_\eta < 5$ GeV.

7.2 W Decay Model

In the simulation, the W bosons are treated as spin-one particles with a momentum and polarization determined by the leading-order production model described above. The W boson decays via the weak interaction into a neutrino and charged lepton (electron, muon or tau). Events with a tau that does not decay into an electron or muon are rejected [54]. The electron or muon from the W decay is propagated through a model of the CDF geometry to determine if it strikes a fiducial region. If so, its measured momentum or energy is determined according to the parameterization of the resolution in Equation 4.2 or 5.1. Using this simulated charged lepton measurement and the simulated recoil measurement described in the preceding section, the transverse mass and other properties of the event are reconstructed.

7.3 Constraints and Performance of Model

This section describes the evaluation of systematic uncertainties on the W mass and the W width due to modeling. Data showing the performance of the model are given.

7.3.1 p_T^W spectrum

To model the shape of the transverse mass and other spectra in W events, a p_T^W spectrum must be used in the event simulation. However, the low-p_T part of the transverse momentum spectrum of W events, from which most of the events used in this measurement are drawn, is not known with sufficient precision to use in the W transverse mass measurement. A direct measurement of the p_T^W spectrum [55] has systematic uncertainties greater than 300% in the pertinent region. Theoretical calculations of the shape of the spectrum in this p_T^W region are also subject to large uncertainties [56, 57].

r	RMS($u_{\parallel}$) (GeV)	RMS($u_{\perp}$) (GeV)	ΔM_W^e (MeV/c^2)	$\Delta\Gamma_W^e$ (MeV)
1.072	5.25	5.15	-29 ± 14	-86 ± 26
1.092	5.35	5.24	-16 ± 14	-53 ± 27
1.112	5.38	$\equiv 5.28$	$\equiv 0$	$\equiv 0$
1.132	5.52	5.40	$+35 \pm 14$	$+73 \pm 24$
1.152	5.60	5.47	$+81 \pm 14$	$+229 \pm 23$

Table 7.1: Variation of the RMS of $u_{\parallel}$ and $u_{\perp}$ and systematic mass and width shifts with the p_T^W scale factor, r, in the $W \rightarrow e\nu$ simulation. The mass shift is for the fixed-width fit. The width shift is for a simultaneous fit to both the mass and width.

Rather than using a previous p_T^W measurement or a theoretical calculation, this W mass analysis uses the similarity of the p_T spectra of W and Z bosons observed in direct measurements [55, 58] and in theoretical predictions [59] as a starting point. Specifically, an initial guess at the proper p_T^W spectrum is taken as the observed $Z \rightarrow ee$ p_T spectrum [53], corrected for distortions due to electron energy resolutions.

This initial p_T^W spectrum is tuned by scaling the transverse momenta by a scale factor, r, *i.e.*,

$$p_T^W(\textit{scaled}) = r \times p_T^W, \tag{7.1}$$

until the RMS of the $u_{\perp}$ distribution from the simulation agrees with that from the data. Table 7.1 shows how the widths of the $u_{\parallel}$ and $u_{\perp}$ distributions predicted by the $W \rightarrow e\nu$ simulation change as the W transverse momenta are scaled by r. Table 7.2 shows the same information for the $W \rightarrow \mu\nu$ simulation. The value and uncertainty of the RMS of $u_{\perp}$ determine r to be 1.112 ± 0.018 for electrons, and 1.110 ± 0.030 for muons [60]. The uncertainty on r produces an uncertainty on the W mass of 35 MeV/c^2 for both the electron and the muon analyses. The corresponding uncertainty on the W width measurement (see Section 9.1) is 95 MeV for both the electron and muon measurements.

r	RMS($u_{\parallel}$) (GeV)	RMS($u_{\perp}$) (GeV)	ΔM_W^{μ} (MeV/c^2)	$\Delta\Gamma_W^{\mu}$ (MeV)
1.050	5.19	5.11	-50 ± 23	-114 ± 43
1.080	5.27	5.23	-14 ± 23	-66 ± 43
1.110	5.38	$\equiv 5.30$	$\equiv 0$	$\equiv 0$
1.140	5.57	5.47	$+38 \pm 23$	$+75 \pm 43$
1.170	5.65	5.55	$+90 \pm 23$	$+226 \pm 43$

Table 7.2: Variation of the RMS of $u_{\parallel}$ and $u_{\perp}$ and systematic mass and width shifts with the p_T^W scale factor, r, in the $W \rightarrow \mu\nu$ simulation. The mass shift is for the fixed-width fit. The width shift is for a simultaneous fit to both the mass and width.

Sensitivity of the W mass measurement to a change in shape of the p_T^W distribution beyond a scale change is investigated using the $W \rightarrow e\nu$ data and simulation. The shape of the p_T^W spectrum used in the simulation is skewed with its mean (9.1 GeV/c) held constant using

$$p_T^W(\textit{distorted}) = 9.1 \text{ GeV/c} + s \times (p_T^W - 9.1 \text{ GeV/c}), \tag{7.2}$$

where s is the skew parameter. An alternate distortion of the p_T^W spectrum is investigated by changing the shape of the p_T^W spectrum according to:

$$p_T^W(\textit{distorted}) = r \times (p_T^W + t \times (p_T^W)^2), \tag{7.3}$$

where t parameterizes this distortion and r is chosen so that the RMS of the $u_{\perp}$ distribution agrees with the data; the bounds on s and t are determined from the data. The data are consistent with the p_T^W spectrum used in the simulation needing no skew. The effects due to these distortions are constrained by the data to be less than 25 MeV/c^2 on the W mass and 40 MeV/c^2 on the W width. These uncertainties are common to the electron and muon channels.

7.3.2 Recoil modeling

Uncertainties in the recoil modeling are incurred from using the $Z \rightarrow ee$ events to calibrate the detector response to the W recoil. Two effects are investigated: statistical fluctuations arising from the finite size of the Z sample and the effect of electron energy resolution on the p_T^Z measurement. Data showing the performance of the model are given.

The effect of statistical fluctuations in the Z sample is measured by generating artificial $W \rightarrow e\nu$ data samples which use fewer $Z \rightarrow ee$ recoil calibration events. Fitting these artificial data to the lineshapes in Section 9 shows that the finite number of Z events leads to a 50 MeV/c^2 uncertainty on the W mass and a 170 MeV uncertainty on the W width. These are common to the electron and muon channels. The uncertainties are checked using simulated $Z \rightarrow ee$ and $W \rightarrow \mu\nu$ events. The spread in fitted W mass values has an RMS of 50 MeV/c^2; the fitted W width values have an RMS deviation of 150 MeV.

The effect of the energy resolution of the electrons on p_T^Z modeling is investigated by degrading the electron energy resolution by a factor of two in the p_T^Z measurement, and repeating the analysis. The study indicates an uncertainty of 35 MeV/c^2 on the W mass, common to the electron and muon channels. The corresponding uncertainty on the W width is 200 MeV, common to both channels. These uncertainties are checked from simulated $Z \rightarrow ee$ and $W \rightarrow \mu\nu$ events by removing the electron energy resolution. Consistent results are observed.

As a demonstration of the ability of the simulation of the event production and recoil to reproduce the data, the spreads and means of $u_{||}$ and $u_{\perp}$ for data and simulation are compared as the maximum value of $|\mathbf{u}|$ is lowered. Tables 7.3 and 7.4 show this comparison for the electron and muon channels. The largest bias to $< u_{||} >$ arises from requiring a minimum transverse energy or momentum for the charged lepton in the event selection; decays of the W

max $\|\mathbf{u}\|$	$< u_{\|\|} >$		$RMS(u_{\|\|})$		$RMS(u_{\perp})$	
(GeV)	(data) (MeV)	(sim) (MeV)	(data) (GeV)	(sim) (GeV)	(data) (GeV)	(sim) (GeV)
20	-473 ± 72	-457	5.36 ± 0.07	5.39	5.28 ± 0.07	5.28
15	-277 ± 63	-309	4.64 ± 0.06	4.78	4.61 ± 0.06	4.72
10	-91 ± 54	-120	3.67 ± 0.05	3.66	3.69 ± 0.05	3.65
5	$+20 \pm 40$	-51	2.23 ± 0.04	2.16	2.19 ± 0.04	2.15
3	-16 ± 40	$+8$	1.42 ± 0.04	1.39	1.37 ± 0.04	1.39

Table 7.3: Variation of mean and RMS of $u_{||}$ and $u_{\perp}$ with maximum $|\mathbf{u}|$ for data and simulation in the $W \rightarrow e\nu$ analysis. The uncertainties are statistical only.

max $\|\mathbf{u}\|$	$< u_{\|\|} >$		$RMS(u_{\|\|})$		$RMS(u_{\perp})$	
(GeV)	(data) (MeV)	(sim) (MeV)	(data) (GeV)	(sim) (GeV)	(data) (GeV)	(sim) (GeV)
20	-514 ± 100	-377	5.48 ± 0.10	5.38	5.28 ± 0.10	5.30
15	-266 ± 90	-251	4.77 ± 0.09	4.76	4.64 ± 0.09	4.70
10	-128 ± 80	-104	3.77 ± 0.08	3.67	3.74 ± 0.08	3.66
5	$+1 \pm 60$	-42	2.25 ± 0.06	2.18	2.14 ± 0.06	2.16
3	$+74 \pm 50$	$+4$	1.43 ± 0.05	1.38	1.37 ± 0.05	1.37

Table 7.4: Variation of mean and RMS of $u_{||}$ and $u_{\perp}$ with maximum $|\mathbf{u}|$ for data and simulation in the $W \rightarrow \mu\nu$ analysis. The uncertainties are statistical only.

boson in which the charged lepton is boosted by the transverse momentum of the W are preferentially kept. Figure 7.4 shows the data and simulation for $< u_{||} >$ as a function of the E_T of the electron. Similarly, Figure 7.5 shows the data and simulation for $< u_{||} >$ as a function of the p_T of the muon. There is a variation of 30 GeV in $< u_{||} >$ over the range of charged-lepton transverse energies, $25 < E_T < 55$ GeV, which the accompanying plots of residuals show is well-modeled. Similar plots of $< u_{||} >$ versus the E_T of the neutrino also show good agreement. The variation of $< u_{||} >$ with the transverse mass of the event is shown in Figure 7.6 for the $W \rightarrow e\nu$ data, and in Figure 7.7 for the $W \rightarrow \mu\nu$ data. These variations are much smaller (which is why the transverse mass is used to extract the W mass), and are well-described by the simulation. Plots of $< u_{||} >$ versus $|\mathbf{u}|$ are sensitive tests of the quality of the event modeling and exhibit good agreement between data and simulation in Figures 7.6 and 7.7.

7.3.3 Proton parton distribution functions

Varying the parton distribution functions (PDFs) of the proton varies the distribution of the W longitudinal momentum, and, through acceptance effects, the lineshape of the transverse mass spectrum. Due to the missing neutrino, the W longitudinal momentum is not directly measurable in W decays. The longitudinal momentum distribution cannot be constrained by the Z data either, since Z production is sensitive to different parton distributions ($u\bar{u} + d\bar{d}$ is different from $u\bar{d}$). However, the CDF measurement of the forward-backward charge asymmetry in W decay [32] can be used to constrain the longitudinal momentum distribution of the W. The charge asymmetry gets larger as the longitudinal momentum distribution broadens. The asymmetry measurement is directly sensitive to those components of the PDFs which influence W production at the Tevatron, and is able to distinguish among parton distributions. The MRS D$'_-$ set [52] is chosen as the default PDF since

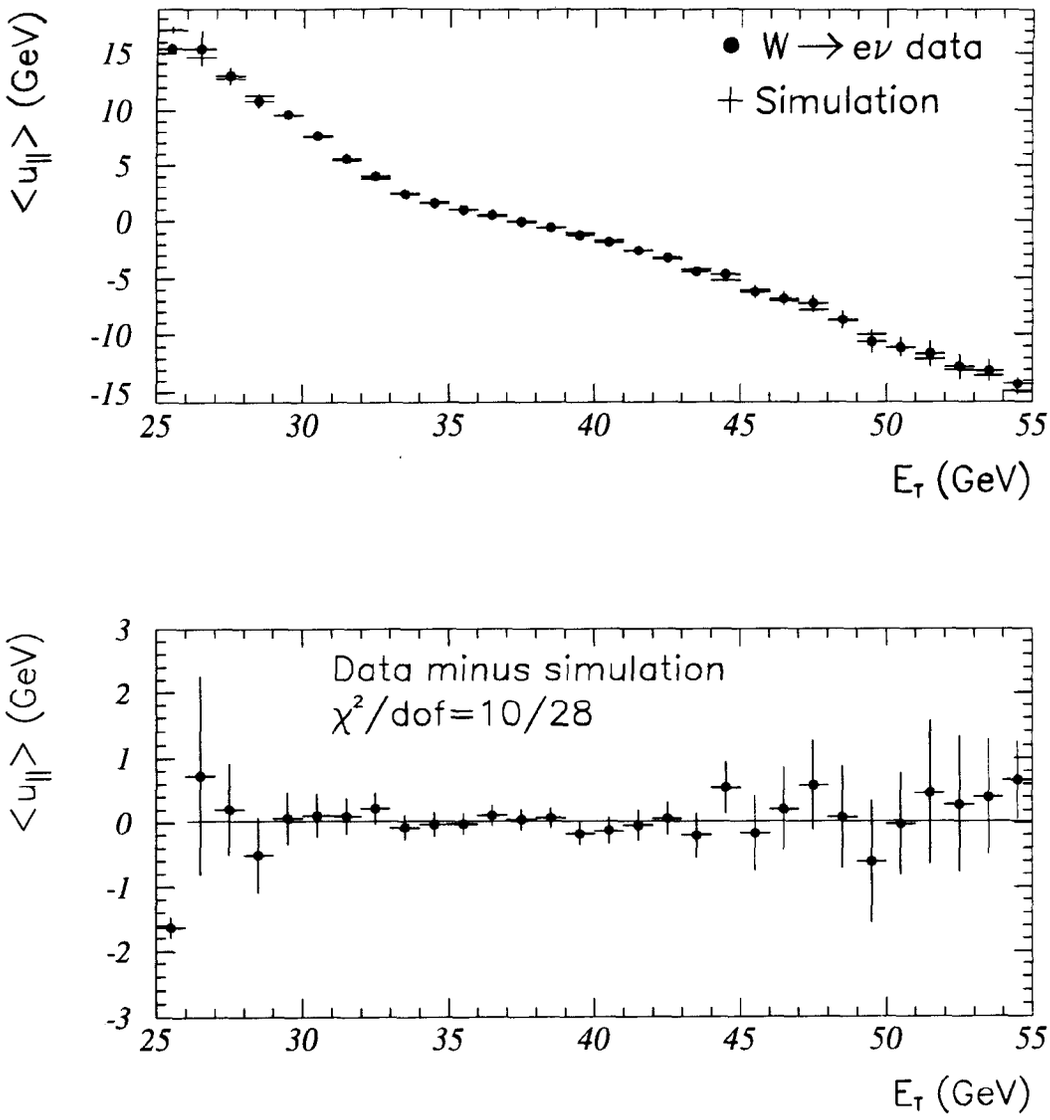

Figure 7.4: Upper: Data versus predicted value of $< u_{\parallel} >$ as a function of the electron E_T for the $W \rightarrow e\nu$ data. Lower: The residuals of the data minus the simulation.

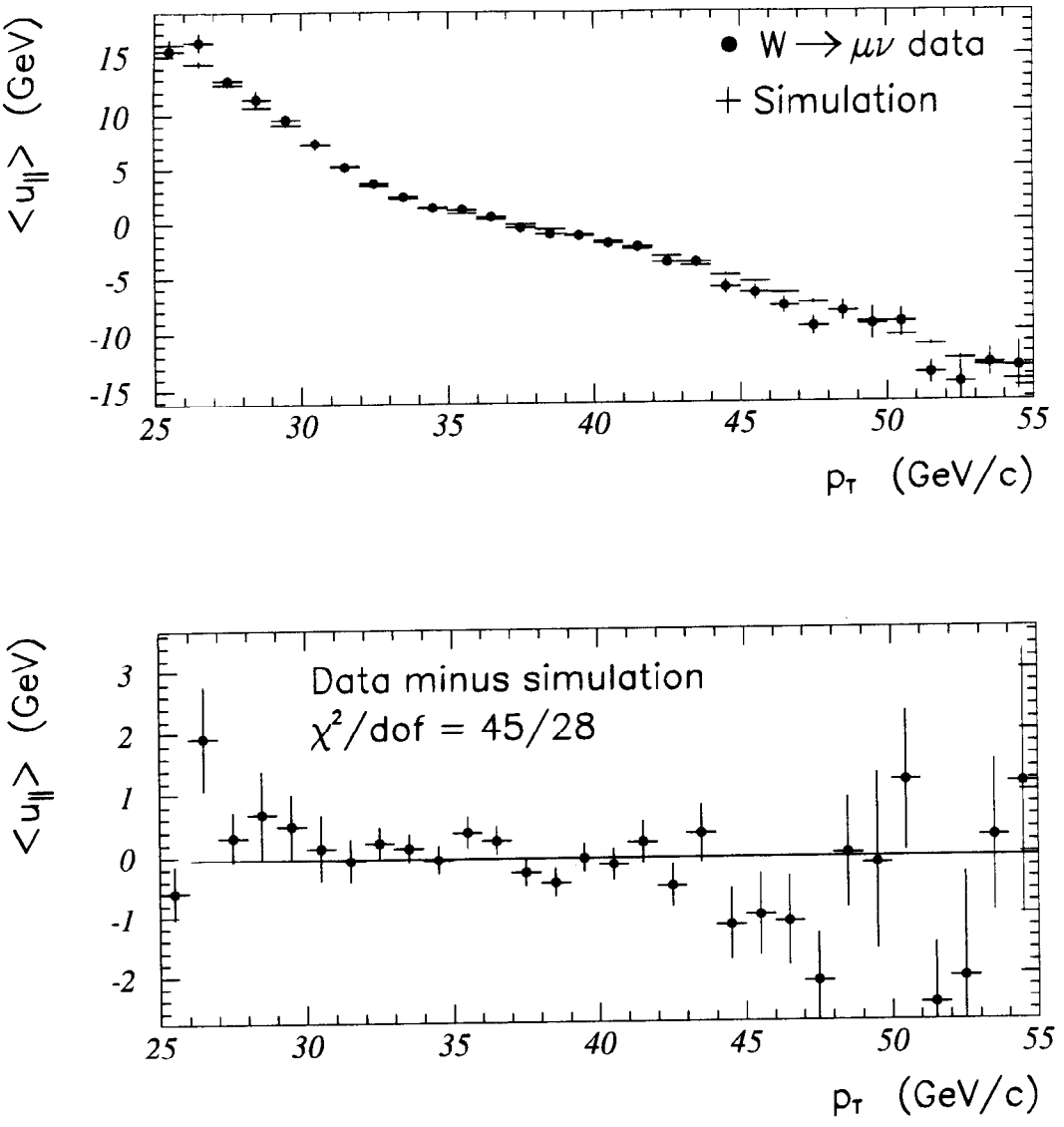

Figure 7.5: Upper: Data versus predicted value of $< u_{||} >$ as a function of the muon p_T for the $W \rightarrow \mu\nu$ data. Lower: The residuals of the data minus the simulation.

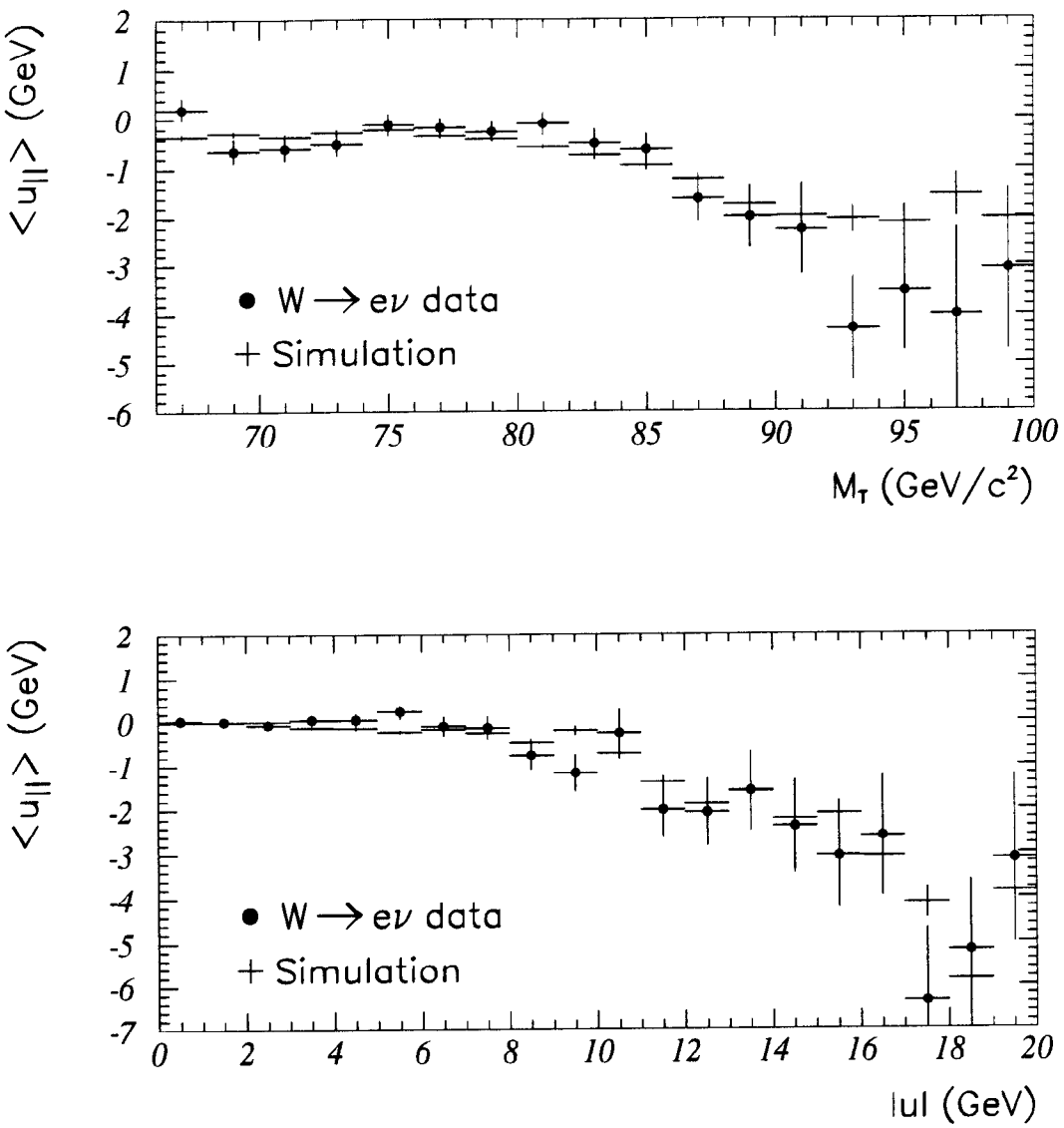

Figure 7.6: Upper: Data versus predicted value of $< u_{\parallel} >$ as a function of M_T for the $W \rightarrow e\nu$ data. Lower: Same as a function of u.

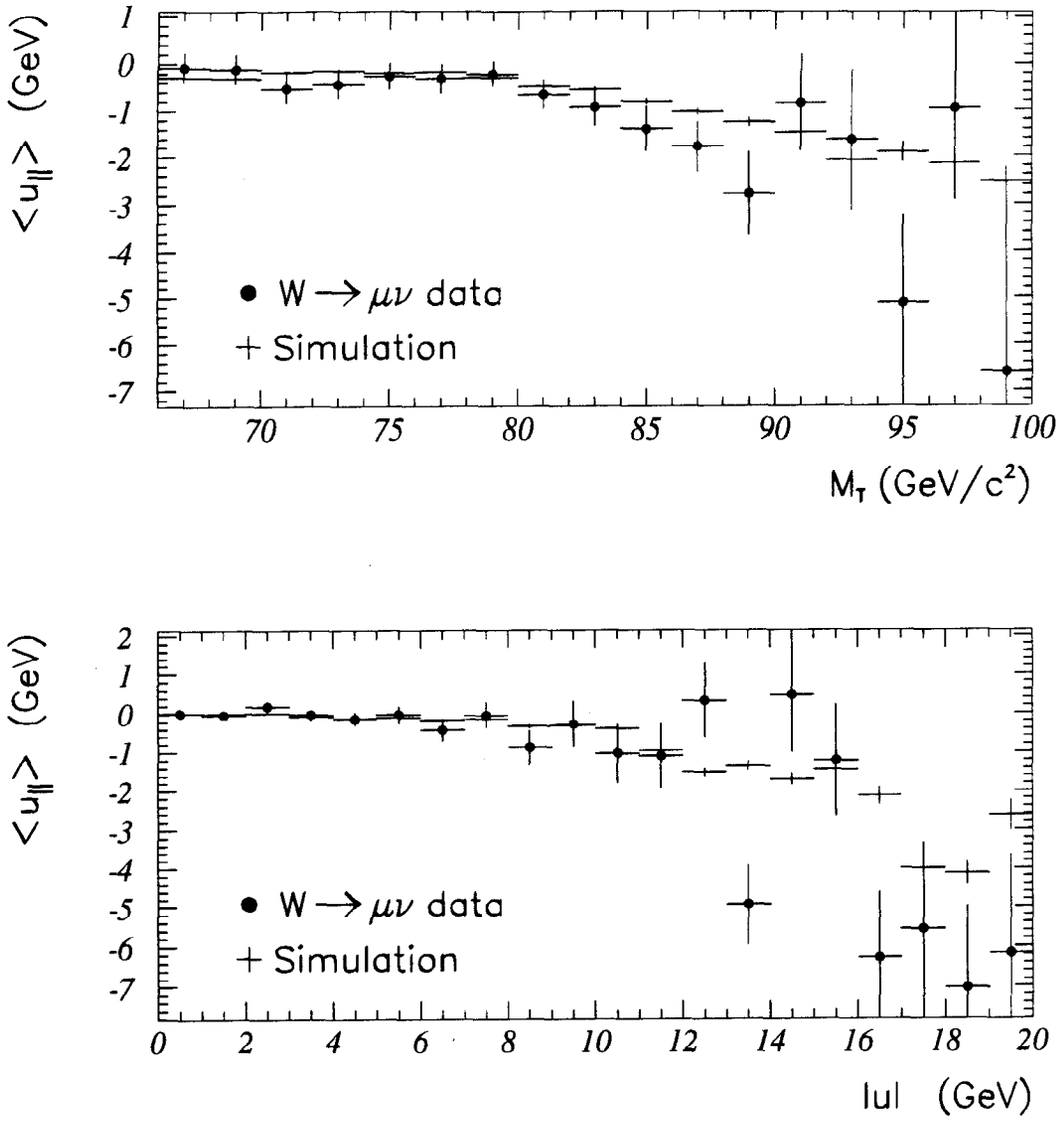

Figure 7.7: Upper: Data versus predicted value of $< u_{||} >$ as a function of M_T for the $W \rightarrow \mu\nu$ data. Lower: Same as a function of $|\mathbf{u}|$.

it is favored by the CDF charge asymmetry measurement and deep inelastic scattering experiments [61].

To quantify how well the various PDFs reproduce the data, for each PDF in Table 7.5, the weighted mean of the charge asymmetry [32] in the region $0.2 < |\eta| < 1.7$ is calculated ($A_{\rm PDF}$). The mean is compared to the measurement ($A_{\rm DATA}$) to yield a significance,

$$\zeta = \frac{A_{\rm PDF} - A_{\rm DATA}}{\delta A_{\rm DATA}}, \tag{7.4}$$

where $\delta A_{\rm DATA}$ is the uncertainty in the mean charge asymmetry measurement. The fitted W mass is extracted using each PDF. The values of ζ and ΔM_W ($= M_W^{\rm PDF} - M_W^{\rm MRS\ D'_-}$) are listed in Table 7.5 and their correlations are shown in Figures 7.8 ($W \rightarrow e\nu$) and 7.9 ($W \rightarrow \mu\nu$). These correlations between the fitted W mass and the charge asymmetry are expected since a larger charge asymmetry (a larger mean W longitudinal momentum) leads to a smaller average M_T^W, and hence a larger fitted W mass [62, 63]. The uncertainty in mass due to the choice of PDF is taken as half the mass difference between points A and B in Figures 7.8 and 7.9, corresponding to $|\zeta| < 2$. This is 50 MeV/c^2 for the region $65 < M_T^W < 100$ GeV/c^2, and is common to the electron and muon mass measurements. Although the smaller rapidity coverage of the muon detector causes greater sensitivity to the W longitudinal momentum distribution, the effect is small.

7.3.4 Charged-lepton energy resolutions

Tables 7.6 ($W \rightarrow e\nu$) and 7.7 ($W \rightarrow \mu\nu$) show the variation in the fitted W mass when artificial data simulated with energy or momentum resolutions other than the favored values are fit to the lineshapes as described in Section 9. For electrons, the corresponding uncertainties are 80 MeV/c^2 on the W mass and 280 MeV on the W width. For muons, the corresponding uncertainties are 60 MeV/c^2 on the W mass and 250 MeV on the W width.

PDF	ζ	ΔM_W^e (MeV/c^2)	ΔM_W^μ (MeV/c^2)
CTEQ 2M	+ 4.56	+ 14	+ 20
CTEQ 2MF	+ 3.76	+ 8	+ 10
CTEQ 2ML	+ 3.51	+ 11	+ 14
GRV	+ 3.04	+ 36	+ 52
CTEQ 2MS	+ 2.94	− 9	− 11
CTEQ 1M	+ 2.09	− 1	− 1
CTEQ 1MS	+ 1.51	− 16	− 24
MRS A (Prelim.)	+ 0.87	− 23	− 26
MRS D′_	+ 0.50	0	0
MRS H	− 0.05	− 6	− 6
MRS D_0'	− 0.94	− 21	− 17
HMRS B	− 1.20	− 33	− 35
MT B1	− 3.21	− 66	− 76
KMRS B_0	− 3.59	− 76	− 89
MRS B′	− 4.10	− 62	− 68
MRS E′	− 4.89	− 78	− 96
MRS B		− 43	− 45

Table 7.5: Dependence of the W charge asymmetry and the W mass on PDF [52] choice. The Monte Carlo statistical uncertainty is ~15 MeV/c^2. MRS D′_ is the default choice of the current analysis. MRS B is the default choice of the previously published CDF W mass measurement [10].

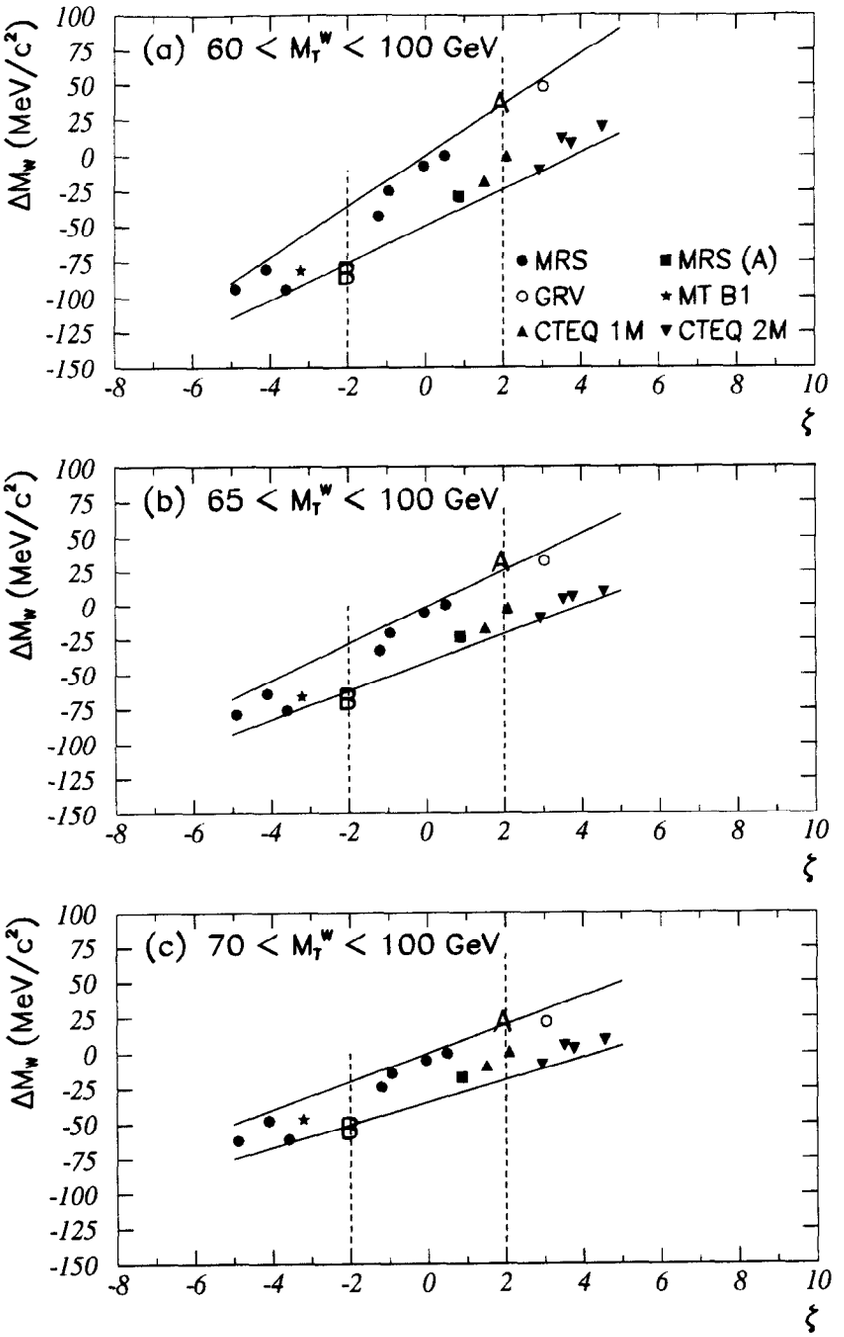

Figure 7.8: The correlation between ΔM_W^e (MeV/c^2) and ζ using various PDFs for the $W \rightarrow e\nu$ sample, where $\Delta M_W^e = M_W^{\rm PDF} - M_W^{\rm MRS\ D'_-}$. The M_T^W regions for the W mass fitting are (a) $60 < M_T^W < 100$ GeV/c^2, (b) $65 < M_T^W < 100$ GeV/c^2, and (c) $70 < M_T^W < 100$ GeV/c^2. The solid lines are taken as bounds on PDF effects. The dashed lines indidate $|\zeta| = 2$. The uncertainty on the W mass is half of ΔM_W^e between points A and B.

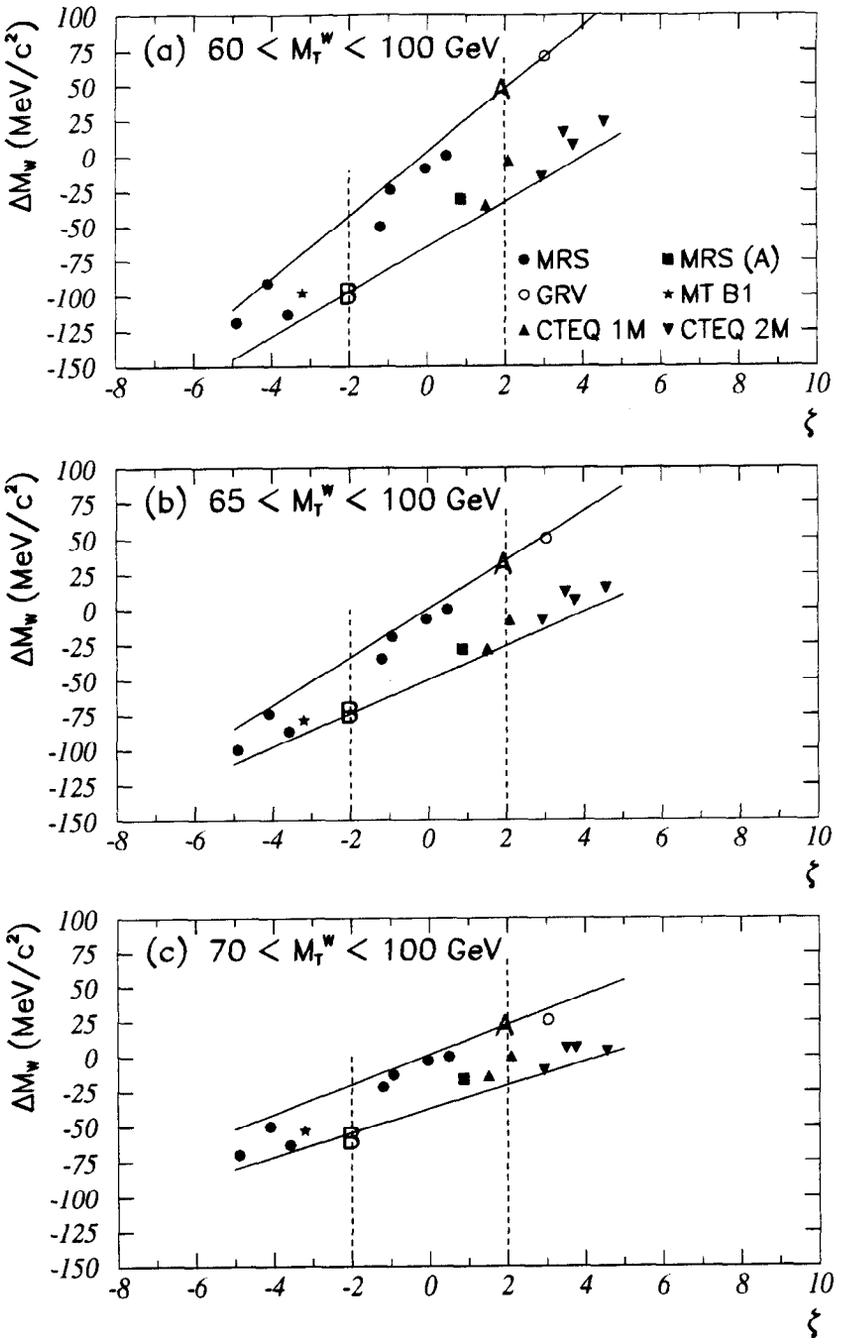

Figure 7.9: The correlation between ΔM_W^{μ} (MeV/c^2) and ζ using various PDFs for the $W \to \mu\nu$ sample, where $\Delta M_W^{\mu} = M_W^{\rm PDF} - M_W^{\rm MRS\ D'_-}$. The M_T^W regions for the W mass fitting are (a) $60 < M_T^W < 100$ GeV/c^2, (b) $65 < M_T^W < 100$ GeV/c^2, and (c) $70 < M_T^W < 100$ GeV/c^2. The solid lines are taken as bounds on PDF effects. The dashed lines indidate $|\zeta| = 2$. The uncertainty on the W mass is half of ΔM_W^{μ} between points A and B.

κ (%)	ΔM_W^e (MeV/c^2)	$\Delta\Gamma_W^e$ (MeV)
0.0	-31 ± 14	-162 ± 24
0.5	-25 ± 14	-132 ± 26
1.0	$\equiv 0$	$\equiv 0$
1.5	$+34 \pm 14$	$+64 \pm 21$
2.0	$+63 \pm 14$	$+247 \pm 20$
2.5	$+135 \pm 14$	$+521 \pm 30$

Table 7.6: Variation in the W mass and width from electrons if a constant term κ in the electron energy resolution (see Equation 5.1) other than the favored value is used. The change in the W width is for a simultaneous fit to both mass and width.

$\delta p_T/p_T^2$ ((GeV/c)$^{-1}$)	ΔM_W^μ (MeV/c^2)	$\Delta\Gamma_W^\mu$ (MeV)
0.00063	-117 ± 23	-463 ± 45
0.00072	-36 ± 23	-244 ± 45
0.00081	$\equiv 0$	$\equiv 0$
0.00090	$+68 \pm 23$	$+220 \pm 45$
0.00099	$+145 \pm 23$	$+430 \pm 45$

Table 7.7: Variation in the W mass and width from muons if a muon momentum resolution (see Equation 4.2) other than the favored value is used. The change in the W width is for a simultaneous fit to both mass and width.

Γ_W (GeV)	ΔM^e (MeV/c^2)	ΔM^μ (MeV/c^2)
1.664	-97 ± 14	-102 ± 10
1.864	-40 ± 14	-50 ± 10
2.064	$\equiv 0$	$\equiv 0$
2.264	$+21 \pm 14$	$+48 \pm 10$
2.464	$+102 \pm 14$	$+94 \pm 10$

Table 7.8: Variation in the fitted W mass as the W width used in the simulation is varied.

7.3.5 W width

The value of the W width used in the simulation is the measured value of 2.064 ± 0.085 GeV/c^2 [43]. Table 7.8 shows the variation in the fitted W mass as the W width is varied in artificial data. The resultant uncertainty on the W mass is 20 MeV/c^2, common to both the electron and muon measurements.

7.3.6 Trigger bias

The triggers for the $W \rightarrow \ell\nu$ sample may affect the W mass measurement if there is a kinematic dependence upon the efficiency. The trigger efficiencies are not included in the model. Their effect on the W mass is estimated.

Events in the $W \rightarrow e\nu$ sample satisfy at least one of three triggers: 1) a trigger requiring an electromagnetic cluster with $E_T > 16$ GeV with a calorimeter transverse energy imbalance ($\not\!\!E_T$) requirement of $\not\!\!E_T > 20$ GeV, where no track is required, 2) an inclusive electron trigger at 9 GeV which requires a track, and 3) a tau trigger that requires a "jet" matched to a track and $\not\!\!E_T > 20$ GeV. No events come in exclusively on an additional trigger requiring only $\not\!\!E_T > 35$ GeV. The trigger requiring an electromagnetic cluster with $\not\!\!E_T$ is 99.8% efficient. Given such high efficiency, the 9-GeV inclusive

electron trigger serves as an adequate backup with its 93.1% efficiency. Only three events fail both of the first two triggers due to hardware failures during electromagnetic cluster finding. Less than one event is expected to have been missed by all three triggers. The trigger bias on the $W \rightarrow e\nu$ measurement is negligible.

The $W \rightarrow \mu\nu$ sample requires muons at all three trigger levels. Of these, only the Level-2 trigger has a significant dependence on the kinematics of the muon; its efficiency varies by $\sim 5\%$ with η of the tracks (see Figure 7.10). This variation, however, leads to a negligible variation ($\sim$ 2 MeV/c^2) on the W mass since M_T^W is approximately invariant under p_Z boosts. The W mass is more sensitive to an inefficiency as a function of p_T^μ since M_T^W is directly related to p_T^μ (see Equation 2.3). No p_T^μ-dependence is seen (see Figure 7.10), but the statistical limitation on measuring such a dependence leads to a 25 MeV/c^2 uncertainty on the $W \rightarrow \mu\nu$ mass.

7.3.7 Higher-order corrections to W production

The physics simulations used for the present W mass measurement use a Born-level matrix element calculation for W production, augmented by a realistic p_T^W distribution. The true production mechanisms (even at low p_T^W) include additional higher-order QCD corrections. These corrections will affect the W longitudinal momentum distribution, as well as the polarization of the produced W. No complete theoretical calculation, including all these effects, is presently available. In the following, the expected contributions of these two effects are estimated by using the results of partial calculations.

A potential problem with the leading-order model is that it does not change the polarization of the W as the p_T of the W increases. In Reference [64] it is shown that higher-order QCD corrections add a term to the angular distribution of charged-leptons from W decay. When averaged over charges, the polar-angle (θ^*) distribution of the charged leptons in the rest frame of

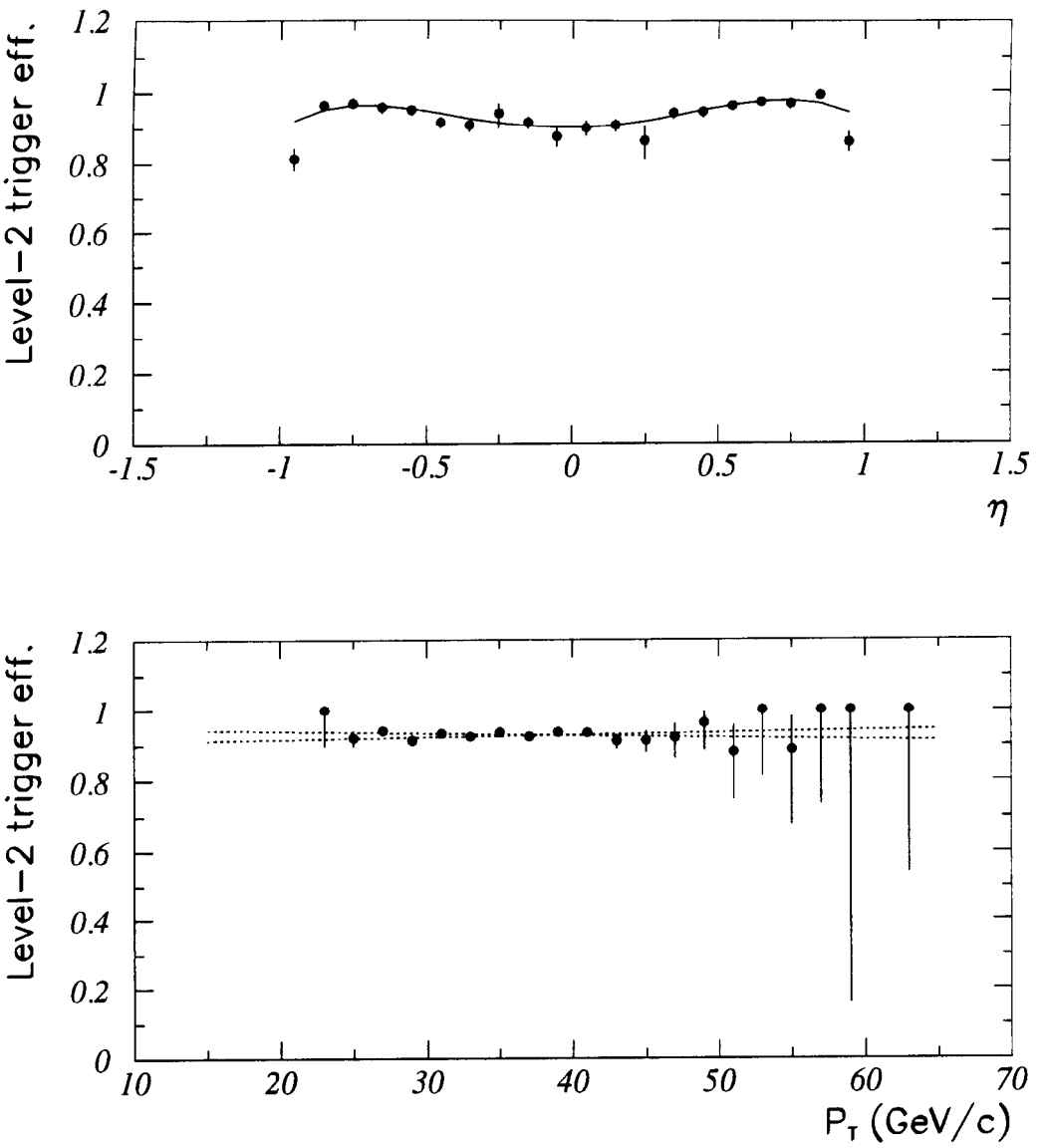

Figure 7.10: Upper: The Level-2 muon trigger efficiency as a function of track η. The solid curve is a 4-th order polynomial fit. Lower: The Level-2 muon trigger efficiency as a function of track p_T (GeV/c). The dotted lines indicate ± 1-σ uncertainties in the slope of a linear fit.

the W becomes

$$\frac{d\sigma}{d(\cos\theta^*)} = (1 + \cos^2\theta^*) + a\ (1 - 3\cos^2\theta^*), \tag{7.5}$$

where the first term in parentheses is reproduced by the leading-order model, and the second term is the correction due to higher-order effects. The coefficient a is always positive. For simulated W events selected as in the mass sample, a is calculated to be typically 0.007, and is usually less than 0.03. A study in which artificial data with this effect included are fit to the leading-order lineshapes used in Section 9 shows that a 10 MeV/c^2 uncertainty should be taken on the W mass for this effect.

A theoretical model may be used to isolate and estimate the bias due solely to possible correlations between p_T^W and W rapidity. To estimate the uncertainty a theoretical double-differential spectrum of W production in p_T and rapidity provided by Arnold and Kauffman [56] with $\Lambda_{QCD} = 300$ MeV, $S_{np} = 1.36$ GeV$^2 b^2$, and $b_{\max}$ =(2 GeV)$^{-1}$ is used. This spectrum is constrained using the same procedure as that used to constrain the spectrum derived from the $Z \rightarrow ee$ data, resulting in an r factor of 0.977. First, as a check, artificial data are generated using this p_T^W spectrum without the rapidity correlation. The returned W mass for these data is shifted by $+20 \pm 10$ MeV/c^2. This shift is smaller than the systematic uncertainty taken for uncertainties in the p_T^W distribution. Note that there is no reason to believe the theoretical spectrum to be "correct" at this level, anyway. The shift in the mass between fits using this artificial data generated with and without the rapidity correlation included is 13 ± 14 MeV/c^2. Although the shift is consistent with no effect, 15 MeV/c^2 is taken as the systematic uncertainty, common to the electron and muon analysis.

7.4 Summary

The uncertainty on the W mass due to uncertainty on the p_T^W spectrum is 45 MeV/c^2 for both the $W \rightarrow e\nu$ and $W \rightarrow \mu\nu$ analyses, of which 25 MeV/c^2 is common. The modeling of the calorimeter response to the recoil contributes a 60 MeV/c^2 uncertainty, common to both channels. Uncertainties in the electron energy resolution and muon momentum resolution contribute 80 MeV/c^2 and 60 MeV/c^2 uncertainties, respectively. These are independent. The choice of parton distribution functions is shown to contribute a 50 MeV/c^2 uncertainty on the W mass common to the electron and muon measurements. The effects of trigger bias have been estimated to be negligible for the $W \rightarrow e\nu$ measurement, but contribute a 25 MeV/c^2 uncertainty on the $W \rightarrow \mu\nu$ measurement. The effects of higher-order QCD corrections on the W polarization and on a correlation between p_T^W and rapidity are investigated. No measurable shift of the W mass is observed. The ability to measure such a shift, 20 MeV/c^2, is taken as an uncertainty for both the $W \rightarrow e\nu$ and $W \rightarrow \mu\nu$ analyses, of which 10 MeV/c^2 is from effects in the W polarization and 15 MeV/c^2 is from effects in the correlation between p_T^W and rapidity.

Section 8

BACKGROUNDS AND RADIATIVE CORRECTIONS

Backgrounds contribute events to the signal region distorting the lineshape. Radiative corrections also modify the lineshape. This section describes the treatment of these processes, and presents the estimated mass shifts and uncertainties.

8.1 Backgrounds

This section describes how the following processes are incorporated into the analysis:

1. $W \to \tau\nu \to \ell\nu\nu\nu$
2. $Z \to \ell\ell$ where the second charged lepton is not found
3. $W \to \tau\nu \to h + X$ ("one-prong" hadronic τ decays)
4. $b\bar{b}$ production, $c\bar{c}$ production, and jets faking leptons ("fakes")
5. $Z \to \tau\tau$ where all decays of τ leptons are considered
6. WW and $t\bar{t}$ production
7. cosmic rays

As can be seen in Figure 8.1, backgrounds have a lower average transverse mass than $W \rightarrow \ell\nu$ decay, and, if not accounted for, will lower the fitted mass. In addition, some backgrounds may affect the distributions of quantities that serve as checks against systematic error, such as $u_{||}$.

To understand the effects of the background processes on $< u_{||} >$ and other quantities, the backgrounds have been incorporated into the simulation. The methods by which each of the seven background processes are simulated and the effects on the mass measurement are addressed separately for the electron and muon channels in the following sections.

8.1.1 $W \rightarrow e\nu$ backgrounds

The $W \rightarrow \tau\nu \rightarrow e\nu\nu\nu$ process is included as described in Section 7.2. Few $W \rightarrow \tau\nu \rightarrow e\nu\nu\nu$ events pass the kinematic cuts. For $M_W = 80.5$ GeV/c^2, the final sample is estimated to contain 0.79% of its 5718 events from this process. This is the largest background in the $W \rightarrow e\nu$ sample, and is also the easiest to simulate since the W production characteristics are the same as for the $W \rightarrow e\nu$ signal.

A $Z \rightarrow ee$ event can mimic a $W \rightarrow e\nu$ event if one of the electrons is either not observed or is mis-measured, creating significant $\not\!\!E_T$. Because the rate of these "lost-Z" events is low, a correction calculated from ISAJET [65] and a CDF detector simulation is adequate. The efficiency for detecting an additional high-p_T track falls rapidly for $|\eta| > 1.4$ because the electron does not traverse enough wire layers in the tracking volume to be reconstructed. As a result, missed electrons will tend to be in cracks in the forward regions. The kinematics and the residual energy deposited by the missed electron cause the transverse mass spectrum of these events, shown in Figure 8.1, to fall with M_T rather than form a peak near M_Z. The spectrum of $u_{||}$ for these events is shown by the simulation to have a long negative tail due to energy left by

Cuts	f
$E_T > 20$, $p_T > 12$, $\not\!\!E_T < 20$	0.43 ± 0.07
$E_T > 20$, $p_T > 12$, $\not\!\!E_T < 10$	0.39 ± 0.08
$E_T > 25$, $p_T > 15$, $\not\!\!E_T < 20$	0.34 ± 0.11
$E_T > 25$, $p_T > 15$, $\not\!\!E_T < 10$	0.31 ± 0.14
$E_T > 30$, $p_T > 18$, $\not\!\!E_T < 20$	0.41 ± 0.21
$E_T > 30$, $p_T > 18$, $\not\!\!E_T < 10$	0.38 ± 0.17

Table 8.1: Variation in f, the ratio of jet events with an isolated track to those with a high track multiplicity (more than four tracks within the track isolation cone around the electron), for a range of kinematic cuts. Units on cuts are in GeV and GeV/c for E and p, respectively.

the missed electrons. Such events are expected to be 0.12% of the 5718-event sample.

The number of events in the sample due to electrons from bottom and charm decays and to fakes may be estimated from inclusive 20 GeV jet data. Since jets and heavy-flavor decays are characterized by high-track multiplicities, a measurement of their track multiplicity distribution allows an estimate of the few background events with a single track. The multiplicity of tracks with p_T greater than 1.0 GeV/c in the track isolation cone ($\sqrt{(\Delta\phi)^2 + (\Delta\eta)^2} < 0.25$) around the electrons is measured for jets passing all other electron identification criteria. The $Z \rightarrow ee$ data indicate that events with four or more tracks within the isolation cone form a pure background sample. The ratio (f) of events with one isolated track to those with four or more tracks in the isolation cone is measured in the jet data. Table 8.1 shows the values of f for several kinematic selection criteria. There are 25 $W \rightarrow e\nu$ events with four or more tracks in the isolation cone, but which satisfy all other selection criteria. Combined with a value of f=0.43 (the largest value in Table 8.1, to be conservative), these 25 events correspond to a background fraction of 0.19% in the $W \rightarrow e\nu$ sample. Checks using different track mul-

tiplicity normalizations and samples enriched in heavy flavor are consistent with this background fraction. Events in the W sample which fail the track multiplicity cut are used to predict the shape of the background, shown in Figure 8.1.

The "one-prong" hadronic decays of tau leptons from W bosons, $W \rightarrow \tau\nu \rightarrow h + X$, constitute a background not normally considered in high-E_T electron analyses. However, the W mass measurement is forced to make only loose cuts on the electron shower profile to reduce biases on events with large bremsstrahlung. Such events would also be likely to bias the tail of E/p. A study using ISAJET and a CDF detector simulation shows that the sum of the contributions from the decays $\tau^{\pm} \rightarrow \pi^{\pm}\nu X$ and $\tau^{\pm} \rightarrow K^{\pm}\nu X$ is small, as shown in Table 8.2 and Figure 8.1.

The number of events from the process $Z \rightarrow \tau\tau$ is estimated using ISAJET and a CDF detector simulation. All decay modes of each τ are included. The effect of this process on the W mass is small, and is summarized in Table 8.2 and Figure 8.1.

The effect of direct W-pair production is calculated using a cross section of 10 pb [66]. The contribution to the observed event rate is 0.6 events in the sample (0.01%). Top-quark pair production with a top mass of 174 GeV/c^2 and cross section of 13.9 pb [16, 67] contributes 0.2 events. Since the sum of these processes produces less than one event in the sample, and because the processes produce electrons from real W bosons which will not have a significantly biased transverse mass distribution, any effects from these processes are negligible.

Cosmic-ray muons may infrequently emit bremsstrahlung in the CEM and be identified as electrons. Of the events failing only the 1.0 cm impact parameter cut, three are identified by a visual inspection to be cosmic rays. These events are otherwise quiet, have muon hits aligned with the track on both sides of the detector and have hits in the opposite side of the CTC

in azimuth. Extrapolating into the region with impact parameter less than 1.0 cm indicates that less than one event is expected in the sample. The effect of cosmic-ray background is thus negligible.

The uncertainty due to the largest background process, $W \rightarrow \tau\nu \rightarrow e\nu\nu\nu$, is negligible since it is precisely simulated. The omission of this process in the lineshapes is seen to cause a shift in the W mass of -50 MeV/c^2. The omission of all the other background processes in the event model is seen to shift the W mass by -10 MeV/c^2. This shift, although corrected for, is also taken as the uncertainty.

8.1.2 $W \rightarrow \mu\nu$ backgrounds

Few $W \rightarrow \tau\nu \rightarrow \mu\nu\nu\nu$ events pass the kinematic selection requirements on p_T^μ, E_T^ν, and M_T^W. The final sample is estimated to contain 0.78% of its 3268 events from this process. This background, if omitted from the model, would lead to a W mass shift of -57 MeV/c^2.

The largest background in the $W \rightarrow \mu\nu$ sample comes from the $Z \rightarrow \mu\mu$ process with one of the muons undetected by the CTC. This background is large because the CTC has limited η coverage. The coverage extends to $|\eta| < 1.7$, although the tracking efficiency falls with increasing $|\eta|$ for $|\eta| > 1.0$. This background is estimated to be (3.6 ± 0.5) %, and, if omitted from the model, would lead to a W mass shift of -120 ± 20 MeV/c^2. The uncertainty in the background estimate comes from two sources: the uncertainty in the measured tracking efficiency, and the choice of parton distribution functions. By varying the absolute tracking efficiency in the region of $1.0 < |\eta| < 1.7$ by 10% (which is conservative), the uncertainty due to the tracking efficiency uncertainty is estimated to be 0.5% in the amount of background, and 20 MeV/c^2 on the W mass. The contribution from the uncertainty in the tracking efficiency in the region of $|\eta| < 1.0$ is less than 5 MeV/c^2. The number of events from $Z \rightarrow \mu\mu$ decay that enter the W sample potentially have a large parton

distribution function dependence since they involve the loss of leptons at high η. Such leptons preferentially come from the high-rapidity tail of the Z production cross section, which depends sensitively on the small-x behavior of the parton distribution functions. The uncertainty due to the choice of parton distribution functions is estimated to be 0.2% in the amount of background and 10 MeV/c^2 on the W mass. The effect on $< u_{||} >$ from $Z \rightarrow \mu\mu$ background is significant because the amount of contamination is large and the lost muon deposits about 2.3 GeV of energy in the calorimeters in the opposite direction to the found muon. A shift of -36 ± 5 MeV in $< u_{||} >$ is estimated; this shift is included in the lineshape modeling.

Background from jet and heavy-flavor production is estimated using the $W \rightarrow \mu\nu$ data sample. The sample is divided into two by using Σp_T, the sum of the p_T of tracks with p_T greater than 1.0 GeV/c in a cone ($\sqrt{(\Delta\phi)^2 + (\Delta\eta)^2} < 0.4$) around the muon. A sample of non-isolated muons is made with a cut $\Sigma p_T > 2$ GeV/c, which should contain most of the background. A sample which is more likely to be background-free is made by requiring $\Sigma p_T < 2$ GeV/c. Distributions of $\phi_{\nu\text{jet}}$ of the two samples are then compared, where $\phi_{\nu\text{jet}}$ is the azimuthal angle between the neutrino direction and the direction of the highest E_T jet with $E_T > 5$ GeV. Background events tend to have $\phi_{\nu\text{jet}} \sim 0°$ or $\sim 180°$. By normalizing the distributions in the range $30 < \phi_{\nu\text{jet}} < 150°$, the non-isolated sample has an excess of 6 events (0.2%) over the isolated sample in the range $\phi_{\nu\text{jet}} < 30°$ or $\phi_{\nu\text{jet}} > 150°$. The W mass shift due to these 6 events is -15 ± 15 MeV/c^2. This background is not included in the model; a correction is instead applied to the fitted W mass.

Cosmic rays can appear as two back-to-back tracks in ϕ when they cross the detector in time with $\bar{p}p$ collisions, due to the time difference between the two 'tracks'. The requirement of no other tracks with $p_T > 10$ GeV/c removes these events. Sometimes cosmic rays have only one track reconstructed.

Requirements of $|z_{vertex} - z_{track}| < 2$ cm and $|D_o| < 0.2$ cm remove most of these events. The number of cosmic rays remaining in the final sample is estimated using events which fail the $|z_{vertex} - z_{track}| < 2$ cm or $|D_o| < 0.2$ cm criteria, but which pass all the other selection criteria (see Table 4.1). A control sample of identified cosmic-ray events is formed from these events by visual inspection. The D_o and $z_{vertex} - z_{track}$ distributions of this control sample are used to estimate the background in the regions $|z_{vertex} - z_{track}| < 2$ cm and $|D_o| < 0.2$ cm. The expected number of cosmic-ray events in the final sample is $0.5^{+2.0}_{-0.5}$. Adding two cosmic-ray events in the $W \rightarrow \mu\nu$ sample would lead to a shift of 5 MeV/c^2, which is taken as the uncertainty. No correction is applied to the W mass.

Background from the process $Z \rightarrow \tau\tau$ is estimated using HERWIG [68] and the CDF detector simulation. This background is estimated to be $(0.05 \pm 0.05)\%$ and leads to a shift of -5 ± 5 MeV/c^2 on the $W \rightarrow \mu\nu$ mass. This background is not included in the model; a correction is instead applied to the fitted W mass.

Effects from direct W-pair production and top-quark pair production are negligible.

The number of events and transverse mass distributions for these backgrounds are shown in Figure 8.1. Large backgrounds ($W \rightarrow \tau\nu \rightarrow \mu\nu\nu\nu$ and $Z \rightarrow \mu\mu$), if not included in the model, would lead to a shift of -177 ± 20 MeV/c^2 on the W mass. Small backgrounds (heavy-flavor decays, fakes, $Z \rightarrow \tau\tau$, and cosmic rays) are not included in the model; the effect of these backgrounds is to shift the W mass by -20 ± 15 MeV/c^2. A correction of $+20 \pm 15$ MeV/c^2 is thus applied to the fitted W mass.

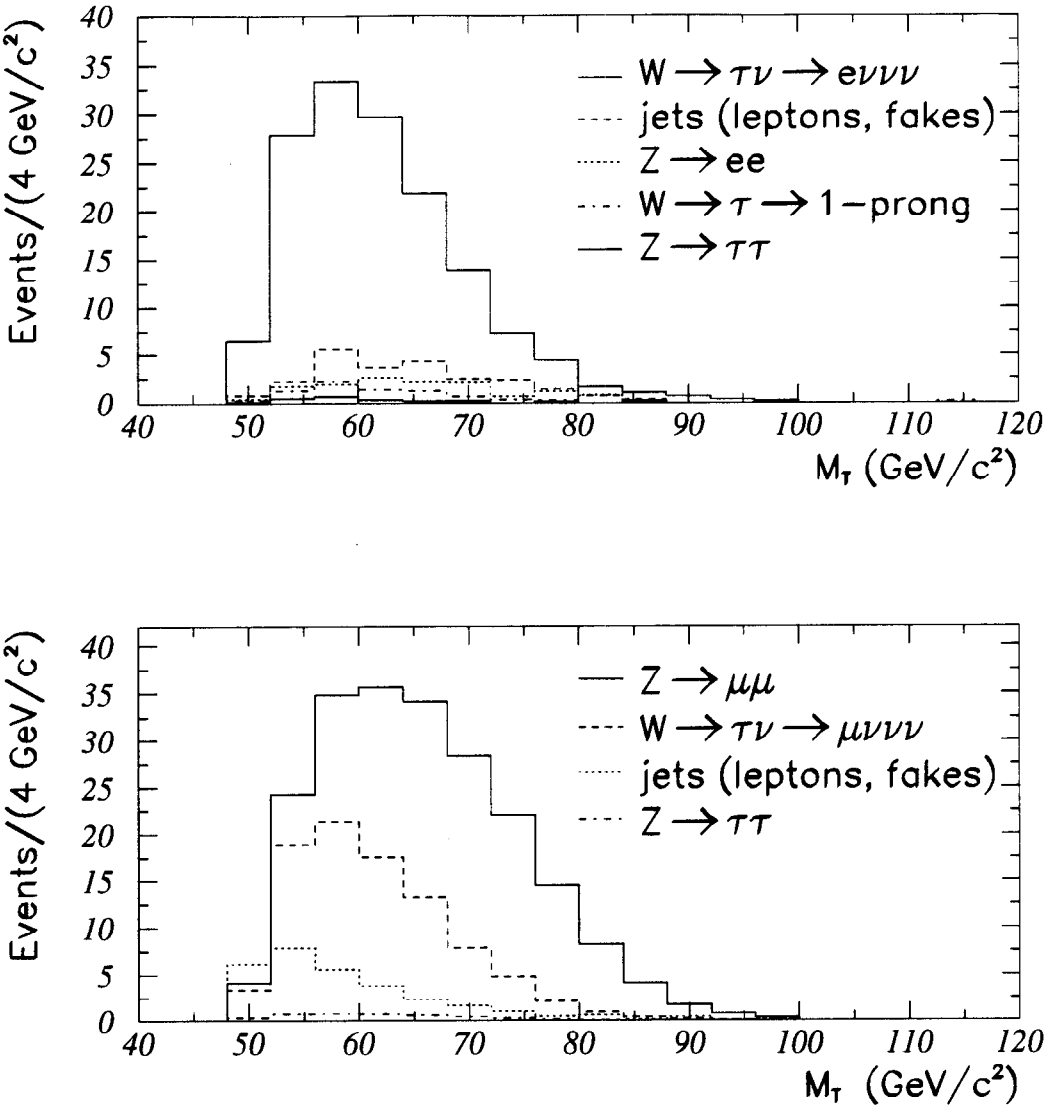

Figure 8.1: Upper: Transverse mass distributions of background in the $W \rightarrow e\nu$ sample. Lower: Transverse mass distributions of background in the $W \rightarrow \mu\nu$ sample.

Decay	Events in $W \to e\nu$ sample	Events in $W \to \mu\nu$ sample
$W \to \tau\nu \to \ell\nu\nu\nu$	45	26
Lost $Z \to \ell\ell$	7	118 ± 16
$W \to \tau\nu \to$"one-prong" hadrons	2	0
heavy-flavor decays and fakes	11	6 ± 6
$Z \to \tau\tau$	2	2 ± 2
Cosmic rays	0	$0.5^{+2.0}_{-0.5}$

Table 8.2: Backgrounds in the W samples. To estimate the uncertainty due to backgrounds in the $W \to e\nu$ channel, the sum of all backgrounds other than $W \to \tau\nu \to e\nu\nu\nu$ is varied by 100%. For the $W \to \mu\nu$ analysis the mass shift from each background is measured individually, as discussed in the text.

8.2 Radiative Corrections

$W\gamma$ production and radiative W decays ($W \to \ell\nu\gamma$) are simulated using the calculation by Berends and Kleiss [40, 41]. Most photons are from radiative W decays and tend to be collinear with the lepton, often showering in the same calorimeter towers as the lepton. For the electron channel, these photons are merged with the electron cluster; for the muon channel, they are removed by the lepton removal procedure. Radiative effects from collinear photons are thus expected to be larger in the muon channel. Photons not collinear with the lepton are included in the calculation of $\mathbf{u}$, and have an effect that is similar in both the electron and muon channels. Shifts in the W mass due to radiative effects are predicted to be -65 MeV/c^2 and -168 MeV/c^2 for the electron and muon channels, respectively. Corrections of $+65$ MeV/c^2 and $+168$ MeV/c^2 are thus applied to the fitted W mass. Corresponding shifts on the W mass from fitting E_T^ℓ and E_T^ν are also studied. These results together with effects on the W width are listed in Table 8.3. For the muon channel the effect on $< u_{||} >$ from radiative decays is significant, $\sim +75$ MeV. The effect is included in the lineshape modeling.

Fit type	ΔM_W^e (MeV/c^2)	ΔM_W^μ (MeV/c^2)	$\Delta\Gamma_W^e$ (MeV)	$\Delta\Gamma_W^\mu$ (MeV)
M_T	$+65 \pm 20$	$+168 \pm 20$	–	–
E_T^ℓ	$+95 \pm 30$	$+240 \pm 32$	–	–
E_T^ν	-21 ± 30	$+45 \pm 30$	–	–
M_W,Γ_W floating	$+58 \pm 24$	$+176 \pm 30$	-65 ± 57	-36 ± 50

Table 8.3: Corrections to the W mass due to the effects of radiative decays. The corrections are shifts applied to the fitted W mass.

Uncertainties in the radiative effects on the W mass are estimated from uncertainties in the theoretical calculation and in the photon response. The Berends and Kleiss calculation does not include all the radiative Feynman diagrams. For example, it does not include initial state radiation (t- and u-channel diagrams). The effect of the missing diagrams is evaluated by using the Baur and Berger calculation [42], and is found to be ~ 20 MeV/c^2 on the W mass. The uncertainty in photon response, for photons well-separated from the W decay lepton, is evaluated by varying the photon energy threshold, the photon fiducial region, and the photon energy resolution. The effect is less than 5 MeV/c^2 on the W mass. The total uncertainty on the W mass due to radiative effects is 20 MeV/c^2, common to the electron and muon channels.

8.3 Summary

Backgrounds are directly included in the simulated lineshapes, with the exception of small backgrounds in the muon channel from $Z \to \tau\tau$ and jet or heavy-flavor production. The total effect of backgrounds on the measured W mass, if they had not been directly accounted for, would have been to shift the mass down by 60 MeV/c^2 in the electron channel and 197 MeV/c^2

in the muon channel. The uncertainties are 10 MeV/c^2 and 25 MeV/c^2 in the electron and muon channel, respectively, and are uncorrelated.

Radiative corrections are applied as a separate shift to the fitted value of the W mass and width (see Table 8.3). The shifts on the W mass from fitting the transverse mass spectra are -65 MeV/c^2 for the electron channel and -168 MeV/c^2 for the muon channel. The fitted W mass is shifted upwards by these amounts to compensate for the effects. The uncertainty on the W mass due to radiative effects is 20 MeV/c^2, common to the electron and muon measurements.

Section 9

FITTING

This section describes details of fitting the observed transverse mass to simulated lineshapes to extract the W mass. The section begins with a description of the transverse mass fitting procedure. Checks of the internal consistency of the fitting procedure follow. Checks of the results are also made using the data by varying the fit types and changing the sample. The fits from which the final W masses are extracted (the "ultimate fits")[1] are one-parameter fits to the transverse mass spectra of the $W \rightarrow e\nu$ and $W \rightarrow \mu\nu$ events with the W width constrained. An uncertainty due to the finite number of events simulated at each W mass is estimated. Log-likelihood contours for fits with the W width constrained and unconstrained are shown.

9.1 Fitting Procedure

This section describes the $W \rightarrow \ell\nu$ transverse mass fitting procedure in detail. The description also applies to the procedures used for fitting the di-electron and di-muon mass spectra, the E/p spectrum, and the individual-lepton E_T spectra. Transverse mass spectra are generated for W masses from

[1] **ultimate**, *adj.*, completing a series or process; final; conclusive.

79.6 GeV/c^2 to 81.0 GeV/c^2 at 100 MeV/c^2 intervals for the $W \rightarrow e\nu$ channel and 79.2 GeV/c^2 to 81.0 GeV/c^2 at 150 MeV/c^2 intervals for the $W \rightarrow \mu\nu$ channel, and for W widths from 1.9 GeV to 2.5 GeV at 200 MeV intervals. The range of transverse masses used in the fit is $65 < M_T^W < 100$ GeV/c^2. At each mass-width point, an unbinned log-likelihood is calculated for the hypothesis that the data are consistent with that mass and width. An uncertainty on each log-likelihood point is calculated from the finite statistics used to generate each lineshape. That is, the number of events in each bin of each lineshape contributes a statistical uncertainty to the log-likelihood. The log-likelihoods fit well to a paraboloid. The maximum of the paraboloid corresponds to the best values for the mass and width. The contour in the mass-width plane corresponding to a decrease of 0.5 in log-likelihood relative to the maximum defines the "one-sigma" confidence level. For the fixed-width fits the procedure is similar, except that the log-likelihoods are fit to a parabola.

9.2 Checks of Fitting Procedure

Any fitting procedure must satisfy at least two reliability criteria. First, when the procedure is applied to an ensemble of simulated experiments of the same sample size, the average returned value must be consistent with the mass used to generate the events. Second, the RMS spread of the fitted masses in these experiments must be consistent with the mean statistical uncertainty returned by the fits.

To check these criteria, artificial $W \rightarrow e\nu$ data samples of the same size as the real data are made at a known mass and width using the same simulation as used to make the lineshapes. Fitting to 225 such data samples, the average of the returned masses is seen to agree with the mass at which they were generated, and their RMS spread agrees with the mean statistical uncertainty. The returned widths must show similar agreement, which they

do. As a check of the constrained-width fits, the spread of returned masses for fits to artificial data generated with M_W=80.45 GeV/c^2 and Γ_W=2.064 GeV is shown in Figure 9.1. The mean returned mass, 80.458 $\pm$ 0.010 GeV/c^2, agrees with the value used to generate the data, 80.450 GeV/c^2. The RMS spread, 147 $\pm$ 7 MeV/c^2, agrees with the mean fitted uncertainty of 143 MeV/c^2. The distribution of fitted masses is well described by a Gaussian, and the fits of the log-likelihood points to parabolas are statistically consistent with $< \chi^2 >= 1.0$, justifying the assumption of Gaussian statistical uncertainties. Since each lineshape consists of several hundred thousand events, the fitted mass is expected to vary by less than 10 MeV/c^2 when fit to statistically independent templates. A scatter of this magnitude is seen when fitting the data to statistically independent lineshapes, and is taken as a systematic uncertainty due to fitting. Studies of the $W \rightarrow \mu\nu$ fits, Z mass fits, and the E/p lineshape fits show them to satisfy the reliability criteria.

9.3 Consistency Checks

The previous checks tested only the internal consistency of the fitting procedure. Other checks are made with the $W \rightarrow e\nu$ and $W \rightarrow \mu\nu$ data. The changes in the returned mass as the fit window on the transverse mass spectrum is varied are given in Tables 9.1 and 9.2. Only the transverse mass window is changed for these fits; the event selection is otherwise the same. In addition to checking the fitting procedure, these results check event modeling and background estimates. The observed mass shifts are consistent with the fluctuations expected from the change in the number of events as the fit window is changed.

Fits to the individual charged lepton and neutrino E_T spectra are more sensitive to systematic errors in the p_T^W and recoil modeling. The resulting mass shifts relative to the ultimate fits are summarized in Table 9.3. These

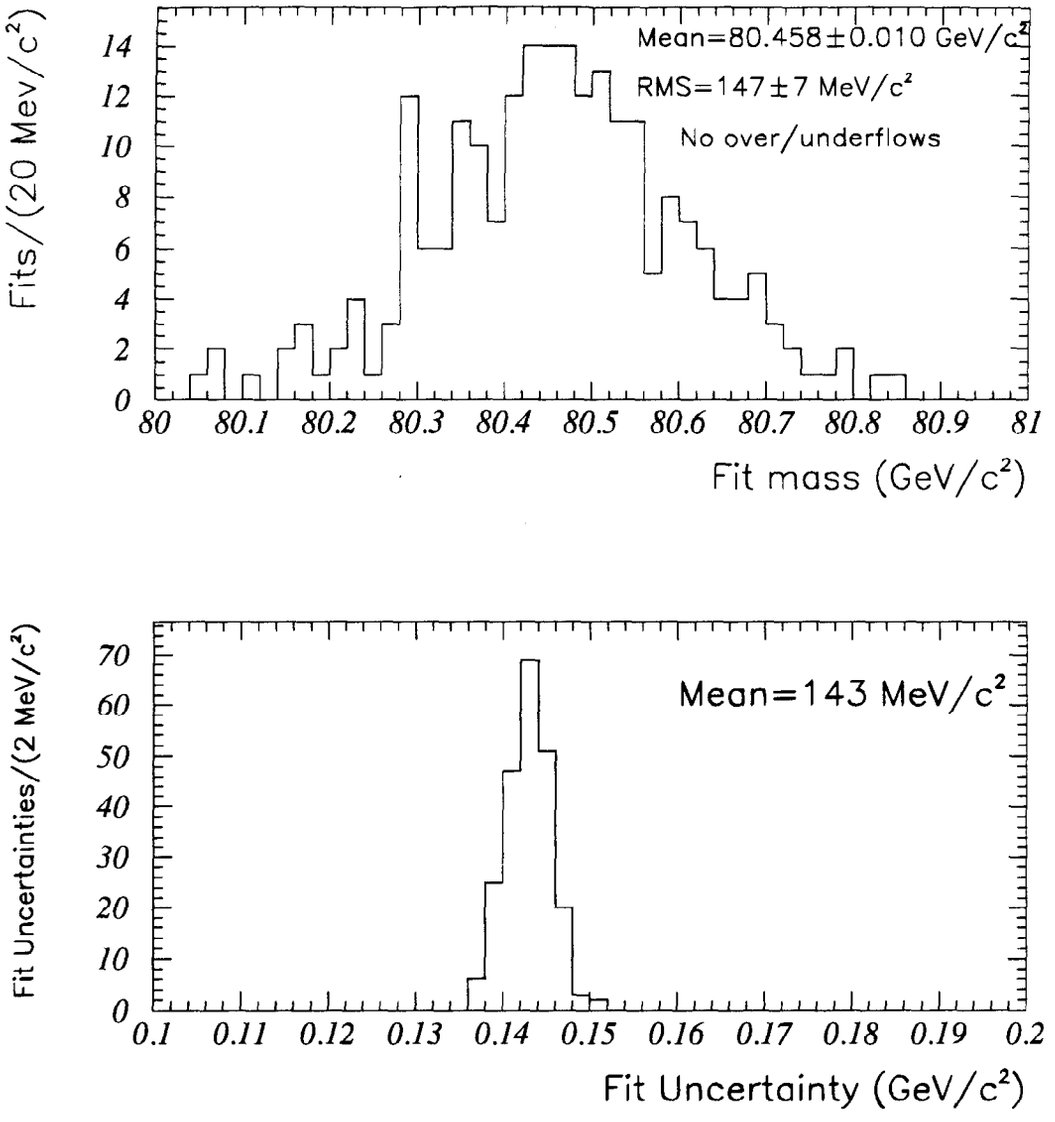

Figure 9.1: Upper: The distribution of returned masses for fixed-width fits to 225 artificial $W \rightarrow e\nu$ data samples generated at M_W=80.45 GeV/c^2. Lower: The distribution of returned statistical uncertainties in those fits. Studies with the $W \rightarrow \mu\nu$ lineshapes yield similar results.

M_T^W (min) (GeV/c^2)	ΔM_W^e (MeV/c^2)	ΔM_W^μ (MeV/c^2)
50	-55 ± 49	$+38 \pm 71$
55	-35 ± 48	$+47 \pm 76$
60	$+12 \pm 39$	$+47 \pm 60$
65	0	0
70	-44 ± 73	$+63 \pm 107$

Table 9.1: The difference in the returned fit relative to the ultimate fit as the lower cutoff in transverse mass for the fit is varied. The uncertainty is the independent statistical uncertainty estimated using the Monte Carlo.

M_T^W (max) (GeV/c^2)	ΔM_W^e (MeV/c^2)	ΔM_W^μ (MeV/c^2)
90	-65 ± 54	$+42 \pm 97$
95	-60 ± 19	-28 ± 49
100	0	0
105	-4 ± 9	$+37 \pm 43$
110	-4 ± 10	$+50 \pm 46$
120	0 ± 12	$+37 \pm 52$
150	$+2 \pm 14$	$+22 \pm 77$

Table 9.2: The difference in the returned fit relative to the ultimate fit as the upper cutoff in transverse mass for the fit is varied. The uncertainty is the independent statistical uncertainty estimated using the Monte Carlo.

Spectrum Fit	ΔM_W (MeV/c^2)
Electron E_T^e fit	-14 ± 132
Electron $\not\!\!E_T$ fit	$+70 \pm 138$
Muon p_T^μ fit	$+322 \pm 184$
Muon $\not\!\!E_T$ fit	-26 ± 143

Table 9.3: Shifts in the W mass as the fit type is changed from the transverse mass spectrum used in the ultimate fit to a fit of an individual-lepton spectrum. The shifts are assigned an uncertainty estimated from the Monte Carlo.

fits do not have a fit window imposed other than the overall requirement that $65 < M_T < 105$ GeV/c^2. The scatter is consistent with the estimates of the independent statistical uncertainty which is estimated using artificial experiments. Even larger deviations than indicated by the statistical estimate might be anticipated since systematic uncertainties increase for these fit types. In Figures 9.2 and 9.3, the lepton p_T spectra are compared to the Monte Carlo spectra predicted using the mass value returned from the ultimate fit.

Fits may be made to the samples split into low and high $|\mathbf{u}|$ regions to further test the event modeling. The subsets of the $W \rightarrow e\nu$ sample with $|\mathbf{u}| < 5$ GeV and $|\mathbf{u}| > 5$ GeV have 2770 and 2948 events in the fit range, respectively; the $W \rightarrow \mu\nu$ samples have 1504 and 1764 events. The results of these fits relative to the ultimate $W \rightarrow \ell\nu$ fits are shown in Table 9.4. Although the numbers are split about zero, the shifts are highly anti-correlated so the numbers can be interpreted as only a single check. Note that the splitting is consistent with what would be expected from the apparent statistical fluctuation in $< u_{\parallel} >$ and the modest disagreements in the RMS values of $u_{\parallel}$ and $u_{\perp}$ seen in Table 7.3. Moreover, the p_T spectrum given to the boson was not retuned for this study. The transverse mass spectrum for each of these samples for electrons and muons is shown along with the Monte Carlo spec-

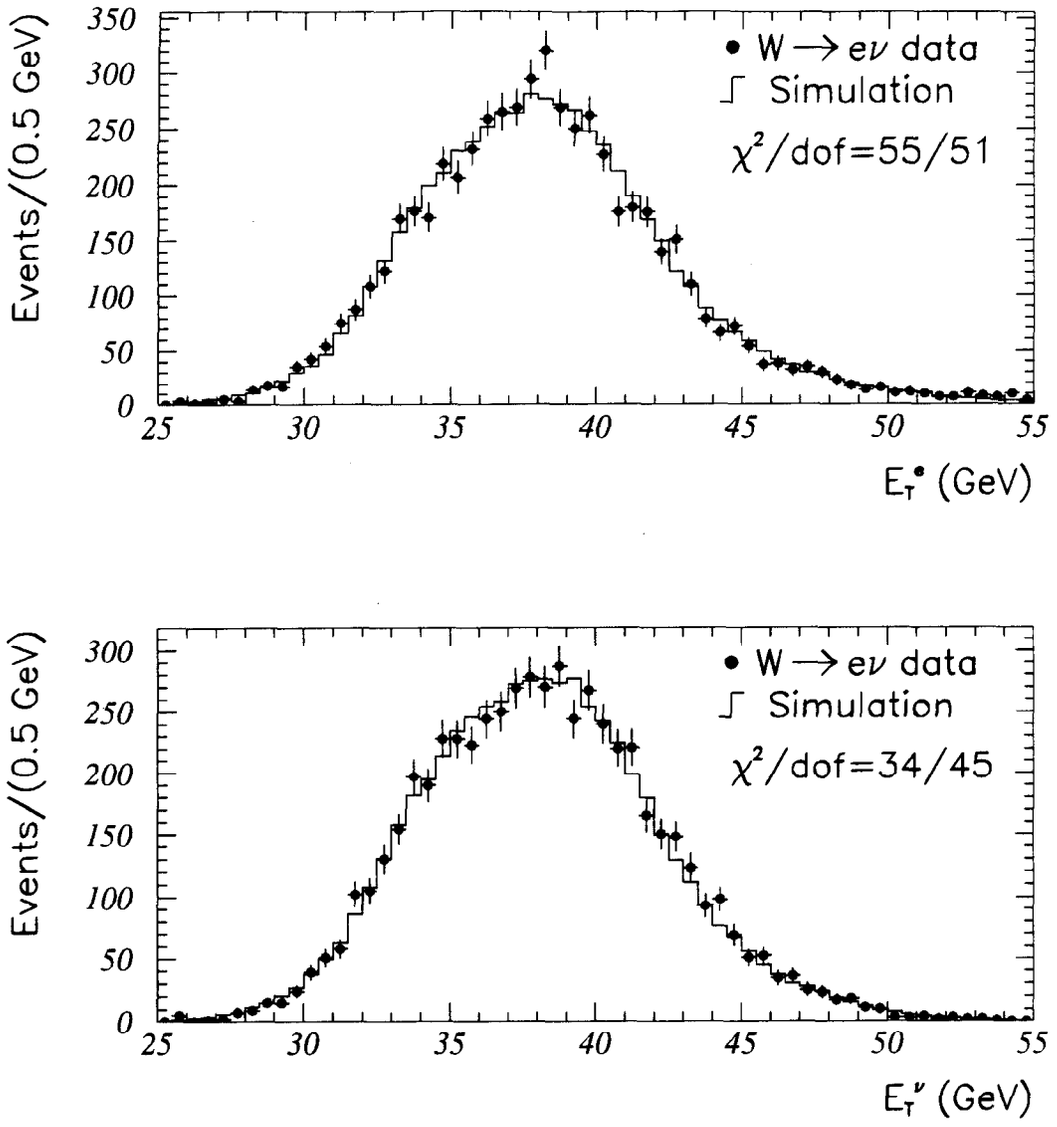

Figure 9.2: Upper: Electron E_T spectrum compared to simulation, for events that fall in the window $65 < M_T < 105$ GeV/c^2. Lower: Electron-neutrino E_T spectrum compared to simulation, for events that fall in the window $65 < M_T < 105$ GeV/c^2. Note that the mass value used for the simulation comes from a fit to the transverse mass, and not to the single-lepton spectrum shown.

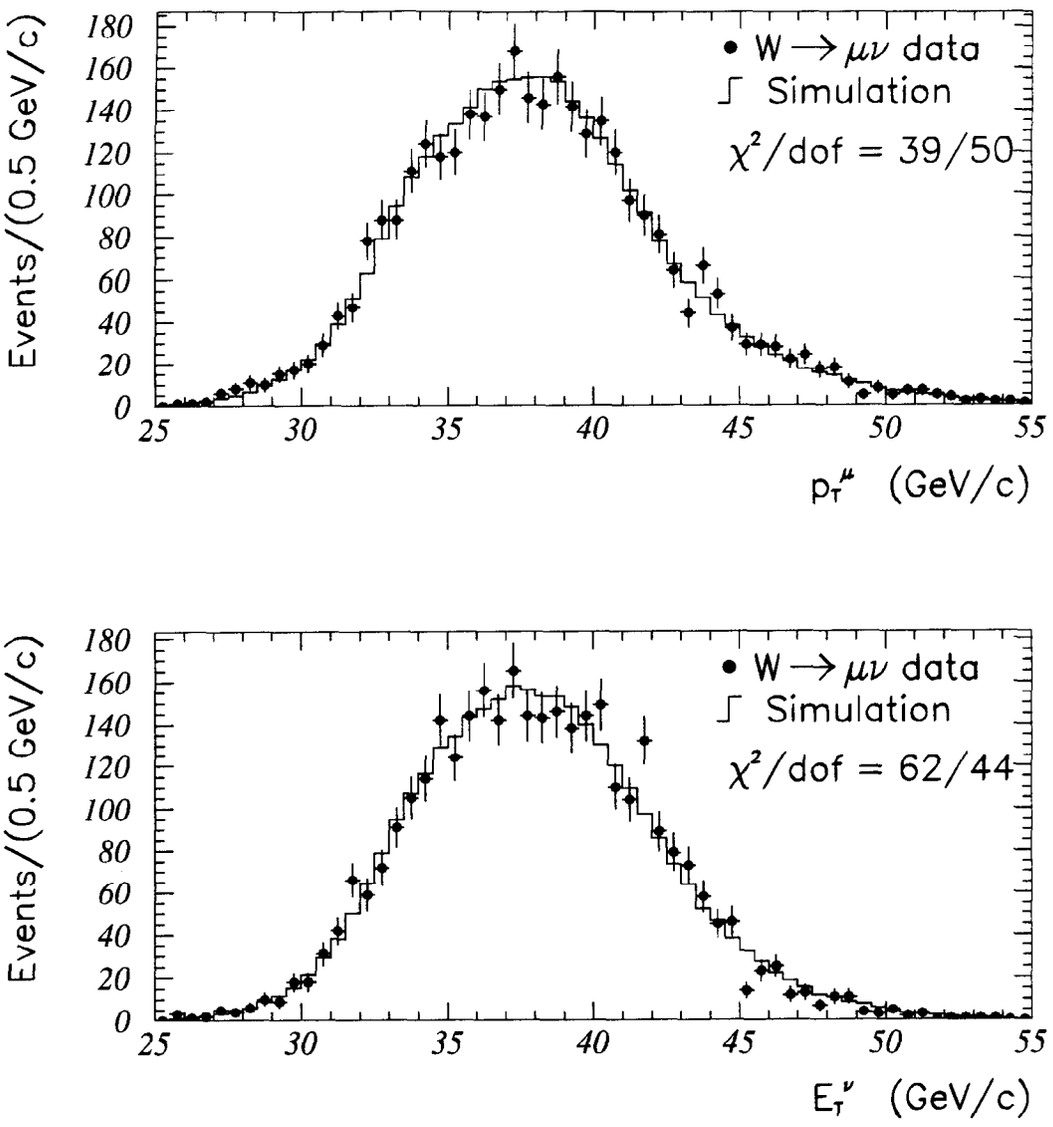

Figure 9.3: Upper: Muon p_T spectrum compared to simulation, for events that fall in the window $65 < M_T < 105$ GeV/c^2. Lower: Muon-neutrino p_T spectrum compared to simulation, for events that fall in the window $65 < M_T < 105$ GeV/c^2. Note that the mass value used for the simulation comes from a fit to the transverse mass, and not to the single-lepton spectrum shown.

Fit type	ΔM_W^e (MeV/c^2)	ΔM_W^μ (MeV/c^2)
$\|\mathbf{u}\| < 5$ GeV fit	$+200 \pm 180$	$+77 \pm 240$
$\|\mathbf{u}\| > 5$ GeV fit	-170 ± 200	-80 ± 270

Table 9.4: Shifts in the W mass as the fit type is changed from the ultimate fit to ones covering a different subset of $|\mathbf{u}|$. The shifts are assigned an uncertainty due to the independent statistical and systematic uncertainties as is done for other checks. The shifts for the two subsets are expected to be almost completely anti-correlated.

trum predicted using the mass from the ultimate fit in Figures 9.4 ($W \rightarrow e\nu$) and 9.5 ($W \rightarrow \mu\nu$).

Another check of systematics is the fitted W width and the shift in the fitted mass when the width is not constrained in the fit. The mass and width values are correlated because the shape of the transverse mass spectrum is asymmetric. Since the W width behaves as a resolution, the comparison of the measured W width with its expected value serves as a check on the modeling. The measured value for the width from the fit to the $W \rightarrow e\nu$ data, after applying the radiative correction in Table 8.3, is

$$\Gamma_W^e = 2.35 \pm 0.25(\text{stat.}) \pm 0.40(\text{syst.}) \text{ GeV}. \quad (9.1)$$

For the $W \rightarrow \mu\nu$ data, the measured number is,

$$\Gamma_W^\mu = 1.53 \pm 0.44(\text{stat.}) \pm 0.39(\text{syst.}) \text{ GeV}. \quad (9.2)$$

The systematic uncertainties on the widths are estimated in the same way as those on the mass. The width measurements are consistent with the indirectly measured value of 2.064 ± 0.085 GeV [43], the directly measured value of 2.040 ± 0.320 GeV [69], and the Standard Model prediction of 2.067 ± 0.021 GeV [70]. In the $W \rightarrow e\nu$ channel, the shift in the measured mass, when the width is unconstrained rather than fixed to its expected value, is -79 MeV/c^2. For the

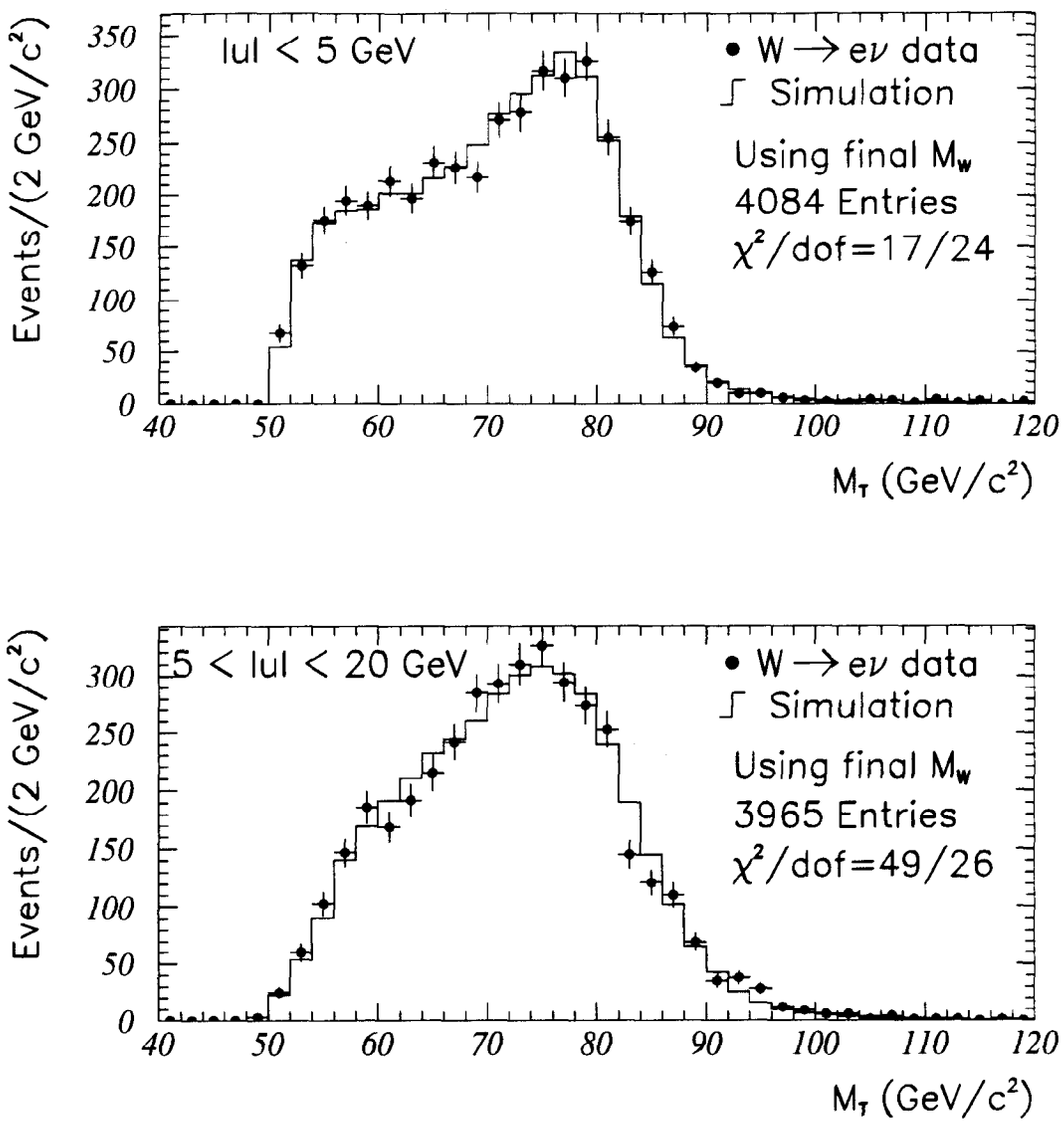

Figure 9.4: Transverse mass spectra of $W \rightarrow e\nu$ compared to the simulation using the mass value from the ultimate fit. Upper: $|\mathbf{u}| < 5$ GeV. Lower: 20 GeV$> |\mathbf{u}| > 5$ GeV. In each plot the two distributions being compared are normalized to equal area.

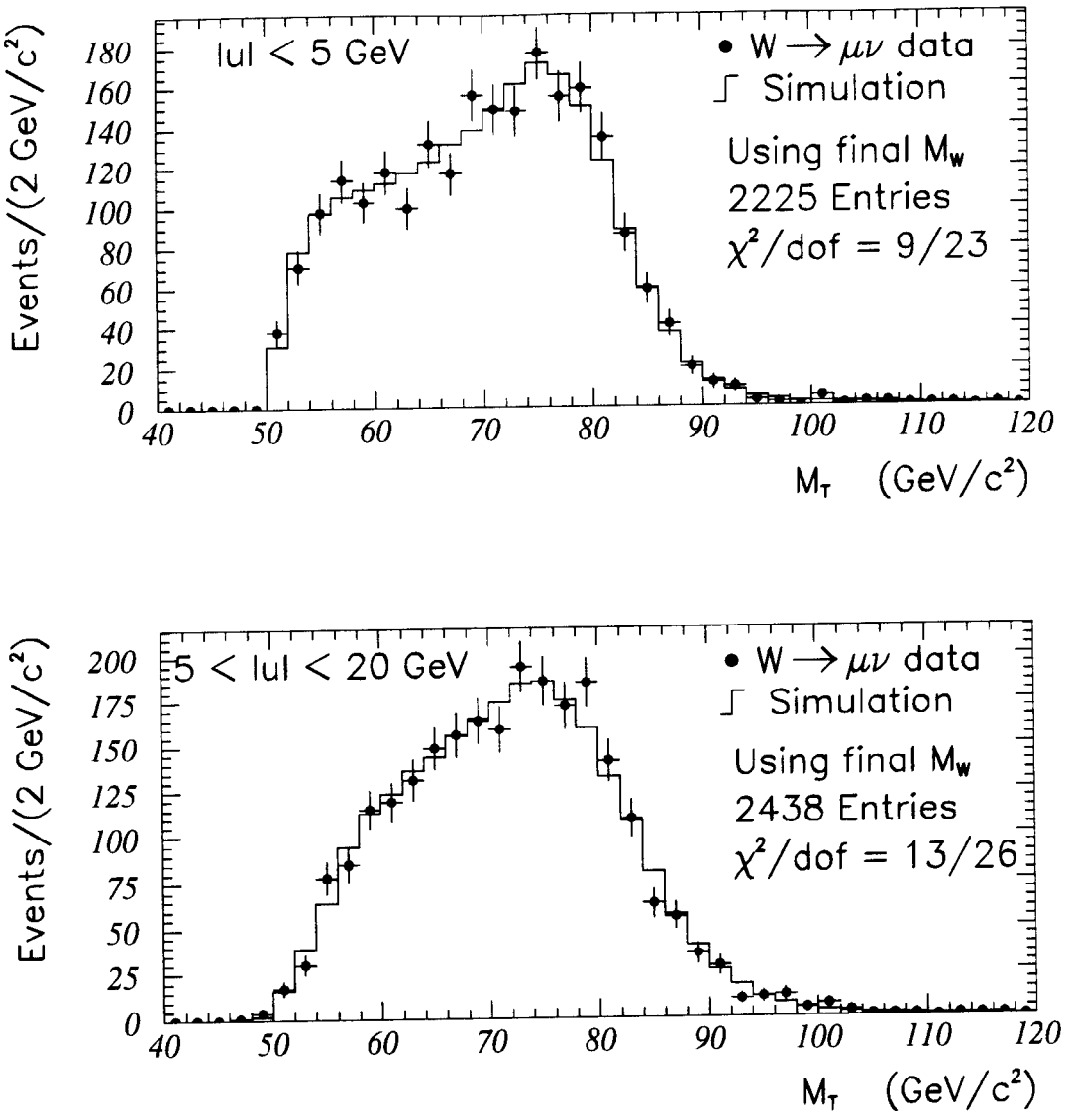

Figure 9.5: Transverse mass spectra of $W \rightarrow \mu\nu$ compared to the simulation using the mass value from the ultimate fit. Upper: $|\mathbf{u}| < 5$ GeV. Lower: 20 GeV$> |\mathbf{u}| > 5$ GeV. In each plot the two distributions being compared are normalized to equal area.

$W \rightarrow \mu\nu$ channel, the shift is $+123$ MeV/c^2. These are consistent with the fitted widths [71]. The log-likelihood contours for the fitted mass and width for the electron and muon fits are shown in Figures 9.6 and 9.7, respectively.

The W^+ and W^- are expected to have the same mass because of CPT conservation. Indirect tests comparing the decay rates of μ^+ and μ^- [72] are about two orders of magnitude more sensitive to this mass difference than the direct measurement presented here. For the $W \rightarrow e\nu$ measurement, since the electron energy measurements are charge-independent, the measurement of the mass difference is dominated by the statistical uncertainty. Dividing the sample by charge, there are 2826 W^+ events and 2892 W^- events. The measured mass difference from the $W \rightarrow e\nu$ data is

$$M(W^+) - M(W^-)\ \text{(electrons)} = +700 \pm 290\ \text{(stat.)}\ \text{MeV/c}^2, \qquad (9.3)$$

where the same energy scale is used for e^+ and e^-. Fits with the W width unconstrained show a similar mass splitting with no significant splitting between the measured widths. For the $W \rightarrow \mu\nu$ measurement, dividing the $W \rightarrow \mu\nu$ sample by charge yields 1644 W^+ and 1624 W^- events. The mass difference from the $W \rightarrow \mu\nu$ data is

$$M(W^+) - M(W^-)\ \text{(muons)} = +549 \pm 410\ \text{(stat.)} \pm 70\ \text{(syst.)}\ \text{MeV/c}^2, \quad (9.4)$$

where the systematic uncertainty is due to residual alignment effects in the CTC calibration. The combined result is

$$M(W^+) - M(W^-)\ \text{(combined)} = +625 \pm 240\ \text{MeV/c}^2, \qquad (9.5)$$

Extensive studies have been performed to see if this effect could be an artifact of the calibration procedure, or due to miscalibration of the energy scales for the gas calorimeters (the latter could give a difference due to the forward- backward asymmetry in W^+ and W^- production). No evidence is found for a systematic effect which could cause such a large mass splitting.

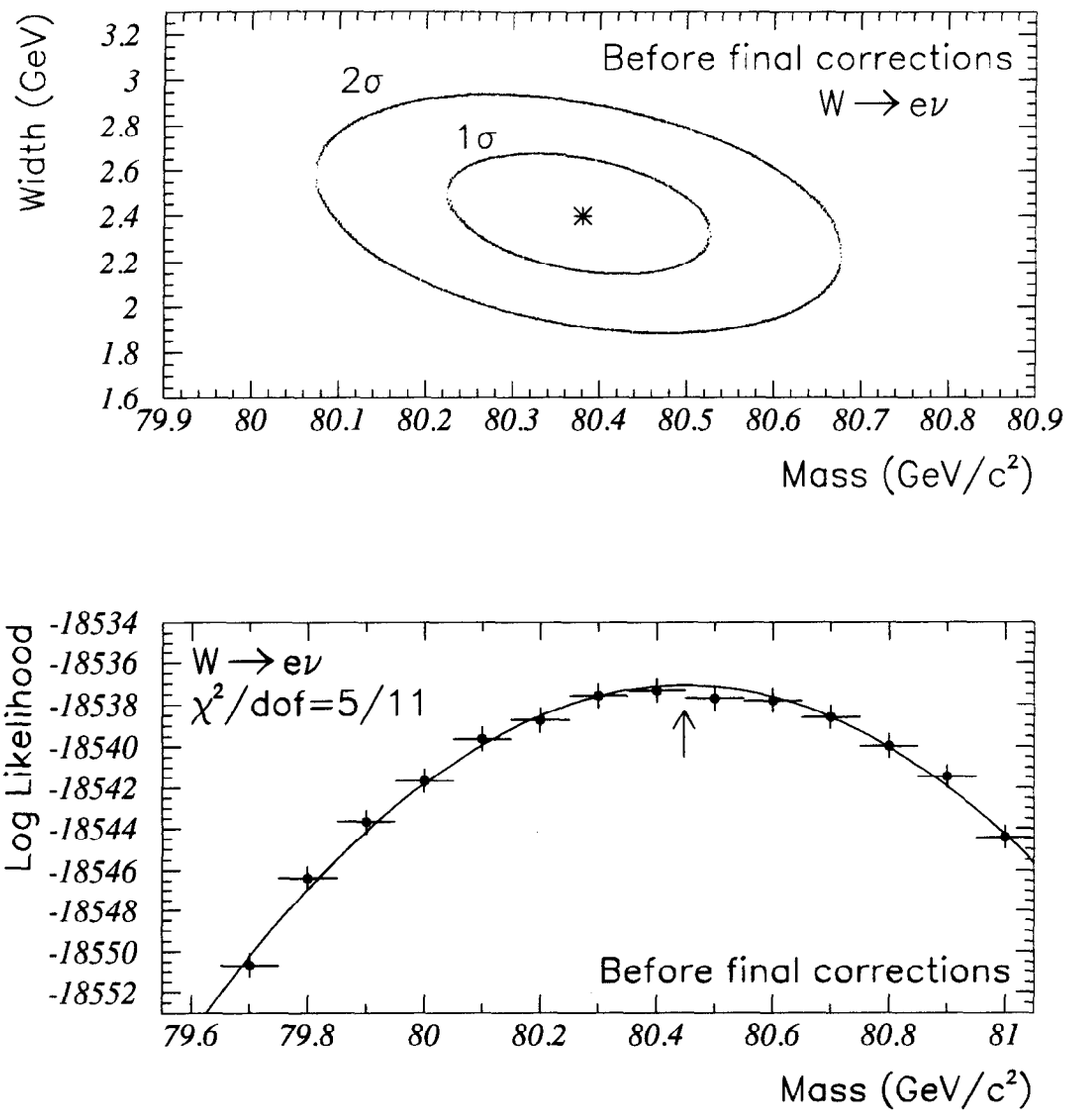

Figure 9.6: Upper: Log-likelihood contours for the simultaneous mass and width fit of the $W \rightarrow e\nu$ data. Lower: Log-likelihood points for the ultimate (fixed-width) fits. The arrow indicates the maximum likelihood.

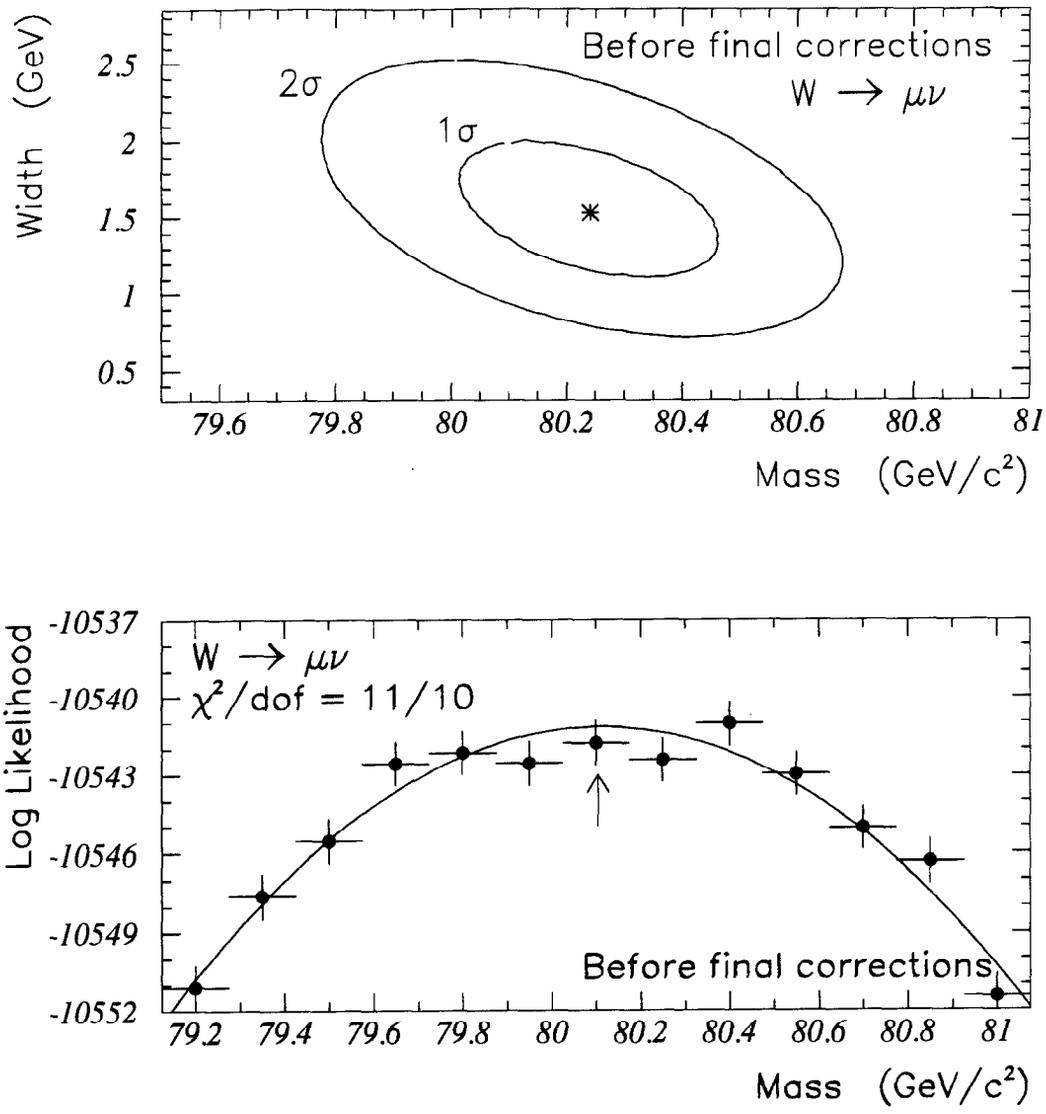

Figure 9.7: Upper: Log-likelihood contours for the simultaneous mass and width fit of the $W \rightarrow \mu\nu$ data. Lower: Log-likelihood points for the ultimate (fixed-width) fit. The arrow indicates the maximum likelihood.

9.4 Ultimate Fits

The ultimate fits to the electron and muon data, from which the quoted masses are taken, are fits to the transverse mass spectra of each data sample, where the W width has been constrained to its measured value of 2.064 ± 0.085 GeV. The log-likelihood points for the ultimate fit to the electron and muon transverse mass spectra are shown in Figures 9.6 and 9.7. A fit of a parabola to the points has $\chi^2/\mathrm{dof} = 5/11$ for the electron fit, and $\chi^2/\mathrm{dof} = 11/10$ for the muon fit. The transverse mass spectra of the $W \rightarrow e\nu$ and $W \rightarrow \mu\nu$ data, superimposed with the predictions using the mass returned from the ultimate fits, are shown in Figures 9.8 and 9.9. Radiative corrections of $+65 \pm 20$ MeV/c^2 for the electron channel and $+168 \pm 20$ MeV/c^2 for the muon channel are added to the fit values. A correction of $+20 \pm 10$ MeV/c^2 due to small backgrounds that are not included in the simulated lineshapes is also applied to the fit value for the muon channel.

The measured values of the W mass extracted from these fits are given in Section 10.2.

9.5 Summary

A 10 MeV/c^2 uncertainty on the W mass, independent in the electron and muon analyses, is taken due to the finite statistics used to generate the transverse mass lineshapes. Fits to the transverse mass spectra with the W width unconstrained yield values for the W width of $\Gamma_W^e = 2.35 \pm 0.25$ (stat.)$\pm$ 0.40 (syst.) GeV and $\Gamma_W^\mu = 1.53 \pm 0.44$ (stat.)$\pm$ 0.39 (syst.) GeV. The results of the ultimate fits are given in the following section.

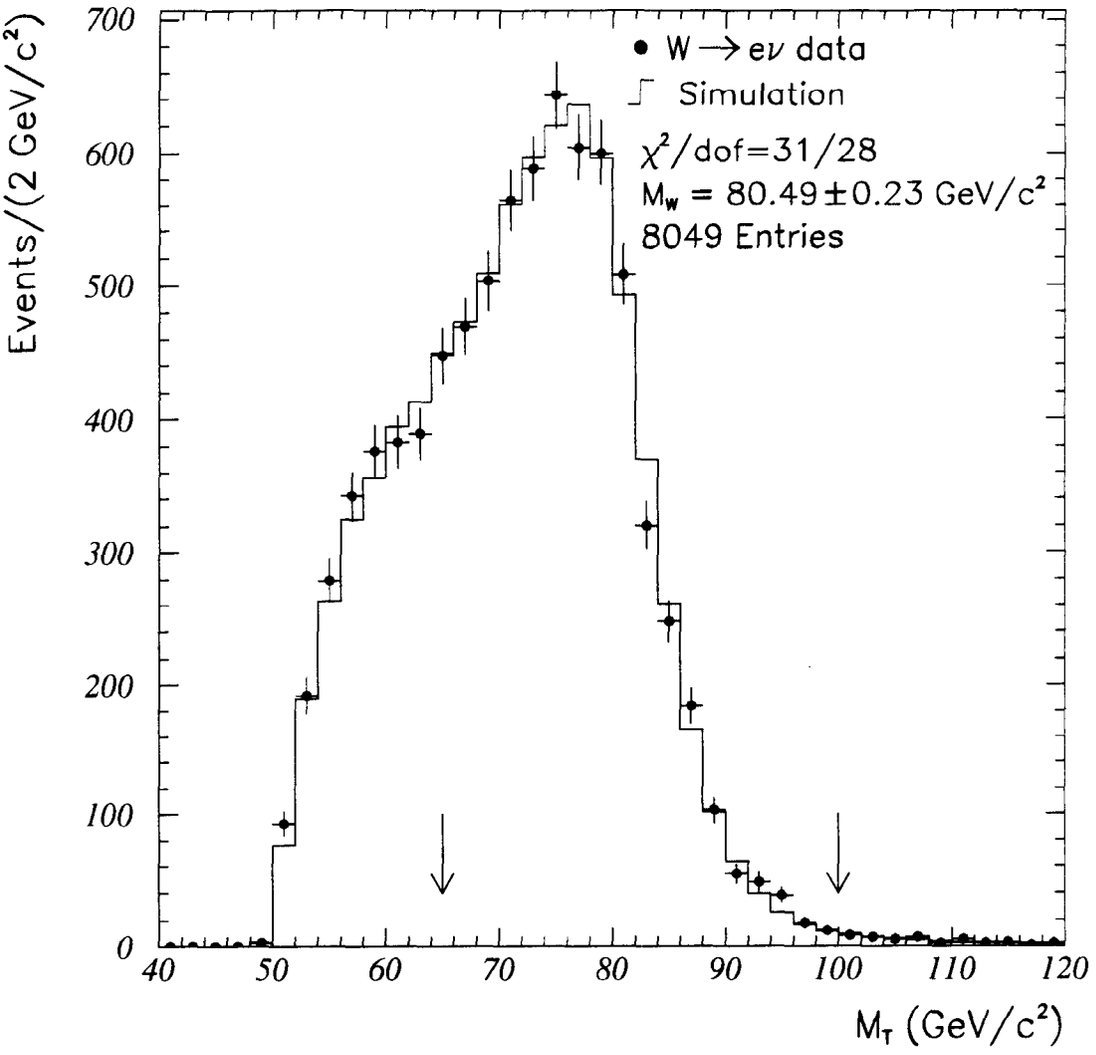

Figure 9.8: Comparison of the $W \rightarrow e\nu$ transverse mass spectrum for the data and simulation. The points are the data and the histogram is the simulation using the W mass value determined by the ultimate fit to the data. The arrows denote the limits of the window used for the ultimate fit.

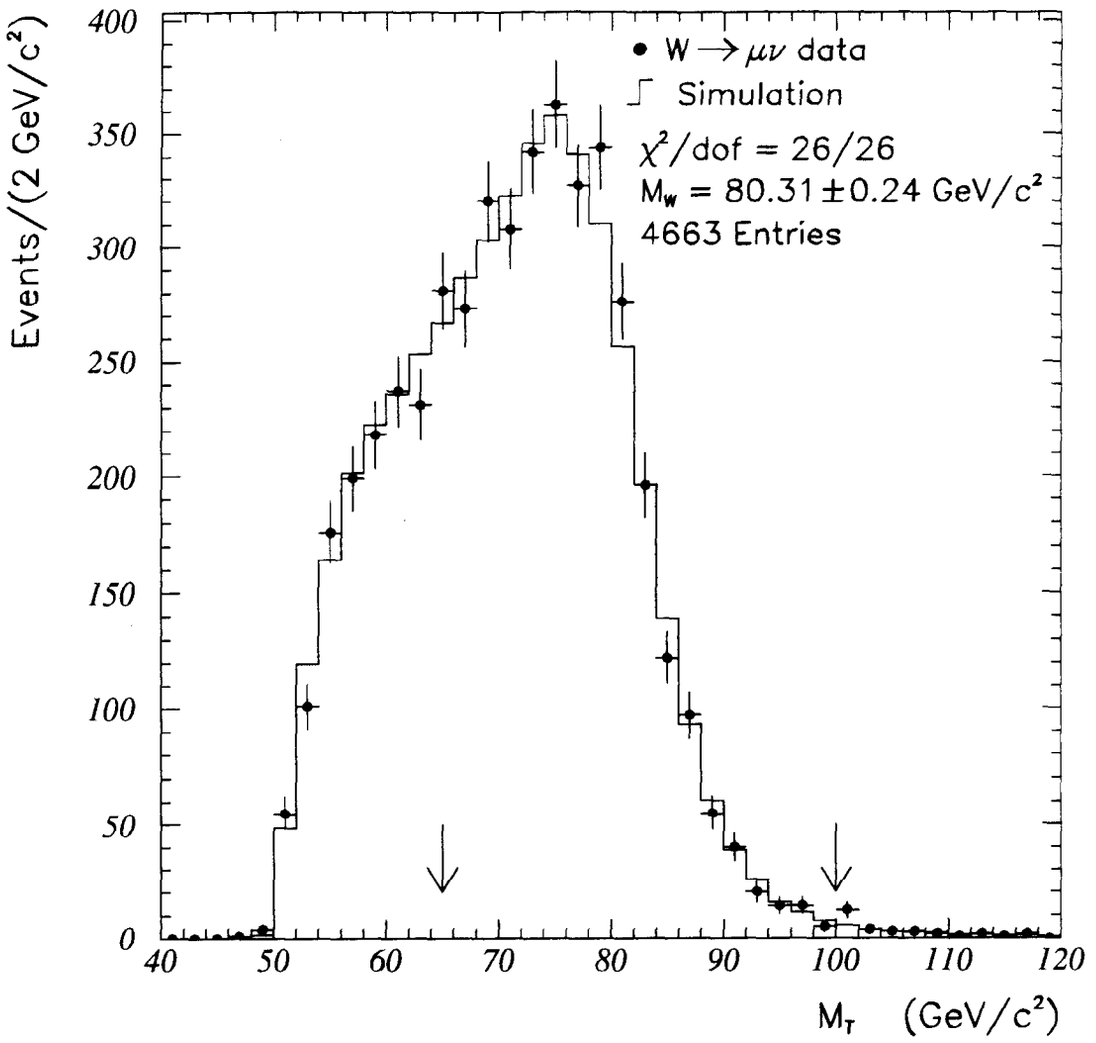

Figure 9.9: Comparison of the $W \rightarrow \mu\nu$ transverse mass spectrum for the data and simulation. The points are the data and the histogram is the simulation using the W mass value determined by the ultimate fit to the data. The arrows denote the limits of the window used for the ultimate fit.

Section 10

RESULTS

This section presents a summary of the measured values and experimental uncertainties in the W mass measurement. The results from the electron and muon channels are combined, accounting for correlated uncertainties. The new measurement is compared to previously published values as well as to predictions of the W mass based on global fits to electroweak measurements. The measurement, when combined with M_{top}, is compared to predictions in the M_W-M_{top} plane.

10.1 Summary of Systematic Uncertainties

A summary of the systematic errors on the W mass measurement discussed in this paper is given in Table 10.1.

All uncertainties have been rounded to the nearest 5 MeV/c^2. The statistical uncertainties are determined from the fits. The systematic uncertainty on the energy scale for electrons, 120 MeV/c^2, is dominated by the systematics of connecting the momentum scale to the electron energy scale. The 45 MeV/c^2 momentum scale uncertainty, included in this 120 MeV/c^2, is common to both the muon and electron channels. Other systematic un-

Uncertainty		ΔM_W^e (MeV/c^2)	ΔM_W^μ (MeV/c^2)	Common (MeV/c^2)
I.	Statistical	145	205	–
II.	Energy Scale	120	50	50
	1. Scale from J/ψ	50	50	50
	2. CTC Alignment	15	15	15
	3. Calorimeter	110	–	–
	a. Stat. on E/p	65		
	b. Syst. on E/p	90		
III.	Other Systematics	130	120	90
	1. e or μ resolution	80	60	–
	2. Input p_T^W	45	45	25
	3. Recoil modeling	60	60	60
	4. Parton distribution functions	50	50	50
	5. e or μ ID and removal	25	10	5
	6. Trigger bias	0	25	–
	7. Radiative corrections	20	20	20
	8. W width	20	20	20
	9. Higher-order corrections	20	20	20
	10. Backgrounds	10	25	–
	11. Fitting	10	10	–
TOTAL UNCERTAINTY		230	240	100

Table 10.1: Summary of uncertainties in the W mass measurement.

certainties due to modeling and event selection add up to 130 MeV/c^2 and 120 MeV/c^2 for the electron and muon analyses, respectively. The total common uncertainty is 100 MeV/c^2.

10.2 Masses

The mass extracted from the electron data is:

$$M_W^e = 80.490 \pm 0.145 \text{ (stat.)} \pm 0.175\text{(syst.)} \text{ GeV/c}^2. \quad (10.1)$$

The mass extracted from the muon data is:

$$M_W^\mu = 80.310 \pm 0.205 \text{ (stat.)} \pm 0.130\text{(syst.)} \text{ GeV/c}^2. \quad (10.2)$$

Accounting for correlations, the combined data yield a mass:

$$M_W = 80.410 \pm 0.180 \text{ GeV/c}^2. \quad (10.3)$$

This result is compared to previously published results (see Table 1.1) in Figure 10.1.

10.3 Experimental and Theoretical Context

A world-average value for the W boson mass is calculated by combining this measurement with the previous CDF [12] and UA2 [13] measurements. (see Figure 10.1). The value is

$$M_W^{\text{World}} = 80.33 \pm 0.17 \text{ GeV/c}^2. \quad (10.4)$$

The procedure used to calculate the average is: 1) Remove the uncertainty due to parton distribution functions (PDF), which is assumed to be (largely) common to the measurements; 2) combine the measurements weighted by their remaining respective uncertainties; and, 3) add back in the largest PDF

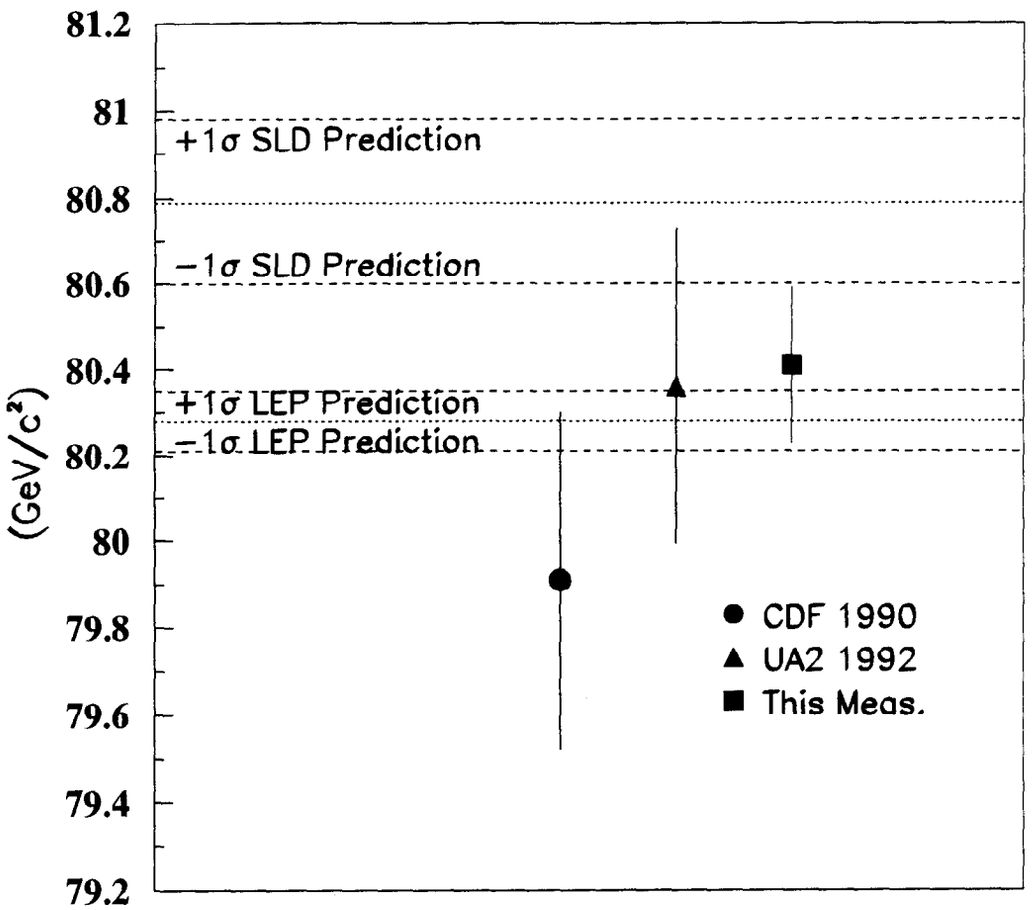

Figure 10.1: Previously published W masses and this measurement compared to the LEP and SLAC predictions.

uncertainty, which in this case is 85 MeV/c^2 [13]. The χ^2/d.o.f. of the three measurements to the world average is 0.69.

Values for the W mass can be inferred from measurements at the Z pole and from experiments measuring charged currents at low momentum transfer ($Q^2 \ll M_W^2$) under the assumption that there are no new phenomena outside of the Standard Model. Fits to properties of the Z measured at LEP [73] give a value $M_W^{\rm LEP} = 80.28 \pm 0.07$ GeV/c^2. The left-right asymmetry of the Z boson, measured at SLAC [74], is used to infer $M_W^{\rm SLAC} = 80.79 \pm 0.19$ GeV/c^2. Deep-inelastic neutrino scattering measurements are used to infer $M_W^{\rm DIS} = 80.24 \pm 0.25$ GeV/c^2 [61]. Figure 10.1 shows a comparison of the present values for the direct and indirect determinations of the W mass.

The direct measurement of the W boson mass can be combined with other electroweak data to yield a prediction for the top quark mass. One can also use a top quark mass to test the consistency of the Standard Model. Figure 10.2 shows a top quark mass of 176$\pm$13 GeV/c^2 [75] and the CDF W mass measurement presented in this paper. Also shown are theoretical predictions [76] of the regions in the M_W–M_{top} plane allowed in the Standard Model for different values of the mass of the Higgs boson. Note that the curves are sensitive to, among other things, the values of α and α_s at the Z pole [77].

10.4 Conclusion

A direct measurement of the W mass is one of the few measurements sensitive to the presence of new phenomena in the Standard Model of the electroweak interaction involving charged currents at high momentum transfer. A measurement of the W mass using both the electron and muon decay channels has been described. The mass is measured with the CDF detector,

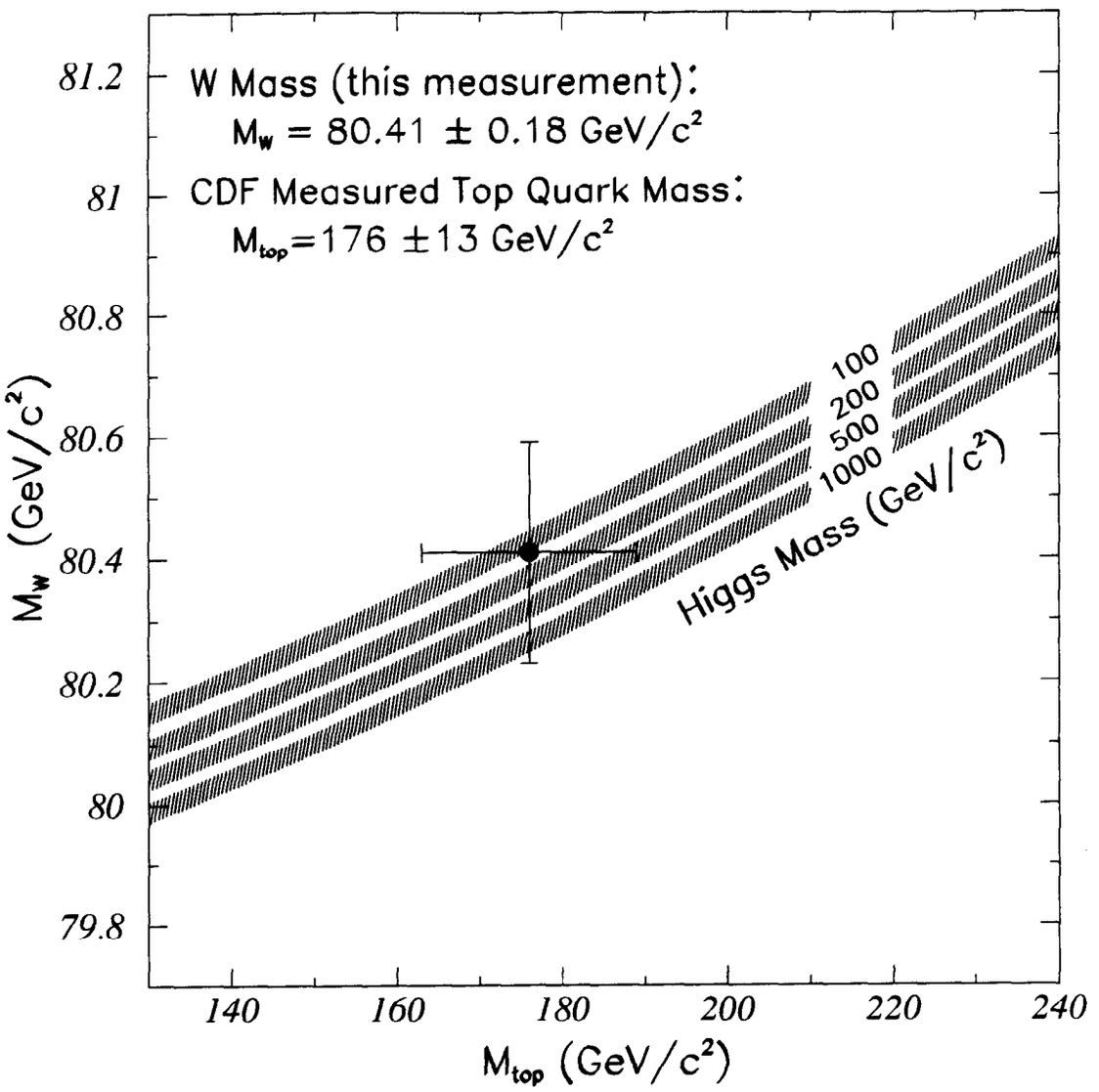

Figure 10.2: The data point represents the W mass measurement presented in this paper and a top quark mass of 176±13 GeV/c^2 [75]. The curves are from a calculation [76] of the dependence of the W boson mass on the top quark mass in the minimal Standard Model using several Higgs masses. The band on each curve is the uncertainty obtained by folding in quadrature uncertainties on $\alpha(M_Z^2)$, M_Z, and $\alpha_s(M_Z^2)$.

a combined magnetic spectrometer and calorimeter that allows many controls and checks of systematic effects, including the momentum and energy scales. This measurement, $M_W = 80.41 \pm 0.18$ GeV/c^2, has an uncertainty that is a factor of two smaller than any previously published direct measurement. The result indicates no deviation from the Standard Model.

We thank the Fermilab staff and the technical staffs of the participating institutions for their contributions. This work was supported by the U.S. Department of Energy and National Science Foundation; the Italian Istituto Nazionale di Fisica Nucleare; the Ministry of Science, Culture, and Education of Japan; the Natural Sciences and Engineering Research Council of Canada; the A. P. Sloan Foundation; and the Grainger Foundation.

Appendix A

COMMENT ON INNER MATERIAL

The energy scale for the calorimeter is set by matching the distribution of the energy to momentum ratio, E/p, for W-decay electrons to that for a radiative simulation. In the absence of bremsstrahlung, the calibration would be accomplished by setting the peak of the E/p distribution to unity. In the presence of internal and external bremsstrahlung, the true peak position is shifted slightly by soft photon radiation. This peak shift is correlated with the total amount of bremsstrahlung and hence with the high-side tail of the distribution, $1.3 < E/p < 2.0$. From a fit to the full E/p distribution, both the true peak position, which sets the energy scale, and the average amount of external material traversed by electrons are extracted. Since this method of determining the material thickness in radiation lengths (X_0) gives a value, $(8.9 \pm 0.9)\%$ X_0, that is significantly higher than the expected material count, 6.4% X_0, it is important to devise an independent check on the average material thickness. This is accomplished by measuring the production rates for e^+e^- conversion pairs, using the inner wall of the CTC as a known radiator.

The inner wall of the CTC is a cylinder at a radius of 28 cm, which

includes a Faraday cage for the VTX as well as structural support for the CTC. At normal incidence it consists of $(0.80 \pm 0.05)\%$ X_0 carbon fiber reinforced plastic, $(0.23 \pm 0.04)\%$ X_0 epoxy, 0.06% X_0 Kapton, 0.03% X_0 foamed lucite (Rohacell-31), 0.01% X_0 aluminum and 0.12% X_0 copper, for a total of $(1.26 \pm 0.06)\%$ X_0.

Conversion candidates are selected from the 9 GeV inclusive electron sample, using electron identification criteria similar to those used for the tower gain calibration. In addition, it is required that nearby partner tracks be reconstructed in the CTC that have small opening angles with respect to the trigger electrons. Conversion pair candidates are characterized by the r-ϕ separation between the two tracks at the conversion point, where the track helices are parallel, and by the polar opening angle, $|\Delta \cot\theta|$. A signal region is defined by requiring absolute separation less than 0.3 cm at the point of closest approach, and $|\Delta \cot\theta| < 0.03$. Non-conversion backgrounds are subtracted using a control region, defined by the same separation cut, but with $0.06 < |\Delta \cot\theta| < 0.15$. The shower maximum detector (CES) [20] is used to confirm the distributions in separation and $\Delta \cot\theta$ for true conversions and fake backgrounds. There are 209,000 signal candidates.

To optimize the resolution on the measured conversion radius, a two-constraint fit is applied to the helix parameters of the two tracks: the separation is constrained to vanish, and the angle ϕ from the beam spot to the conversion point is constrained to match the ϕ of the photon momentum vector. These constraints give an average observed resolution of 0.41 cm on the conversion radius, to be compared with an expected resolution of 0.35 cm. The radial distributions for conversions and backgrounds are shown in Figure A.1; the inner wall of the CTC is clearly visible. In estimating the number of conversions in the CTC inner wall itself, backgrounds from nearby SVX cables (see Figure A.2 *a*) and *b*)) are reduced by appropriate azimuthal cuts. The efficiency of the azimuthal cuts is not strictly geometrical, due to the

shadowing caused by ϕ cracks in the calorimeter, as illustrated in Figure A.2 c). The background-subtracted number of conversions in the CTC inner wall is 39900±975, or $(317 \pm 2 \pm 7 \pm 15) \times 10^4$ conversions per radiation length, where the three uncertainties are due to statistics, backgrounds, and uncertainty in the thickness of the CTC inner wall, respectively.

A check on this result is provided by the inner guard wires of the first super-layer in the CTC, as shown in Figure A.3. These wires are 153 μm- and 127 μm-radius stainless steel, corresponding to 0.045% X_0. The wires and the CTC inner wall are close in radius so the conversions from the two regions are expected to be reconstructed with the same efficiency. The distributions of conversions from the inner guard wires and from the other wires in the first super-layer are compared with a Monte Carlo simulation that includes resolution effects and background from conversions in the argon-ethane gas. After efficiency corrections (see below), the number of conversions in the inner guard wires is 1378±52, or $(305 \pm 12) \times 10^4$ conversions per radiation length, in good agreement with the CTC inner wall calibration.

A second check is provided by counting Dalitz pairs and conversions in the 500μm beryllium beampipe, selecting pairs with r <6 cm from the beam axis. To eliminate backgrounds from conversions in the SVX material, an event vertex requirement ($|z_{vertex}| > 35$ cm) is imposed. The efficiency for counting Dalitz pairs depends on the conversion-photon production mechanism, and in particular the relative production rates of e^+e^- pairs from π^0 and η decays and internal conversions of prompt photons; each of these contributions is expected to have a broader opening angle distribution and therefore, a lower efficiency, compared with external conversions. The number of Dalitz pairs plus beampipe conversions near the origin is 2246±130, where the uncertainty includes uncertainties on the production mechanisms, the radial dependence of the reconstruction efficiency, and the beampipe thickness. Using measured Dalitz decay rates to define an equivalent radiator, this implies $(313 \pm 20) \times 10^4$

pairs per radiation length, again consistent with the CTC inner wall calibration.

To measure the average material traversed by electrons, the total conversion rates are compared with those in the CTC inner wall; this requires a determination of the relative efficiency for detecting conversions as a function of radius. The main source of this efficiency dependence is bias in the electron trigger. When both the trigger electron and partner positron point to the same calorimeter cell, the trigger efficiency is increased because of the enhanced energy deposition. The geometrical probability for both tracks to point to the same cell increases with radius, causing the overall conversion efficiency to grow with radius; the increase is about 10% in going from the origin to the CTC inner wall. This radial dependence is measured directly from the data by transplanting conversion pairs from small to large radius, and comparing their p_T spectra with those observed at large radius. This efficiency correction is included in the Dalitz-pair calibration described above.

Subtracting non-conversion backgrounds and Dalitz pairs, correcting for relative efficiencies, and averaging over event vertex position and θ, the amount of material traversed inside a radius of 31 cm by an electron from $W \rightarrow e\nu$ decay is determined to be $(7.1 \pm 0.1 \pm 0.4)\%\ X_0$, where the first uncertainty is statistical and the second is systematic, dominated by uncertainty in the thickness of the CTC inner wall. Adding in CTC gas and wire material between a 31 cm radius and the center of the CTC, the total predicted material is $(8.1 \pm 0.4)\%\ X_0$. This compares well with the $(8.9 \pm 0.9)\%\ X_0$ value derived from the fit to the E/p distribution, and confirms the discrepancy with the 6.4% X_0 estimate based on the direct accounting of the material.

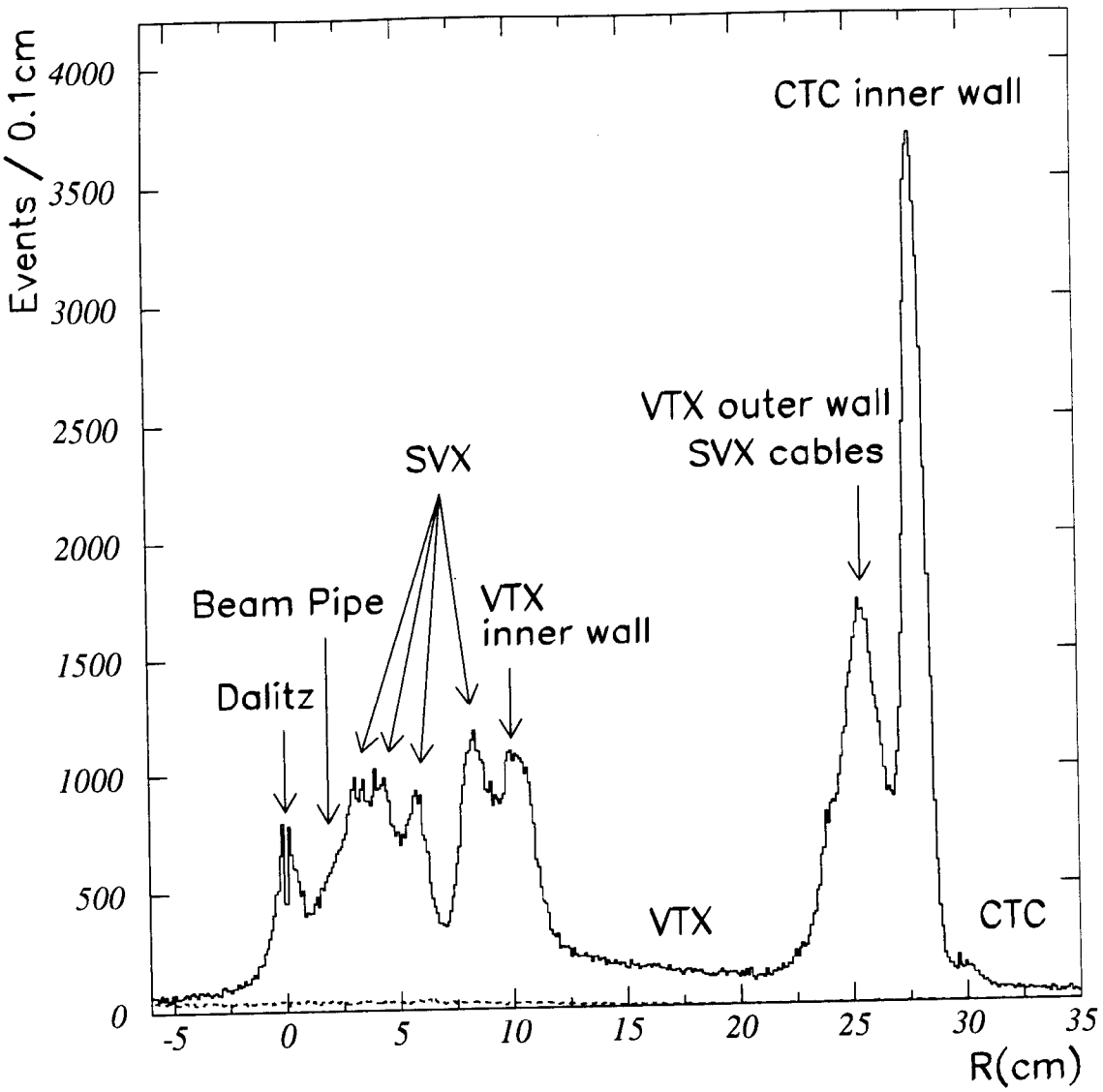

Figure A.1: The radial distributions for conversions (solid line) and background (dashed line). The radial positions of the various sources of conversions are also shown.

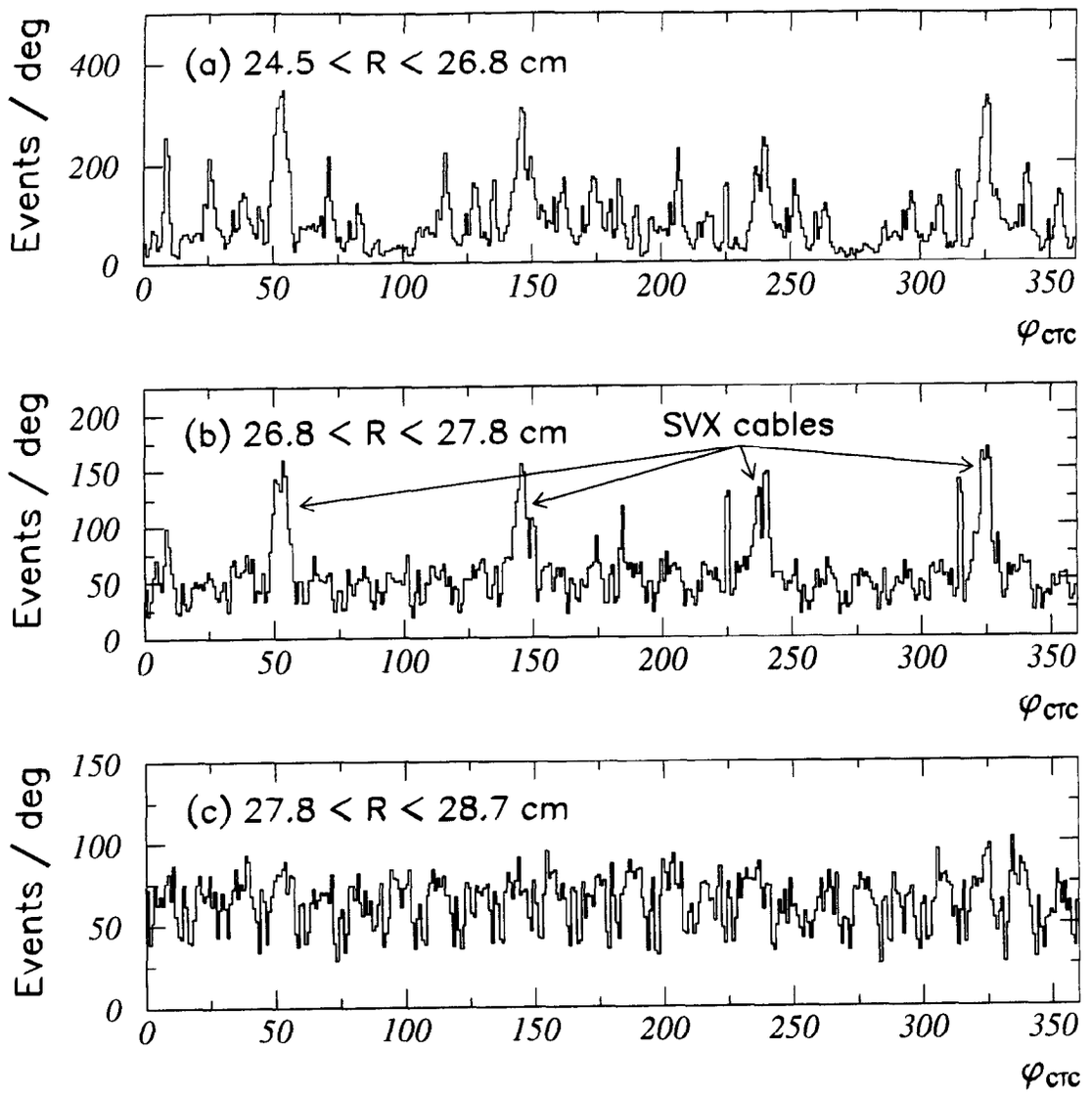

Figure A.2: The ϕ distribution of conversions for (a) $24.5 < R_{\text{conversion}} < 26.8$, (b) $26.8 < R_{\text{conversion}} < 27.8$, and (c) $27.8 < R_{\text{conversion}} < 28.7$.

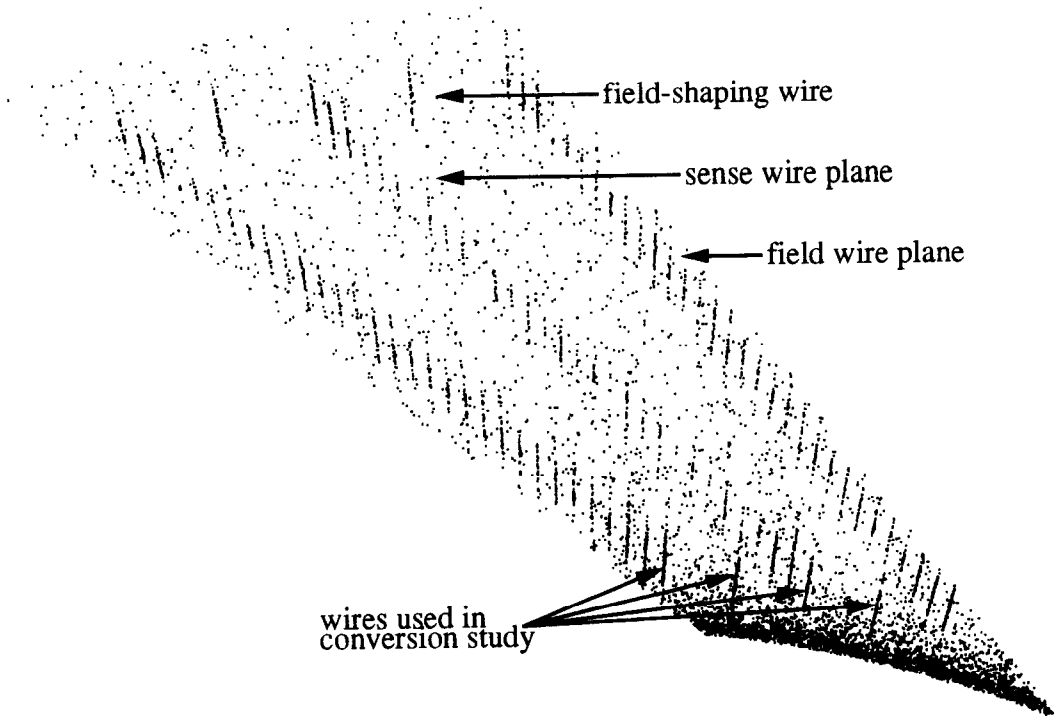

Figure A.3: Reconstructed photon conversion vertex density in the r-ϕ plane for the innermost super-layer in the CTC, folded into 1/30 of the circumference (this layer has 30-fold symmetry). Each point represents one reconstructed vertex.

Appendix B

COMMENT ON CHECKS

Many checks of the model and results have been made in this paper. Of these, 28 have been identified as significant and independent and are listed in Table B.1. The root mean squared standard deviation from zero is 0.98 ± 0.13, in good agreement with the expected value of 1.0. There are 20 entries with standard deviation less than 1.0, where one would expect 19.1. There are 6 entries between 1.0 and 2.0 where one would expect 7.6. There are 2 entries between 2.0 and 3.0 where one would expect 1.2. There are no entries above 3.0 where one would expect 0.1.

Check	Standard deviations
Υ(1S) mass	0.04
Υ(2S) mass	0.81
Υ(3S) mass	2.26
$Z \rightarrow \mu\mu$ mass	0.67
Tracking resolution	0.00
$Z \rightarrow ee$ mass	1.14
Material measurement	0.81
$< u_{\|\|} >$ offset for $W \rightarrow e\nu$	0.12
$< u_{\|\|} >$ offset for $W \rightarrow \mu\nu$	1.34
RMS ($u_{\|\|}$) for $W \rightarrow e\nu$	0.43
RMS ($u_{\|\|}$) for $W \rightarrow \mu\nu$	1.00
Γ_W^e	0.61
Γ_W^μ	0.91
E_T^e fit	0.06
E_T^ν ($W \rightarrow e\nu$) fit	0.93
p_T^μ fit	1.35
E_T^ν ($W \rightarrow \mu\nu$) fit	0.67
$M_T^{\min} = 50$ GeV/c^2 ($W \rightarrow e\nu$)	1.12
$M_T^{\min} = 70$ GeV/c^2 ($W \rightarrow e\nu$)	0.60
$M_T^{\max} = 90$ GeV/c^2 ($W \rightarrow e\nu$)	1.20
$M_T^{\max} = 150$ GeV/c^2 ($W \rightarrow e\nu$)	0.14
$M_T^{\min} = 50$ GeV/c^2 ($W \rightarrow \mu\nu$)	0.53
$M_T^{\min} = 70$ GeV/c^2 ($W \rightarrow \mu\nu$)	0.59
$M_T^{\max} = 90$ GeV/c^2 ($W \rightarrow \mu\nu$)	0.43
$M_T^{\max} = 150$ GeV/c^2 ($W \rightarrow \mu\nu$)	0.29
$\|\mathbf{u}\| < 5$ GeV ($W \rightarrow e\nu$)	0.90
$\|\mathbf{u}\| < 5$ GeV ($W \rightarrow \mu\nu$)	0.32
CPT-test (e and μ)	2.60
Root mean-squared deviation from zero	0.98 ± 0.13

Table B.1: List of 28 of the checks made in this paper.

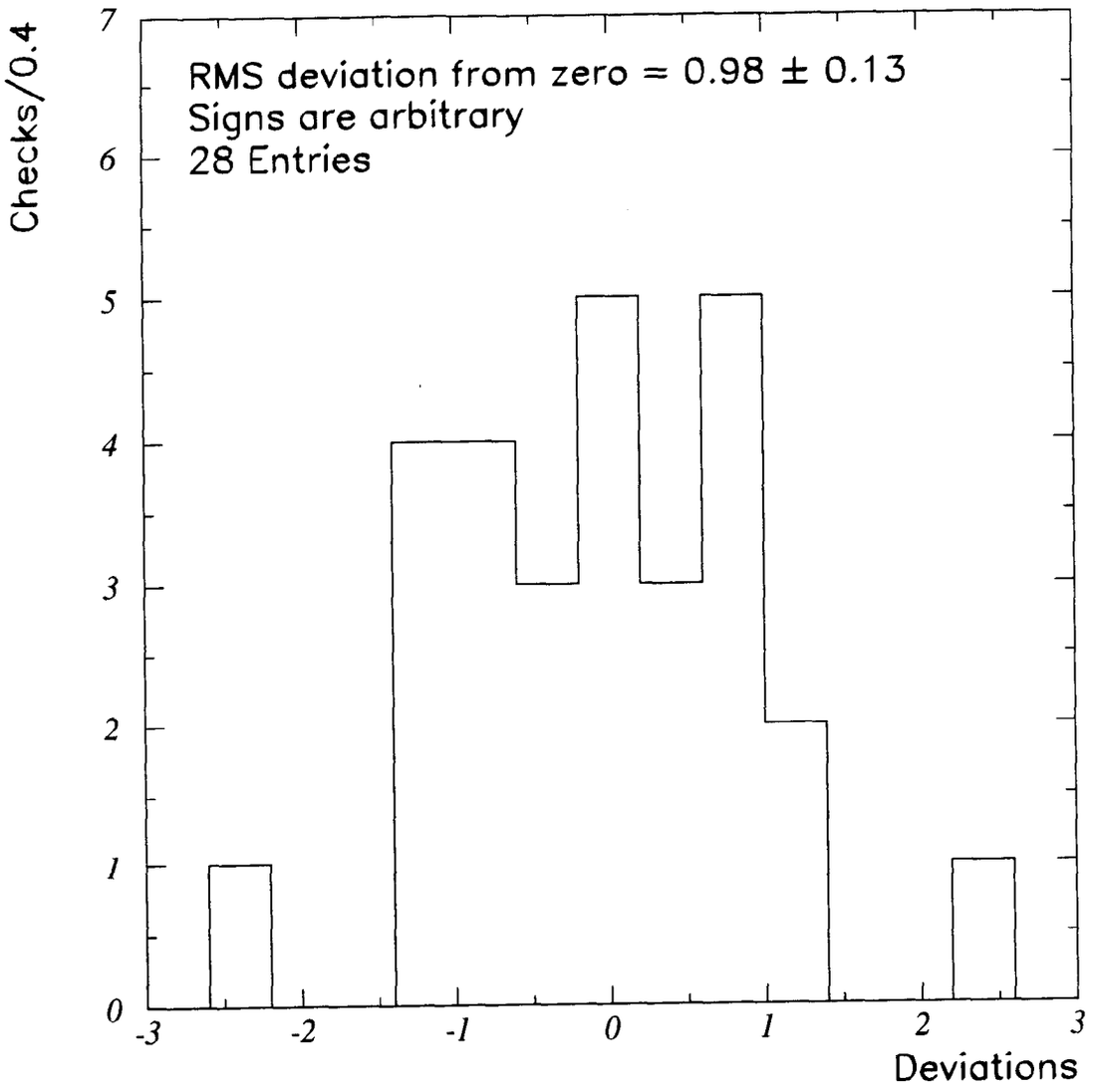

Figure B.1: Standard deviations of 28 of the checks made in this analysis.

REFERENCES

[1] S. L. Glashow, Nucl. Phys., **22**, 579 (1961); S. Weinberg, Phys. Rev. Lett., **19**, 1264 (1967); A. Salam, *Proceedings of the Eighth Nobel Symposium*, edited by N. Svartholm (Almqvist and Wiksells, Stockholm, Wiley, New York, 1968), p. 367.

[2] For recent reviews, see W. Hollik and W. Marciano, in "Precision Tests of the Standard Electroweak Model", ed. by P. Langacker (World Scientific, Singapore, 1994), and B. A. Kniehl, KEK preprint KEK-TH-412, Sept. 1994, submitted to Int. J. Mod. Phys. A.

[3] J. L. Rosner, Rev. Mod. Phys., **64**, 1151 (1992); erratum, *ibid.*, **66**, 1117 (1994).

[4] G. Arnison *et al.* (UA1 Collaboration), Phys. Lett., **B122** 103, (1983).

[5] M. Banner *et al.* (UA2 Collaboration), Phys. Lett., **B122** 476, (1983).

[6] G. Arnison *et al.* (UA1 Collaboration), Phys. Lett., **B134**, 469 (1984).

[7] G. Arnison *et al.* (UA1 Collaboration), Europhys. Lett., **1**, 327 (1986).

[8] R. Ansari *et al.* (UA2 Collaboration), Phys. Lett., **B186**, 440 (1987).

[9] C. Albajar *et al.* (UA1 Collaboration), Z. Phys., **C44**, 15 (1989).

[10] F. Abe *et al.* (CDF Collaboration), Phys. Rev. Lett., **62**, 1005 (1989).

[11] J. Alitti *et al.* (UA2 Collaboration), Phys. Lett., **B241**, 150 (1990).

[12] F. Abe *et al.* (CDF Collaboration), Phys. Rev. Lett., **65**, 2243 (1990); F. Abe *et al.* (CDF Collaboration), Phys. Rev., **D43**, 2070 (1991).

[13] J. Alitti *et al.* (UA2 Collaboration), Phys. Lett. **B276**, 354 (1992).

[14] L. M. Lederman and B. G. Pope, Phys. Rev. Lett. **27**, 316 (1971); R.B. Palmer, E. A. Paschos, N. P. Samios, and L.-L. Wang, Phys. Rev. **D14**, 118 (1976); C. Quigg, Rev. Mod. Phys. **49**, 297 (1977);G. Altarelli, K. Ellis, M. Greco, and G. Martinelli, Nucl. Phys. **B**246, 12 (1984); G. Altarelli, K. Ellis, and G. Martinelli, Z. Phys. C**27**, 617 (1985);Arnold and Kaufman, Nucl. Phys., **B349**, 381 (1991); A.D. Martin, W.J. Stirling, and R.G. Roberts, preprint RAL-94-104, Sept. 1994.

[15] F. Abe *et al.* (CDF Collaboration), Nucl. Instrum. Methods, **A271**, 387 (1988).

[16] F. Abe *et al.* (CDF Collaboration), Phys. Rev., **D50**, 2966 (1994).

[17] D. Amidei *et al.*, Nucl. Instrum. and Methods, **A350**, 73 (1994).

[18] F. Snider *et al.*, Nucl. Instrum. Methods, **A268**, 75 (1988). This is the reference for the previous generation of the device. The replacement for the 1992-93 data-taking period has more modules, each with a shorter drift length, but is otherwise similar.

[19] F. Bedeschi *et al.*, Nucl. Instrum. Methods, **A268**, 50 (1988).

[20] L. Balka *et al.*, Nucl. Instrum. Methods, **A267**, 272 (1988); S. R. Hahn *et al.*, Nucl. Instrum. Methods, **A267**, 351 (1988); K. Yasuoka *et al.*, Nucl. Instrum. Methods, **A267**, 315 (1988); R. G. Wagner *et al.*, Nucl. Instrum. Methods, **A267**, 330 (1988); T. Devlin *et al.*, Nucl. Instrum. Methods, **A267**, 24 (1988).

[21] S. Bertolucci *et al.*, Nucl. Instrum. Methods, **A267**, 301 (1988).

[22] Y. Fukui *et al.*, Nucl. Instrum. Methods, **A267**, 280 (1988); W. C. Carithers *et al.*, "Proceedings of the Gas Sampling Calorimetry Workshop II," Batavia, Illinois, 54 (1985). S. Cihangir *et al.*, Nucl. Instrum. Methods, **A267**, 249 (1988); G. Brandenburg *et al.*, Nucl. Instrum. Methods, **A267**, 257 (1988). The missing E_T calculation uses the calorimeters inside the range $|\eta| < 3.6$.

[23] G. Ascoli *et al.*, Nucl. Instrum. Methods, **A268**, 33 (1988); G. Ascoli *et al.*, Nucl. Instrum. Methods, **A268**, 41 (1988).

[24] D. Amidei *et al.*, Nucl. Instrum. Methods, **A269**, 51 (1988).

[25] T. Carroll *et al.*, Nucl. Instrum. Methods, **A263**, 199 (1988).

[26] G. W. Foster *et al.*, Nucl. Instrum. Methods, **A269**, 93 (1988).

[27] This is a superset of the 19.3 pb^{-1} used in some other CDF analyses (for example, Reference [16]), which exclude 0.4 pb^{-1} of data in which some (small) part of the muon system was inoperative.

[28] See F. Abe *et al.* (CDF Collaboration), Phys. Rev. Lett. **63**, 720 (1989), for an explicit demonstration.

[29] F. Abe *et al.* (CDF Collaboration), Phys. Rev. Lett. **74**, 850 (1995).

[30] The magnetic field map has been corrected upwards by a factor of 1.00070 ± 0.00021 from the original mapping, where this factor is from the recent NMR measurement.

[31] A run is a period of contiguous data-taking typically less than a day.

[32] See Reference [29] above. The forward/backward charge asymmetry in W decays is defined as: $A(\eta) = \frac{(d\sigma^+/d\eta)-(d\sigma^-/d\eta)}{(d\sigma^+/d\eta)+(d\sigma^-/d\eta)}$, where $d\sigma^{\pm}/d\eta$ is the cross section for $W^{\pm}$ decays as a function of lepton pseudorapidity, η.

[33] In many plots in this paper a χ^2/dof is given between two sets of data or between data and a simulation. Only those bins for which the data have more than five entries are included as a degree of freedom.

[34] M. Aguilar-Benitez *et al.* (PDG), *Review of Particle Properties* from Phys. Rev., **D45**, (1992); Phys. Rev. **D50**, (1994). The W mass analysis was completed before the 1994 edition of this review, and so used the 1992 numbers; we have updated the numbers in the text to the 1994 values where appropriate. The differences for the numbers used in this paper are completely insignificant.

[35] The momentum scale determination in Section 3 is truly a *transverse* momentum scale determination. The determination of the electron energy scale from E/p in Section 5 is actually a determination of the *transverse* energy scale using E_T/p_T.

[36] The data in Figure 3.4a are fit to a parabola, $y = ax^2 + bx + c$, yielding $a = (2.31 \pm 0.17)$, $b = (0.23 \pm 0.11)$, and $c = (-2.29 \pm 0.08)$. A similar fit to Figure 3.4b yields $a = (0.22 \pm 0.17)$, $b = (0.28 \pm 0.11)$, and $c = (-2.38 \pm 0.08)$.

[37] C. Newman-Holmes, E. E. Schmidt, and R. Yamada, Nucl. Instr. and Meth., **A274**, 443 (1989).

[38] The data in Figure 3.5b are fit to a line, $y = ax + b$, yielding $a = (-2.4 \pm 1.5) \times 10^{-5}$ and $b = (-2.20 \pm 0.09)$.

[39] R. M. Keup, Ph. D. dissertation, University of Illinois, 1995.

[40] F. A. Berends and R. Kleiss, Z. Phys., **C27**, 365 (1985).

[41] R. G. Wagner, Comput. Phys. Commun., **70**, 15 (1992).

[42] U. Baur and E. L. Berger, Phys. Rev., **D41**, 1476 (1990).

[43] F. Abe *et al.* (CDF Collaboration), Phys. Rev. Lett., **73**, 220 (1994).

[44] Electron candidates in the plug and forward regions are not required to have a track, but must have $E_T > 5$ GeV, pass an "isolation requirement" that the energy measured in a cone $\sqrt{(\Delta\phi)^2 + (\Delta\eta)^2} < 0.4$ be less than 10% of the electron energy, and have an electromagnetic fraction greater than 95%. Electrons in the plug calorimeter must also pass a transverse-profile χ^2 test.

[45] The fiducial criteria are 5 cm from the azimuthal (ϕ) edge of the towers, 9 cm away from the central crack at $\theta = 90°$, and that the shower position be no closer than 1.5 towers from the high-η boundary of the CEM.

[46] Note that this method is only used as a check since it is not as robust as the extraction from the $Z \rightarrow ee$ width. The method assumes the same transverse energy for all electrons. Also, systematic effects may cancel in the ratio, E/p, resulting in an extracted constant term which is erroneously low.

[47] Y.-S. Tsai, Rev. Mod. Phys., **45**, 815 (1974).

[48] Uncertainties are extracted from the shifts listed in the tables in this and other sections. Linear fits to the mass shifts relative to the nominal value of the parameter being studied yield a slope as the parameter is increased or decreased. The uncertainty on the parameter being studied is multiplied by the slope to yield an uncertainty on the scale, mass, width or other quantity. If the uncertainty is asymmetric, the uncertainty is symmetrized by taking the larger one.

[49] S. Drell and T. M. Yan, Phys. Rev. Lett., **25**, 316 (1970); erratum, *ibid.*, **25**, 902 (1970).

[50] Note that electron shower leakage, bremsstrahlung landing outside the electron cluster, and overlap with hadronic particles only need to be directly addressed in the recoil reconstruction and not in the electron energy measurement. It is the nature of the electron energy scale determination from E/p to include these effects in the definition of the energy scale for electrons. This is the reason the $W \rightarrow e\nu$ data are used to set the energy scale.

[51] The reader may be concerned that the $< u_{||} >$ and $< M_T^W >$ shifts are not in accord with Equation 2.3. That relation holds only on average for the bulk sample. For smaller subsets chosen with kinematic biases, such as the few rejected W events being considered, it need not hold.

[52] For a description of the MRS D_0', D_-' and H global fits, see A.D. Martin, R.G. Roberts and W.J. Stirling, RAL-92-099 (1993). For a description of the CTEQ global fits, see J. Botts *et al.*, Phys. Lett. **B304**, 159 (1993). For a description of the GRV set, see Z. Phys., **C53**, 127 (1992). For a description of the MT sets, see J. Morfin and W.K. Tung, Z. Phys., **C52**, 13 (1991). The MRS A set uses the CDF charge asymmetry measurement in the fit; all the others are evaluated independently of the CDF measurement.

[53] Only $Z \rightarrow ee$ events, and not $Z \rightarrow \mu\mu$ events, are used for this purpose because the rapidity acceptance for the second electron is much larger than that for the second muon. The larger rapidity acceptance for the electron more closely mimics that for the neutrino.

[54] Polarization effects are included in the decay $W \rightarrow \tau\nu \rightarrow \ell\nu\nu\nu$.

[55] F. Abe *et al.* (CDF Collaboration), Phys. Rev. Lett., **66**, 2951 (1991).

[56] P. B. Arnold and R. P. Kauffman, Nucl. Phys., **B349**, 381 (1991).

[57] G. Altarelli, R. K. Ellis, M. Greco, and G. Martinelli, Nucl. Phys., **B246**, 12 (1984).

[58] F. Abe *et al.* (CDF Collaboration), Phys. Rev. Lett., **67**, 2937 (1991).

[59] M. H. Reno, University of Iowa preprint *UIOWA-94-01 (1994)*.

[60] The factor r cannot be interpreted as a direct comparison of the respective p_T spectra. Combining additional uncertainties arising from differences in the W and Z selection criteria and a statistical uncertainty from the finite number of Z events yields a ratio of 1.11 ± 0.08.

[61] C. Arroyo et al. (CCFR Collaboration), Phys. Rev. Lett., **72**, 3452 (1994).

[62] A. D. Martin and W. J. Stirling, Phys. Lett., **B237**, 551 (1990).

[63] E. L. Berger, F. Halzen, C. S. Kim, and S. Willenbrock, Phys. Rev., **D40**, 83 (1989).

[64] P. Chiappetta and M. Le Bellac, Z. Phys., **C32**, 521 (1986).

[65] F. Paige and S. Protopopescu, **ISAJET** version 6.43, FNAL publication PM0059 (1990).

[66] J. Ohnemus, Phys. Rev., **D44** (1991) 1403.

[67] F. Abe *et al.* (CDF Collaboration), Phys. Rev. Lett., **73**, 225 (1994).

[68] G. Marchesini and B. Webber, Nucl. Phys. **B310**, 461 (1988).

[69] F. Abe *et al.* (CDF Collaboration), submitted to Phys. Rev. Lett. (1994).

[70] J. Rosner, M. Worah, and T. Takeuchi, Phys. Rev., **D45**, 1363 (1994).

[71] D. P. Saltzberg, Ph. D. dissertation, University of Chicago, 1994. It is shown in Appendix A of this dissertation that these fits can be used to reduce the systematic uncertainty on M_W.